

Dynamic Evolution of the Transcrustal Plumbing System in Large Igneous Provinces: Geochemical and Microstructural Insights from Glomerocrysts and Melt Inclusions

MANFREDO CAPRIOLO ^{1,2,*}, SARA CALLEGARO ^{1,3}, FRANCES M. DEEGAN ⁴, RENAUD MERLE⁴, HEEJIN JEON⁵, MARTIN J. WHITEHOUSE⁵, LÁSZLÓ E. ARADI^{6,7}, MALTE STORM^{8,9}, PAUL R. RENNE ^{10,11}, DON R. BAKER¹², JACOPO DAL CORSO¹³, ROBERT J. NEWTON¹⁴, CSABA SZABÓ⁶, BRUNA B. CARVALHO⁷, NASRRDDINE YOUNBI^{15,16,17} and ANDREA MARZOLI ¹⁸

¹Centre for Earth Evolution and Dynamics, University of Oslo, Oslo 0371, Norway

²School of Geography, Earth and Environmental Sciences, University of Birmingham, Birmingham B15 2TT, United Kingdom

³Department of Biological, Geological and Environmental Sciences, University of Bologna, Bologna 40126, Italy

⁴Department of Earth Sciences, Natural Resources and Sustainable Development, Uppsala University, Uppsala SE-752 36, Sweden

⁵Department of Geosciences, Swedish Museum of Natural History, Stockholm SE-104 05, Sweden

⁶Lithosphere Fluid Research Laboratory, Institute of Geography and Earth Sciences, Eötvös Loránd University, Budapest H-1117, Hungary

⁷Department of Geosciences, University of Padova, Padova 35131, Italy

⁸Diamond Light Source, Oxfordshire OX11 0DE, United Kingdom

⁹Helmholtz-Zentrum Hereon, Institute of Materials Physics, Geesthacht 21502, Germany

¹⁰Berkeley Geochronology Center, Berkeley 94709, California, United States

¹¹Department of Earth and Planetary Science, University of California, Berkeley 94720, California, United States

¹²Department of Earth and Planetary Sciences, McGill University, Montreal H3A 0E8, Quebec, Canada

¹³State Key Laboratory of Biogeology and Environmental Geology, China University of Geosciences, Wuhan 430074, China

¹⁴School of Earth and Environment, University of Leeds, Leeds LS2 9JT, United Kingdom

¹⁵Department of Geology, Faculty of Sciences – Semlalia, Cadi Ayyad University, Marrakesh, Morocco

¹⁶Instituto Dom Luiz, University of Lisbon, Lisbon 1749-016, Portugal

¹⁷Faculty of Geology and Geography, Tomsk State University, Tomsk 634050, Russia

¹⁸Department of Land, Environment, Agriculture and Forestry, University of Padova, Legnaro 35020, Italy

*Corresponding author. Email: m.capriolo@bham.ac.uk

The nature of the magma plumbing system of Large Igneous Provinces is still poorly understood. Among these exceptional magmatic events from Earth's past, the end-Triassic Central Atlantic Magmatic Province (CAMP) and the end-Cretaceous Deccan Traps (Deccan) coincided in time with two of the most catastrophic biotic crises during the Phanerozoic. In order to constrain the architecture of their magma plumbing system, glomerocrysts containing abundant bubble-bearing melt inclusions from basaltic lava flows of both CAMP and Deccan were investigated via in situ geochemical and microstructural analyses. The analysed glomerocrysts, dominated by augitic clinopyroxene crystals, represent fragments of a crystal mush entrained by basaltic magmas before eruption. The analysed melt inclusions, consisting of an intermediate to felsic composition glass and CO₂-bearing bubbles, represent relics of interstitial melts and fluids within a porous crystal framework forming the crystal mush. The different volume proportions between bubbles and whole inclusions reveal that melt entrapment occurred after volatile exsolution. The minimum observed bubble/inclusion fraction indicates that the CO₂ concentration in CAMP and Deccan melts was at least 0.3 wt.%, consistent with a maximum entrapment pressure of about 0.5 GPa at CO₂-H₂O fluid-saturated conditions. The MgO-rich composition of host clinopyroxene crystals and whole rocks is in contrast with the SiO₂-rich composition of (trachy-) andesitic to rhyolitic glass of melt inclusions, pointing to disequilibrium conditions. Thermodynamic and geochemical modelling shows that fractional crystallization alone cannot explain the evolved composition of glass in melt inclusions starting from their whole rock composition. On one side, the oxygen isotope composition of clinopyroxene crystals in glomerocrysts ranges from +3.9 (± 0.3) to +5.8 (± 0.3) ‰ and their sample-averaged oxygen isotope composition spans from +4.4 (N = 10) to +5.6 (N = 10) ‰, implying that glomerocrysts crystallized from mafic melts with normal (i.e., mantle-like) to slightly low δ¹⁸O values. On the other side, the oxygen isotope composition of glass in melt inclusions ranges from +5.5 (± 0.4) to +22.1 (± 0.4) ‰, implying that melt inclusions entrapped intermediate to felsic melts with normal (i.e., mantle-like) to extremely high δ¹⁸O values, typical of (meta-) sedimentary rocks. Some melt inclusions are compatible with fractionation from the same mafic melts that crystallized their host mineral phase, but most melt inclusions are compatible with variable degrees of crustal assimilation and partial mixing, potentially followed by minor post-entrapment isotope re-equilibration. In the CAMP, where sedimentary basins are abundant, (meta-) pelites and occasionally granitoids were the most likely assimilants. On the contrary, in the Deccan, where sedimentary basins are rare, granitoids and metapelites were the most likely assimilants. Oxygen isotope compositions of glass in melt inclusions, spanning from mantle-like to crust-dominated signatures, suggest that the CO₂ within their coexisting bubbles likely derived partly from the mantle and partly

RECEIVED AUGUST 8, 2023; REVISED SEPTEMBER 27, 2024; ACCEPTED SEPTEMBER 30, 2024

© The Author(s) 2024. Published by Oxford University Press.

This is an Open Access article distributed under the terms of the Creative Commons Attribution License (<https://creativecommons.org/licenses/by/4.0/>), which permits unrestricted reuse, distribution, and reproduction in any medium, provided the original work is properly cited.

from assimilated crustal materials. The investigated glomerocrysts and their bubble-bearing melt inclusions are relics of a multiphase (i.e., solid + liquid + gas phases) crystal mush revealing a dynamic evolution for the magma plumbing system of both CAMP and Deccan, where crystals, silicate melts and exsolved fluids coexisted and interacted through most of the transcrustal section.

Key words: Central Atlantic Magmatic Province (CAMP); Deccan Traps (Deccan); Confocal Raman microspectroscopy; X-ray microtomography; Oxygen isotopes

INTRODUCTION

The classical model of magma chambers, as uniform and long-lived reservoirs dominated by melt, has been gradually replaced by the recent model of magma plumbing systems comprising multiple, variably interconnected and short-lived reservoirs dominated by crystal mush, extending from crustal roots to Earth's surface (Marsh, 2015; Cashman *et al.*, 2017; Sparks *et al.*, 2019). The term *mush* indicates a multiphase system dominated by a crystalline matrix in which melts coexist with buoyant fluids (Pistone *et al.*, 2013). In transcrustal plumbing systems, crystals, melts and exsolved fluids interact throughout the crustal thickness, amplifying potential element exchanges and mass transfers with the crust, and resulting in typical rock textures and microstructures (Jackson *et al.*, 2018). Compared to a liquid-rich environment (e.g., melt lenses), a more static solid-rich environment (e.g., mush zones) produces characteristic microstructures, such as polycrystalline aggregates indicative of limited crystal mobility, with in situ crystal nucleation and growth (Holness *et al.*, 2019). Glomerocrysts in volcanic rocks are polycrystalline aggregates which may form via several magmatic processes in different magmatic environments, including highly packed crystal frameworks of mush zones, and thus offer unparalleled constraints on the architecture of magma plumbing systems (Holness *et al.*, 2007; Ferguson *et al.*, 2019; McCarthy *et al.*, 2020).

Evidence of a mush-dominated plumbing system was initially provided by active calcalkaline magmatism at convergent margins, but this paradigm was soon thereafter supported by Large Igneous Provinces (LIPs; Grant *et al.*, 2016; Black & Manga, 2017; Bédard *et al.*, 2021; Mittal *et al.*, 2021; Mittal & Richards, 2021; Marzoli *et al.*, 2022). The concept of a mush-dominated plumbing system in the context of LIPs shed light on their pulsed activity, the occurrence of geochemically uniform and distinct magma batches, and the flushing of magma reservoirs via melt-fluid decoupling (Black *et al.*, 2021). In general, LIPs are volumetrically dominated by tholeiitic continental flood basalts, resulting in relatively homogeneous rocks with phenocrysts of augitic clinopyroxene and bytownitic plagioclase, with much higher magma volumes and eruption rates than arc volcanoes, likely implying different mechanisms of magma supply (Ernst, 2014). In contrast with active systems, the study of LIPs may be hindered by plate tectonic fragmentation, by erosion of the original emplaced volume, by alteration of the original magmatic minerals, and cannot be supported by geophysical methods to assess the presence of an active crystal mush. Hence, in situ geochemical and microstructural investigation of rock samples (Ubide *et al.*, 2014, 2019, 2022) is the main viable approach to understand the fossil magma plumbing system of LIPs as well as the evolution of their magmas and volatile budget (Andreasen *et al.*, 2004; Holness *et al.*, 2017; Krans *et al.*, 2018; Marzoli *et al.*, 2022; Carvas *et al.*, 2023).

Magmatic volatiles control magma storage, migration and ascent, and govern eruptive dynamics, ultimately affecting atmosphere, hydrosphere and biosphere with potentially catastrophic consequences, as revealed by the temporal coincidence between LIPs and mass extinction events throughout Earth's history

(Wignall, 2015; Bond & Grasby, 2017; Ernst & Youbi, 2017; Black & Gibson, 2019; Clapham & Renne, 2019; Green *et al.*, 2022). In this study, we focussed on two LIPs (Fig. 1), the Central Atlantic Magmatic Province (CAMP) at about 201 Ma (Marzoli *et al.*, 1999, 2018) and the Deccan Traps (Deccan) at about 66 Ma (Schoene *et al.*, 2019; Sprain *et al.*, 2019), respectively synchronous with end-Triassic and Cretaceous–Palaeogene boundary mass extinctions (Raup & Sepkoski, 1982; Marzoli *et al.*, 2004; Hull *et al.*, 2020). The emplacement of the CAMP induced volcanic and thermogenic emissions of greenhouse gases, such as CO₂ and CH₄ (Capriolo *et al.*, 2020, 2021), which seriously affected the end-Triassic global climate and environment (Marzoli *et al.*, 2004; Heimdal *et al.*, 2018, 2020; Capriolo *et al.*, 2022). Similarly, the emplacement of the Deccan degassed mainly CO₂ and SO₂ (Self *et al.*, 2008; Callegaro *et al.*, 2014a, 2023; Choudhary *et al.*, 2019; Hernandez Nava *et al.*, 2021), which deteriorated the end-Cretaceous surface system (Hull *et al.*, 2020; Gilibert *et al.*, 2021). Among magmatic volatiles, CO₂ is one of the most impactful greenhouse gases, and is a propellant of volcanic eruptions in basaltic systems (Black & Manga, 2017; Caricchi *et al.*, 2018). Quantifying magmatic CO₂ is thus crucial to reconstruct its role in the eruptive mechanism of LIPs and their implication in mass extinction events. However, the CO₂ preserved in whole rock samples is a minimal part of the original magmatic CO₂ as it tends to exsolve and escape from deep levels in Earth's crust (Pichavant *et al.*, 2013). Melt inclusions (MIs) are microscopic imperfections in minerals which may entrap melts and coexisting fluids during the crystal growth, and their study is thus fundamental to quantify magmatic CO₂ throughout the magma plumbing system (Roedder, 1979; Self *et al.*, 2005; Baker, 2008).

Here, we analysed glomerocrysts containing bubble-bearing MIs sampled from basaltic lava flows of both CAMP and Deccan, using a multi-technique approach from micro- to macro-scale, in order to assess the occurrence of a crystal mush in their magma plumbing system, and to investigate how crystals, melts and exsolved fluids interact throughout the transcrustal section. Confocal Raman microspectroscopy allowed the quantification of CO₂ density within bubbles of MIs. Synchrotron radiation X-ray microtomography provided precise volume proportions of bubbles within MIs (i.e., bubble/inclusion fractions), which are essential for estimating the original CO₂ concentration in the melts and were previously determined by optical microscopy observations in 2D only. Electron microprobe (EMP) and secondary ion mass spectrometry (SIMS) analyses of MIs glass and their host clinopyroxene revealed the origin of the melts via major element and oxygen isotope compositions. Furthermore, thermodynamic and geochemical modelling was employed to test the potential occurrence of differentiation by fractional crystallization and crustal assimilation, as well as the possible implications for diffusional exchange of oxygen isotopes. By combining in situ geochemical and microstructural methods, we reconstructed complex magmatic differentiation processes occurring in mush zones within the transcrustal plumbing system of the two investigated LIPs. Hence, we obtained new constraints on the origin and transfer

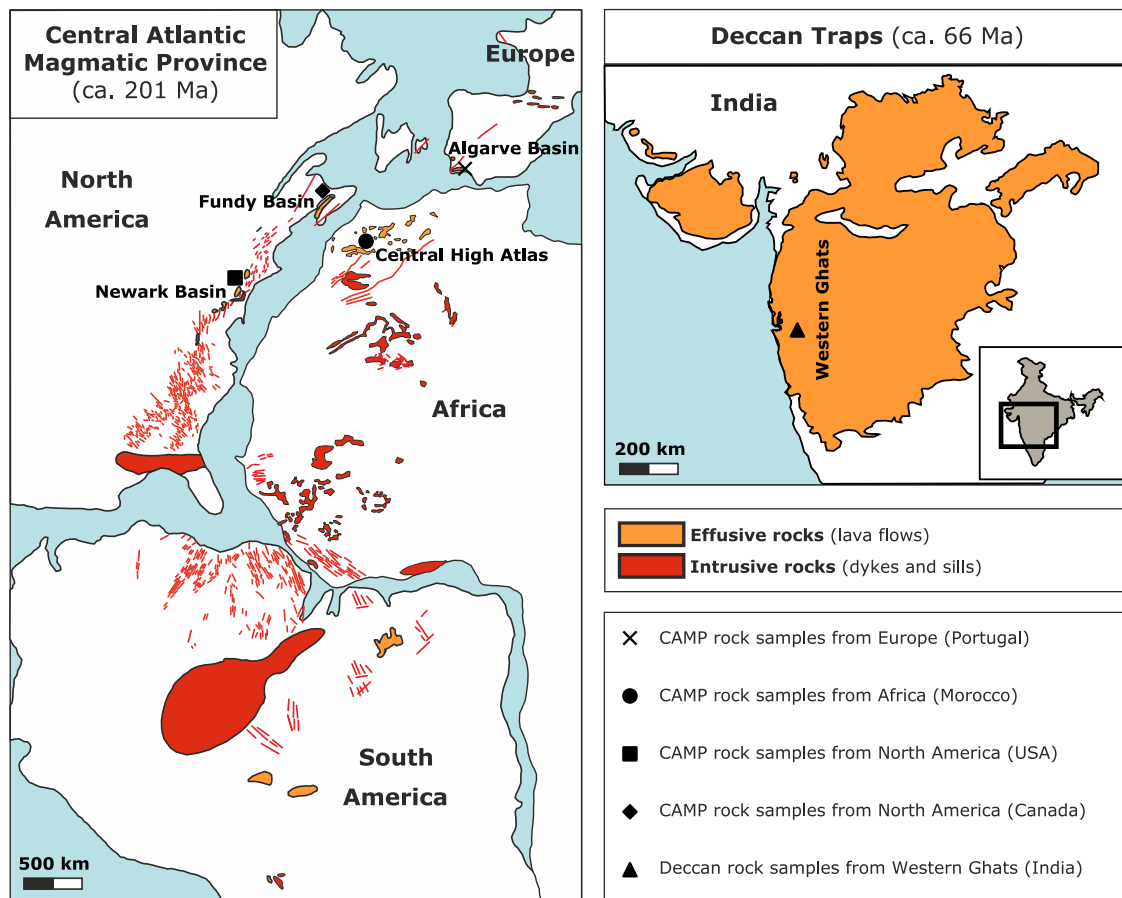


Fig. 1. Overview of the Central Atlantic Magmatic Province and the Deccan Traps with rock samples location. The preserved volume of the CAMP (map adapted from Marzoli *et al.*, 2018) is volumetrically dominated by intrusive rocks, whereas the preserved volume of the Deccan (map adapted from Marzoli *et al.*, 2022) is volumetrically dominated by effusive rocks. The investigated CAMP rock samples are lava flows from Algarve Basin, Fundy Basin, Newark Basin and Central High Atlas, and the investigated Deccan rock samples are lava flows from Western Ghats (Supplementary Fig. 1 and Supplementary Tab. 1).

of carbon from the mantle to Earth's surface, with crucial implications for LIPs emplacement and for their environmental and climatic impact.

GEOLOGICAL SETTING AND SAMPLING

The CAMP is one of the most voluminous Phanerozoic LIPs and was synchronous with the end-Triassic mass extinction (Marzoli *et al.*, 2004). This LIP was emplaced over an area of about 1.0×10^7 km² throughout the circum-Atlantic continents (Fig. 1), involving an original volume of $>3.0 \times 10^6$ km³ magmas (Marzoli *et al.*, 1999, 2018; Davies *et al.*, 2017). The analysed CAMP rock samples are from several lava flows outcropping in North America (Merle *et al.*, 2014), Africa (Marzoli *et al.*, 2019) and Europe (Callegaro *et al.*, 2014b). All rock samples belong to the early phase of CAMP activity (latest Triassic), at ca. 201.6–201.5 Ma, except for two rock samples (NEW73 from USA and AN156A from Morocco) belonging to the late phase of CAMP activity (earliest Jurassic), at ca. 201.2–200.9 Ma (Blackburn *et al.*, 2013; Davies *et al.*, 2017; Marzoli *et al.*, 2019).

The Deccan was active across the Cretaceous–Palaeogene boundary, which was marked by the Chicxulub bolide impact and the disappearance of non-avian dinosaurs among multiple other marine and terrestrial species (Alvarez *et al.*, 1980; Courtillot *et al.*, 1986; Renne *et al.*, 2015). This LIP was emplaced over an area of about 1.5×10^6 km² on the Indian subcontinent (Fig. 1), involving

an original volume of $>1.5 \times 10^6$ km³ magmas (Beane *et al.*, 1986; Krishnamurthy, 2020a, 2020b; Mittal *et al.*, 2022; Self *et al.*, 2022). The analysed Deccan rock samples are from different lava flows outcropping in the Western Ghats, India (Sprain *et al.*, 2019). Two rock samples (BOR14-2 and MAT14-3 from the Thakurvadi Formation) belong to the Kalsubai Subgroup, corresponding to the early phase of Deccan activity (latest Cretaceous), at ca. 66.3–66.1 Ma, whereas the other two rock samples (KJA14-2 and PAS14-1 from the Poladpur and Mahabaleshwar Formations, respectively) belong to the Wai Subgroup, corresponding to the late phase of Deccan activity (earliest Palaeocene), at ca. 66.0–65.5 Ma (Sprain *et al.*, 2019).

Magma generation in both CAMP and Deccan continued over about 1 Ma, but magma discharge occurred in short-lived (few hundred years) pulses with high eruption rate, according to geochemical, geochronological and magnetostratigraphic constraints (Knight *et al.*, 2004; Chenet *et al.*, 2008; Davies *et al.*, 2017, 2021; Fendley *et al.*, 2019; Schoene *et al.*, 2019; Sprain *et al.*, 2019). Apart from this similarity, these two LIPs differ in many ways. The preserved volume of the CAMP mainly consists of shallow magmatic intrusions (e.g., sills, dykes and layered intrusions), with a total volume of about 2×10^6 km³, and minor lava flows in sedimentary basins, forming lava piles up to 400 m thick (Philpotts *et al.*, 1996; Kontak, 2008; Marzoli *et al.*, 2019). Most CAMP basaltic lava flows have low TiO₂ (<2.0 wt.%) content, and a large portion of the CAMP intruded rift basins dominated

by volatile-rich sedimentary rocks, thus having a high potential for thermogenic gas production by magma–sediment interaction (Heimdal *et al.*, 2019; Capriolo *et al.*, 2021; Davies *et al.*, 2021). Conversely, the preserved volume of the Deccan mostly consists of lava flows on a crystalline basement, forming lava piles up to 1650 m thick in the Western Ghats, with a cumulative volcanostratigraphic thickness up to 3 km (Krishnamurthy, 2020a, 2020b). These lava flows were emplaced on a gneissic basement, which was intruded by Archean and Palaeoproterozoic granitic plutons and rarely overlain by sedimentary sequences, thus having a relatively low potential for thermogenic gas production by magma–sediment interaction. Sedimentary basins of Proterozoic and seldom Phanerozoic (mostly Palaeozoic) age occur in grabens mainly to the North of the Western Ghats (Krishnamurthy, 2020a, 2020b). Unlike the CAMP, the Deccan also recorded felsic and alkaline magmatic activity (Cucciniello *et al.*, 2019, 2020; Basu *et al.*, 2020; Halder *et al.*, 2023). Additionally, in the Western Ghats, Deccan basaltic lava flows have dominantly high TiO₂ (>2.0 wt.%) content and are occasionally interlayered with m-thick palaeosol horizons, called *red boles*, which often include reworked silicic tephra in terrigenous sediments (Ghosh *et al.*, 2006; Krishnamurthy, 2020a, 2020b; O'Connor *et al.*, 2022).

ANALYTICAL METHODS

Based on the presence of glomerocrysts containing bubble-bearing MIs, the most representative 15 basaltic rock samples were selected for this study (Supplementary Fig. 1 and Supplementary Tab. 1). The 11 selected rock samples for the CAMP are from North America (samples NEW31 and NEW73 from USA, and samples NS9, NS12, NS13 and NS21 from Canada), Africa (samples AN18, AN39, AN137A and AN156A from Morocco) and Europe (sample AL14 from Portugal). The 4 selected rock samples for the Deccan are from the Western Ghats (samples BOR14-2, KJA14-2, MAT14-3 and PAS14-1 from India). All rock samples were prepared as thin and thick sections, rock chips and epoxy mounts (see Supplementary Materials for sample preparation). The same glomerocrysts and different bubble-bearing MIs from the same primary assemblages within the same glomerocrysts were analysed by confocal Raman microspectroscopy, Synchrotron radiation X-ray microtomography, EMP and SIMS in all rock samples (Fig. 2).

Confocal Raman microspectroscopy

Volatile species within bubbles of unexposed MIs were characterized by confocal Raman microspectroscopy in all rock samples from the Deccan only, using thick sections and rock chips cast in epoxy mounts. All CAMP rock samples were previously analysed by confocal Raman microspectroscopy (Capriolo *et al.*, 2020). Confocal Raman microspectroscopy was carried out at the Research and Industrial Relations Center of the Faculty of Science, Eötvös Loránd University of Budapest (Hungary), using a HORIBA Jobin Yvon LabRAM HR800 Raman microspectrometer. Spot analyses in both single- and multi-window settings were carried out at ambient temperature, below the sample surface for all the investigated MIs, allowing to characterize the volatile content of bubbles within MIs, and to determine its density. A frequency doubled Nd–YAG green laser with a 532 nm excitation wavelength was employed, displaying 120 mW at the source and 23 mW on the sample surface. An OLYMPUS objective with 100× magnification (N.A.=0.9) was used to focus the laser on the analysis sites. A 50 μm (for sample BOR14-2) and 100 μm (for samples KJA14-2, MAT14-3 and PAS14-1) confocal hole, a 1800

grooves/mm optical grating, 2–10 accumulations and a 20–60 s exposure time were employed. The investigated spectral region of interest ranged from 100 to 4000 cm⁻¹, and the spectral resolution of measurements varied from 0.8 to 3.0 cm⁻¹. All Raman data were processed via LabSpec 5 software by HORIBA Jobin Yvon.

Synchrotron radiation X-ray microtomography

Selected glomerocrysts and bubble-bearing MIs were analysed by Synchrotron radiation X-ray microtomography in all rock samples from both CAMP and Deccan, using rock chips from the same thick sections previously analysed by confocal Raman microspectroscopy. X-ray microtomography was carried out at the beamline I13-2 of Diamond Light Source (UK), using a pink beam with 20.5 keV mean energy. A pco.edge sCMOS detector with a total 20× magnification, a 2560 × 2160 pixel field of view and an effective 325 nm-side pixel were employed for image acquisition, resulting in <1 μm overall full resolution of the system. Each rock chip was mounted on a pin for X-ray microtomography acquisition, and a sample volume of ca. 800 × 700 × 100–150 μm³ was analysed in each rock chip. Raw image data were reconstructed in the open-source Savu framework (Wadeson & Basham, 2016), using the TomoPy reconstruction package (Gürsoy *et al.*, 2014). After identifying the centre of rotation, the processing of X-ray microtomography data involved pre-processing and denoising, using a non-local means filter, then segmentation, volume measurement and volume rendering. Imaging of these data hinges on the different density of the analysed materials (mineral phases, glass and bubbles, which may be empty or occupied by fluid phases). Reconstructed data were processed at workstation I13-Data of Diamond Light Source (UK), using Avizo software by Thermo Fisher Scientific, in order to model the most representative glomerocrysts and MIs in 3D, and to calculate volume proportions of the different phases. The reconstructed glomerocrysts were selected according to their variability in terms of volume proportions between constituting mineral phases, whereas the reconstructed MIs were selected according to their variability in terms of size, shape, number of bubbles and volume proportions between bubbles, glass and daughter mineral phases, across all the investigated rock samples.

Electron microprobe (EMP) analysis

Major element compositions of the host clinopyroxene (Cpx) crystals from glomerocrysts and of the glass of exposed MIs were determined by EMP in all rock samples from both CAMP and Deccan, using thin sections and rock chips cast in epoxy mounts from the same rock chips previously analysed by Synchrotron radiation X-ray microtomography. Since some CAMP rock samples were previously analysed by EMP (Capriolo *et al.*, 2020), Deccan rock samples were more extensively investigated via additional analytical sessions for the host Cpx crystals, the glass of exposed MIs and the daughter mineral phases within them. In addition, S (and Cl for further EMP analysis on Deccan rock samples) was measured in the glass of exposed MIs. EMP analysis was carried out at the Department of Geosciences, University of Oslo (Norway), using a Cameca SX100 electron microprobe for all rock samples, and at the Department of Earth Sciences, University of Milano (Italy), using a JEOL JXA 8200 Superprobe for 3 rock samples from the Deccan (samples BOR14-2, KJA14-2 and PAS14-1). The analyses acquired at these two facilities are equivalent and comparable for the level of accuracy required in the present study. For the measurement of host Cpx and daughter mineral phases within MIs at the facility in Oslo, a ≤1 μm (i.e., focussed) beam diameter was adopted. Beam current was 15 nA, accelerating

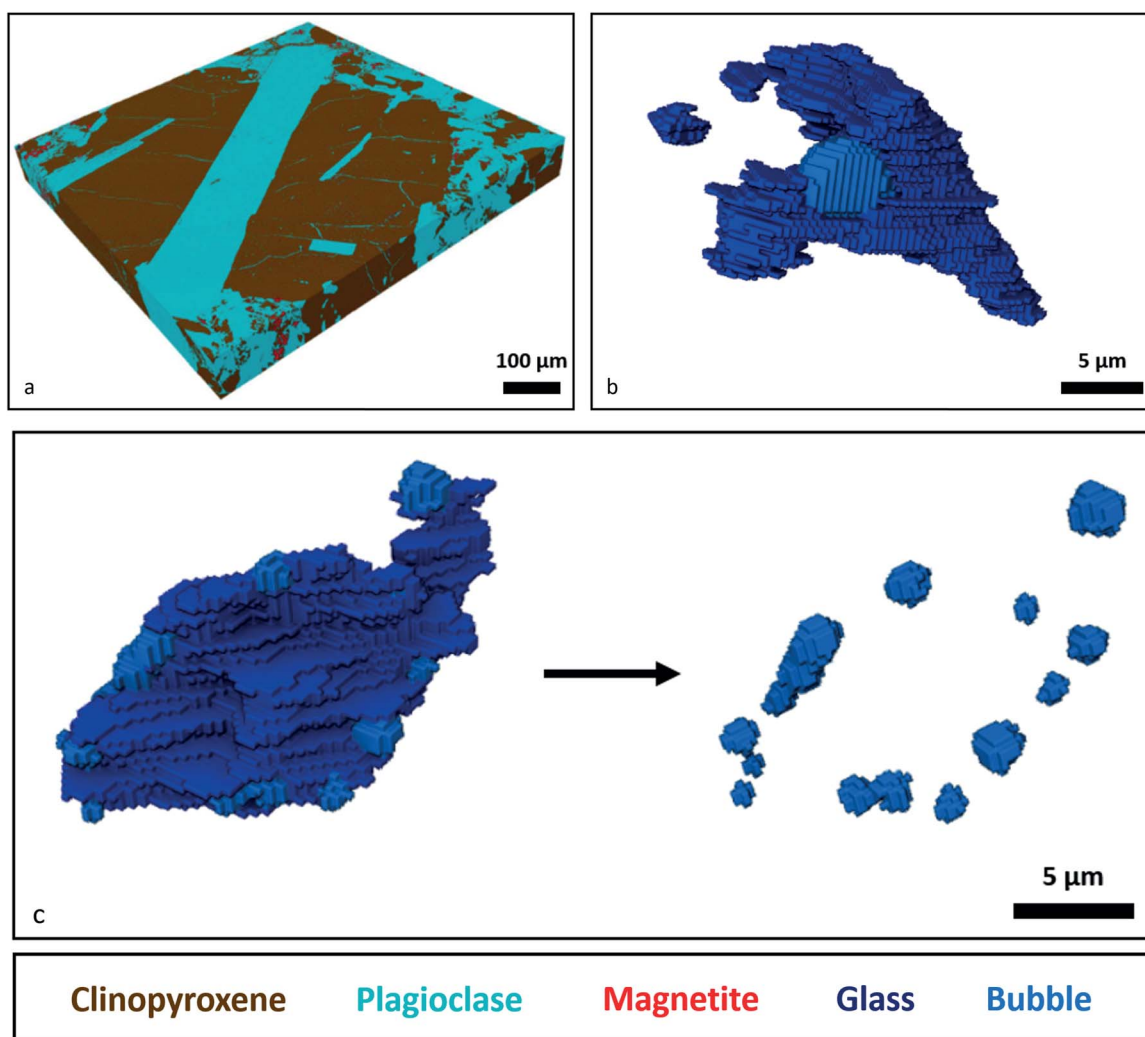


Fig. 2. 3D reconstructions of a glomerocryst and bubble-bearing MIs. Representative 3D reconstructions of a glomerocryst and bubble-bearing MIs by Synchrotron radiation X-ray microtomography. a) 3D reconstruction of a glomerocryst consisting of clinopyroxene (brown phase) and plagioclase (teal phase), in a microcrystalline groundmass consisting of the same mineral phases and magnetite (red phase; sample AN156A, CAMP, Morocco). b) 3D reconstruction of a single-bubble MI, consisting of glass (dark blue phase) and a single bubble (light blue phase; sample NEW31, CAMP, USA). c) 3D reconstruction of a multi-bubble MI, consisting of glass (dark blue phase) and multiple bubbles (light blue phase; sample NEW31, CAMP, USA). See [Supplementary Data 1](#) for all the glomerocrysts and bubble-bearing MIs reconstructed by Synchrotron radiation X-ray microtomography.

voltage was 15 kV, and counting times were 10 s on the peak and 5 s on the background for all analysed elements. The spatial step of transects in host Cpx was about 5 µm for all analysed samples, except for sample NS21, where the spatial step of the transect in host orthopyroxene (Opx) was about 10 µm. For the measurement of host Cpx at the facility in Milano, a 1 µm beam diameter was adopted. Beam current was 5 nA, accelerating voltage was 15 kV, and counting times were 10 s on the peak and 5 s on the background for all analysed elements. The spatial step of transects in host Cpx was 4 µm for all analysed samples. For the measurement of glass in exposed MIs at the facility in Oslo, a 3 µm beam diameter was adopted in most cases, but during the further investigation on Deccan rock samples a 5 µm beam diameter was preferentially adopted when possible. Beam current was 10 nA, accelerating voltage was 15 kV, and counting times were 10 s on the peak and 5 s on the background for all analysed elements. For the measurement of glass in exposed MIs at the facility in Milano, a 1 µm beam diameter was adopted to avoid contamination from the surrounding host mineral phase. Beam current was 5 nA, accelerating voltage was 15 kV, and counting

times were 10 s on the peak and 5 s on the background for all analysed elements. Natural and synthetic standards were used for instrumental calibration. For the analysis of glass and mineral phases at the facility in Oslo, the employed standards were wolastonite for Si and Ca, albite for Na, orthoclase for K, pyrophanite for Ti and Mn, barium sulphite for S, synthetic alforosite for Cl, metal iron for Fe, and the corresponding oxides for Al, Mg and Cr. Similarly, for the analysis of glass and mineral phases at the facility in Milano, the employed standards were grossular for Si, Al and Ca, omphacite for Na, orthoclase for K, fayalitic olivine for Fe, forsteritic olivine for Mg, rhodonite for Mn, ilmenite for Ti, galena for S, scapolite for Cl, and metal chromium for Cr. The analytical uncertainty on major elements is typically <1 wt.% at the 2σ level for both glass and mineral phases.

Secondary ion mass spectrometry (SIMS) analysis

Oxygen isotope ratios of the host Cpx crystals from glomerocrysts and of the glass from exposed MIs were analysed by SIMS in all rock samples from both CAMP and Deccan, using rock chips cast

in epoxy mounts from the same rock chips previously analysed by Synchrotron radiation X-ray microtomography. The selected rock chips were washed in acetone, cleaned in ethanol, dried in oven, cast in epoxy resin, gently polished, and then coated with a gold layer in preparation for SIMS analysis. SIMS analysis was carried out at the NordSIMS ion microprobe facility, Swedish Museum of Natural History, Stockholm (Sweden), using a CAMECA IMS 1280 multi-collector instrument. Prior to SIMS analysis, the epoxy mounts were imaged using a Hitachi TM4000Plus desktop scanning electron microscope (SEM) located at the same facility. Analysis sites potentially affected by the presence of (micro-) fractures or, in the case of MIs, by the occurrence of evident post-entrapment crystallization were carefully avoided. Only exposed MIs with a $\geq 10 \times 10 \mu\text{m}^2$ bubble-free area were selected for SIMS analysis. Each analysis was preceded by an initial 80 s pre-sputter phase with a $15 \mu\text{m}$ -side square raster. A Cs^+ primary beam of ca. 1.5 nA was used in critically-focussed mode together with a $5 \mu\text{m}$ -side square raster to sputter a $< 10 \times 10 \mu\text{m}^2$ sample area with an impact energy of 20 keV. A normal incidence low energy electron gun provided charge compensation, and a secondary ion beam was centred in the field aperture with the ^{16}O signal, followed by a 64 s (16 cycles of 4 s integrations) data acquisition. Data were acquired using two Faraday cup detectors (amplifiers equipped with 10^{10} and $10^{12} \Omega$ resistors for ^{16}O and ^{18}O , respectively) in the multi-collector system operating at a mass resolution of ca. 2500. The secondary magnetic field was regulated at high precision, using a Metrolab NMR teslameter.

Appropriate reference materials were analysed in a sample-bracketing procedure every 4 to 6 analyses of the unknown samples, in order to measure the external precision (i.e., reproducibility) as well as to correct for within-session drift of oxygen isotope ratios and for instrumental mass fractionation (IMF). Oxygen isotope ratios are reported in standard δ -notation, as $\delta^{18}\text{O}_{\text{VSMOW}}$ (i.e., Vienna Standard Mean Ocean Water; Gonfiantini, 1978; Coplen, 1988), and expressed as $\delta^{18}\text{O}_{\text{Cpx}}$ and $\delta^{18}\text{O}_{\text{glass}}$ for host Cpx and MIs glass, respectively. Unless otherwise stated, the analytical uncertainty is reported at the 2σ level.

The (unoriented) augitic Cpx crystal NRM-AG-1 ($\delta^{18}\text{O}$ value of +5.45 ‰; Deegan et al., 2016) was employed as the reference material for host Cpx, and was embedded in all the analysed epoxy mounts. Since this reference material has an augitic composition with Fs (ferrosilite) content $\sim 15\%$ and Wo (wollastonite) content $\sim 45\%$, all the analysed spots on Cpx crystals with Fs content $> 30\%$ and Wo content $< 30\%$ were discarded as not matching the reference material, including those on Opx and pigeonitic Cpx crystals. Throughout the analytical session of Cpx crystals, external precision was 0.13 ‰ (1 σ standard deviation, SD) on NRM-AG-1 and internal precision was on average 0.11 ‰ (1 σ standard error, SE; overall range of 0.09 to 0.18 ‰). The average ^{16}O intensity of Cpx crystals was 0.9×10^9 cps.

The silicate glass BCR-2G (SiO_2 content of 54.4 wt.% and $\delta^{18}\text{O}$ value of +7.01 ‰; Hartley et al., 2012) was employed as the reference material for MIs glass, and was embedded in all the analysed epoxy mounts. Because of their different composition (mainly in terms of SiO_2), silicate glasses show a significant IMF bias (ΔIMF), that is the difference between accepted and measured oxygen isotope ratios. In order to overcome the ΔIMF issue, a suite of 9 glass reference materials (7 MPI-DING glasses, 1 USGS glass and 1 obsidian, with SiO_2 contents from 45.5 to 75.6 wt.% and $\delta^{18}\text{O}$ values from +3.20 to +9.43 ‰; Jochum et al., 2006; Hartley et al., 2012) was measured before and after each analytical session of MIs glass. The silicate glass BCR-2G, embedded as an internal reference material in each epoxy mount, was also

included in the suite of external reference materials. Repeated analyses of external reference materials provided a correction scheme based on their SiO_2 content, which was applied to all unknown samples of MIs glass, using EMP data acquired after SIMS analysis. Throughout the analytical sessions of MIs glass, external precision ranged from 0.13 to 0.14 ‰ (1 σ SD) on BCR-2G and internal precision was on average 0.12 ‰ (1 σ SE; overall range of 0.08 to 0.25 ‰). The average ^{16}O intensity of MIs glass was 1.0×10^9 cps.

RESULTS

Petrography of glomerocrysts

All rock samples from both CAMP and Deccan are basaltic lava flows, consisting of holocrystalline, isotropic and porphyritic rocks, characterized by the presence of phenocrysts and glomerocrysts in a microcrystalline groundmass (Supplementary Fig. 2). In this study, the term *phenocryst* refers to any single crystal larger than 500 μm , without any implications for its equilibrium with the surrounding groundmass. Similarly, the term *glomerocryst* refers to any (glomerocrystic or glomerophytic) aggregate of crystals larger than 500 μm . In the investigated rock samples, the phenocrysts consist of mainly augitic clinopyroxene (Cpx), plagioclase (Pl), rare orthopyroxene (Opx) and altered olivine (Ol), and the microcrystalline groundmass consists of the same mineral phases plus oxides (Figs. 3 and 4). Except for sample AL14, where ilmenite (Ilm) is more abundant, magnetite (Mag) is the most common oxide in CAMP rock samples, whereas Ilm and Mag are equally abundant in Deccan rock samples. Glomerocrysts are usually dominated by Cpx, with a mainly augitic and subordinately pigeonitic composition, and often contain Pl and rarely Opx (Fig. 3). As polycrystalline domains, glomerocryst-forming crystals display different optical orientations, and their Cpx crystals are intergrown and sintered together along with Pl and Opx crystals, without any interstitial (microcrystalline or glassy) groundmass, but often entrapping bubble-bearing MIs (Supplementary Fig. 3). The analysed glomerocrysts generally range from about 500 μm to 5 mm, whereas their individual crystals mostly vary from about 100 μm to 1 mm in size (Fig. 4). Phenocrysts and glomerocryst-forming crystals sometimes display irregular (wavy to subgranular) extinction, kink bands and deformed twinning planes, such as tapered twins (Supplementary Fig. 4). The crystallization sequence, based on spatial relationships between the different mineral phases within and around glomerocrysts, indicates the coprecipitation of pyroxene and plagioclase from the melt, followed by Fe-Ti oxides (see Supplementary Data 1 for all the glomerocrysts reconstructed by Synchrotron radiation X-ray microtomography; 16 reconstructed glomerocrysts, 13 for the CAMP (plus 1 single crystal) and 3 for the Deccan).

Petrography of melt inclusions

All Cpx-dominated glomerocrysts host abundant bubble-bearing MIs, up to several hundred per glomerocryst (Supplementary Fig. 5). The main host mineral phase is augitic Cpx, and the MIs are in growth shells of single crystals or between individual crystals within the glomerocrysts, displaying a variable number of bubbles, usually from 1 to 15 per inclusion, but exceptionally even more. Multi-bubble MIs are common in CAMP rock samples, whereas single-bubble MIs are dominant in Deccan rock samples (Figs. 5 and 6).

In general, MIs may have a primary, pseudosecondary or secondary origin (Roedder, 1984). Primary MIs are entrapped during

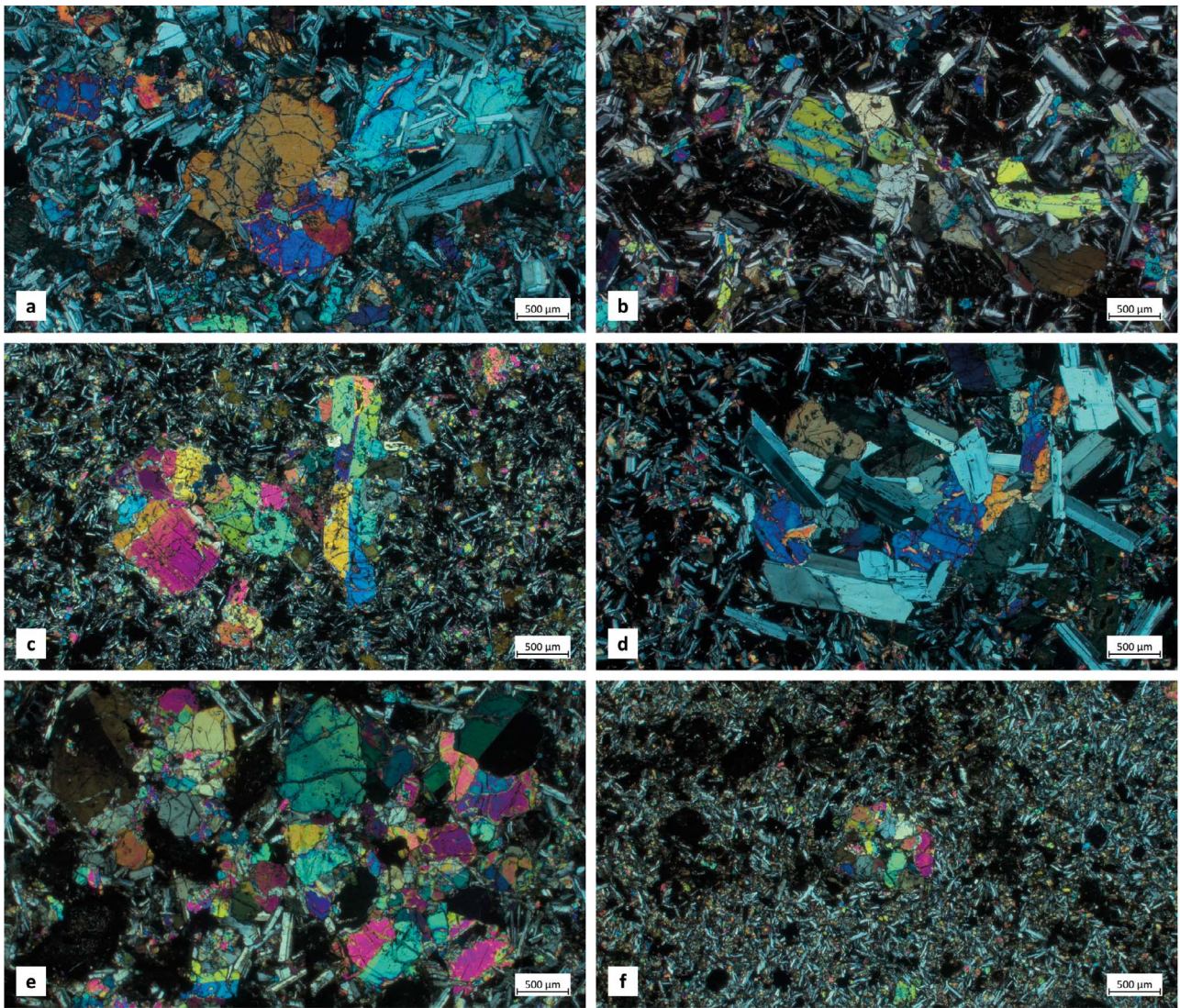


Fig. 3. Photomicrographs of glomerocrysts containing bubble-bearing MIs, from both CAMP and Deccan. Representative photomicrographs of glomerocrysts containing bubble-bearing MIs from CAMP and Deccan lava flows in transmitted, crossed polarized light. a) Cpx-dominated glomerocryst (sample AL14, CAMP, Portugal). b) Cpx-dominated glomerocryst (sample AN137A, CAMP, Morocco). c) Cpx-dominated glomerocryst (sample NEW31, CAMP, USA). d) Pl-dominated glomerocryst (sample NS12, CAMP, Canada). e) Cpx-dominated glomerocrysts (sample BOR14-2, Deccan, India). This cumultic rock sample displays coarser grain, higher porphyricity and slightly different mineralogical composition compared to the other rock samples; although completely altered, Ol was present in interstitial position and along the rims of Cpx-dominated glomerocrysts. f) Tiny (mm-sized), Cpx-dominated glomerocryst (sample PAS14-1, Deccan, India).

growth of the host mineral phase, whereas secondary MIs are entrapped after growth of the host mineral phase because of its fracturing and subsequent healing. Similarly, pseudosecondary MIs are entrapped because of the brittle deformation of the host mineral phase prior to its final growth. In the investigated rock samples, bubble-bearing MIs are randomly distributed in clusters corresponding to specific portions of the Cpx crystal domains within the glomerocrysts (Fig. 5). These common clusters of MIs within the Cpx-dominated glomerocrysts likely formed during a specific phase of crystal growth, indicating a primary origin. In few cases, bubble-bearing MIs are aligned along planes cutting limited sectors of the Cpx crystal domains within the glomerocrysts. These rare alignments of MIs within the Cpx-dominated glomerocrysts likely formed from sealing fractures when crystal growth was still ongoing, indicating a pseudosecondary origin.

The analysed MIs are mostly composed of glass, which is optically transparent or sometimes brownish in larger MIs, likely due to devitrification and alteration (Fig. 5). The analysed MIs

also often contain tiny (μm -sized) crystals, which are optically opaque (mostly Mag) or transparent and similar to the host mineral phase (likely Cpx). Rather than incidentally being entrapped along with the melt, these crystals likely crystallized from the entrapped melt within MIs (i.e., daughter mineral phases). Bubbles are usually distributed along MIs boundary, especially within multi-bubble MIs.

The size of the analysed MIs ranges from 10 to 80 μm , and exceptionally up to 100 μm , on the principal axis, whereas the size of their bubbles ranges from <1 to 30 μm in diameter (Fig. 6). The shape of the analysed MIs is variable, but generally highly irregular. They are often elongated or flattened, frequently hooked, and sometimes display peculiar shapes, such as a hemisphere or a torus. In some cases, the analysed MIs consist of disconnected and spatially separated portions of glass and bubbles. The shape of bubbles within MIs is variable as well, from perfectly spherical to irregular. They are often oblate or prolate spheroids, but sometimes simply occupy the interstices between growing

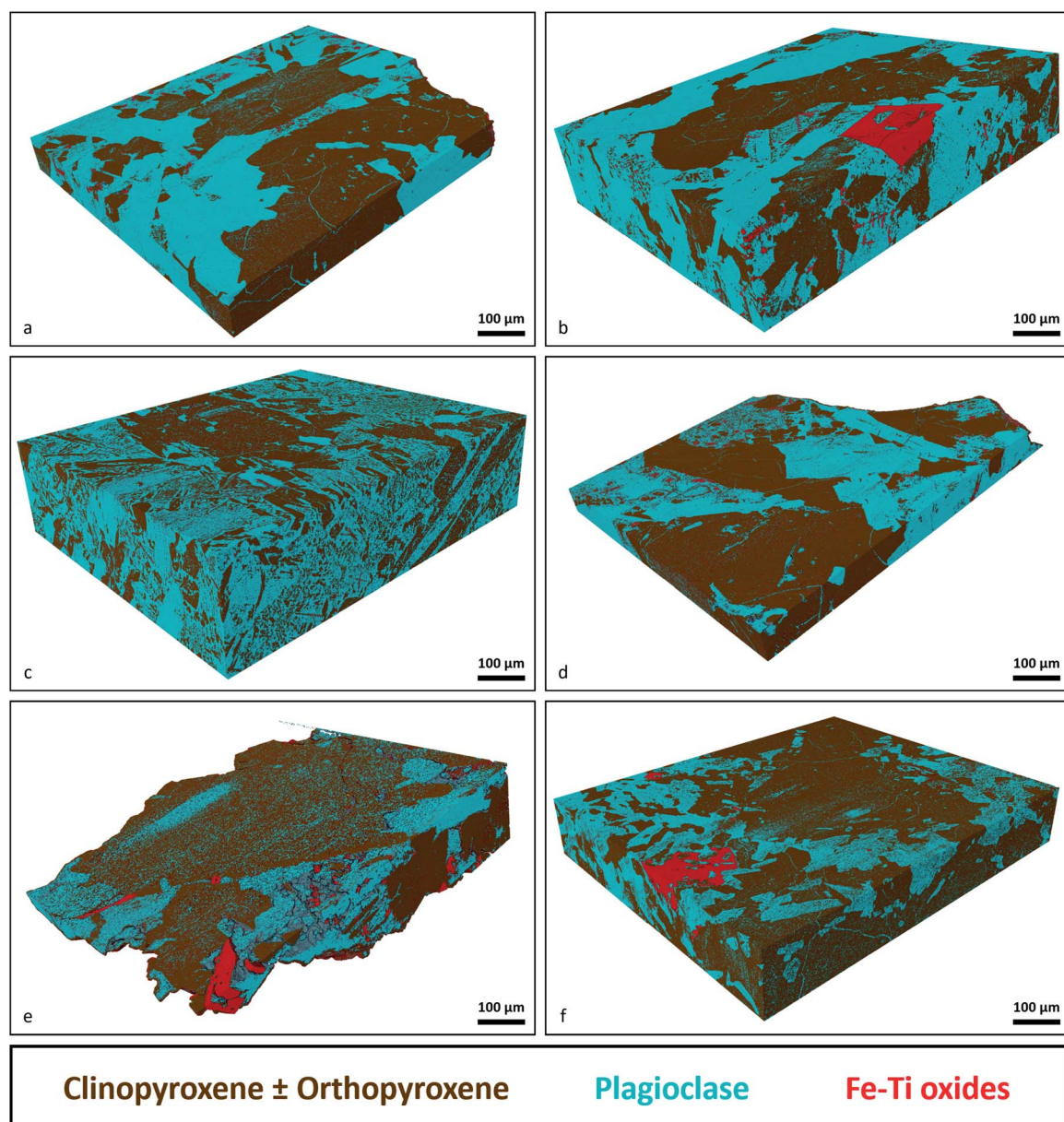


Fig. 4. 3D reconstructions of glomerocrysts, from both CAMP and Deccan. Representative 3D reconstructions of glomerocrysts by Synchrotron radiation X-ray microtomography. Glomerocrystic aggregates consist of Cpx ± Opx (brown phase) and Pl (teal phase) in a microcrystalline groundmass consisting of the same mineral phases and Fe-Ti oxides, mostly Mag ± Ilm (red phase). Empty interstices such as fractures and (gas-bearing) bubbles of MIs (not visible at this scale) were also reconstructed. a) Sample AN39, CAMP, Morocco. b) Sample NEW73, CAMP, USA. c) Sample NS9, CAMP, Canada. d) Sample NS21, CAMP, Canada. e) Sample MAT14-3, Deccan, India. f) Sample PAS14-1, Deccan, India. See [Supplementary Data 1](#) for all the glomerocrysts reconstructed by Synchrotron radiation X-ray microtomography.

crystals (see [Supplementary Data 1](#) for all the bubble-bearing MIs reconstructed by Synchrotron radiation X-ray microtomography; 12 reconstructed MIs, 9 for the CAMP and 3 for the Deccan).

Major element composition of host Cpx, MIs glass and daughter mineral phases

The host Cpx, the glass and the daughter mineral phases of exposed MIs in glomerocrysts were analysed by EMP for major element composition (see [Supplementary Data 2](#) for all the analytical data; 517 EMP spots on host Cpx and Opx crystals, 359 for the CAMP and 158 for the Deccan; 99 EMP spots on MIs glass, 44 for the CAMP and 55 for the Deccan; 5 EMP spots on daughter mineral phases from 3 MIs for the Deccan). Apart from rare host Opx crystals with an enstatitic composition (e.g., sample NS21), the

analysed host Cpx crystals have a mainly augitic and subordinately pigeonitic composition (Fig. 7). All the analysed host Cpx and Opx crystals are MgO-rich, from 34 to 85 Mg# and on average 76 Mg# (defined as $\text{Mg}/(\text{Mg} + \text{Fe}) \times 100$, where Mg and Fe are expressed in mol.%, and Fe is total Fe), and major element composition varies from cores to rims in MI-rich polycrystalline aggregates of Cpx (see [Supplementary Data 3](#) for the photomicrographs of all the sites analysed by EMP on host Cpx crystals). In the investigated rock samples from both CAMP and Deccan, MgO and CaO decrease from cores to rims of Cpx crystals, whereas FeO and TiO₂ increase (Fig. 8). In general, the analysed host Cpx crystals do not show any evident major element variation close to MIs.

The glass was analysed in exposed MIs (see [Supplementary Data 3](#) for the photomicrographs of all the sites analysed by

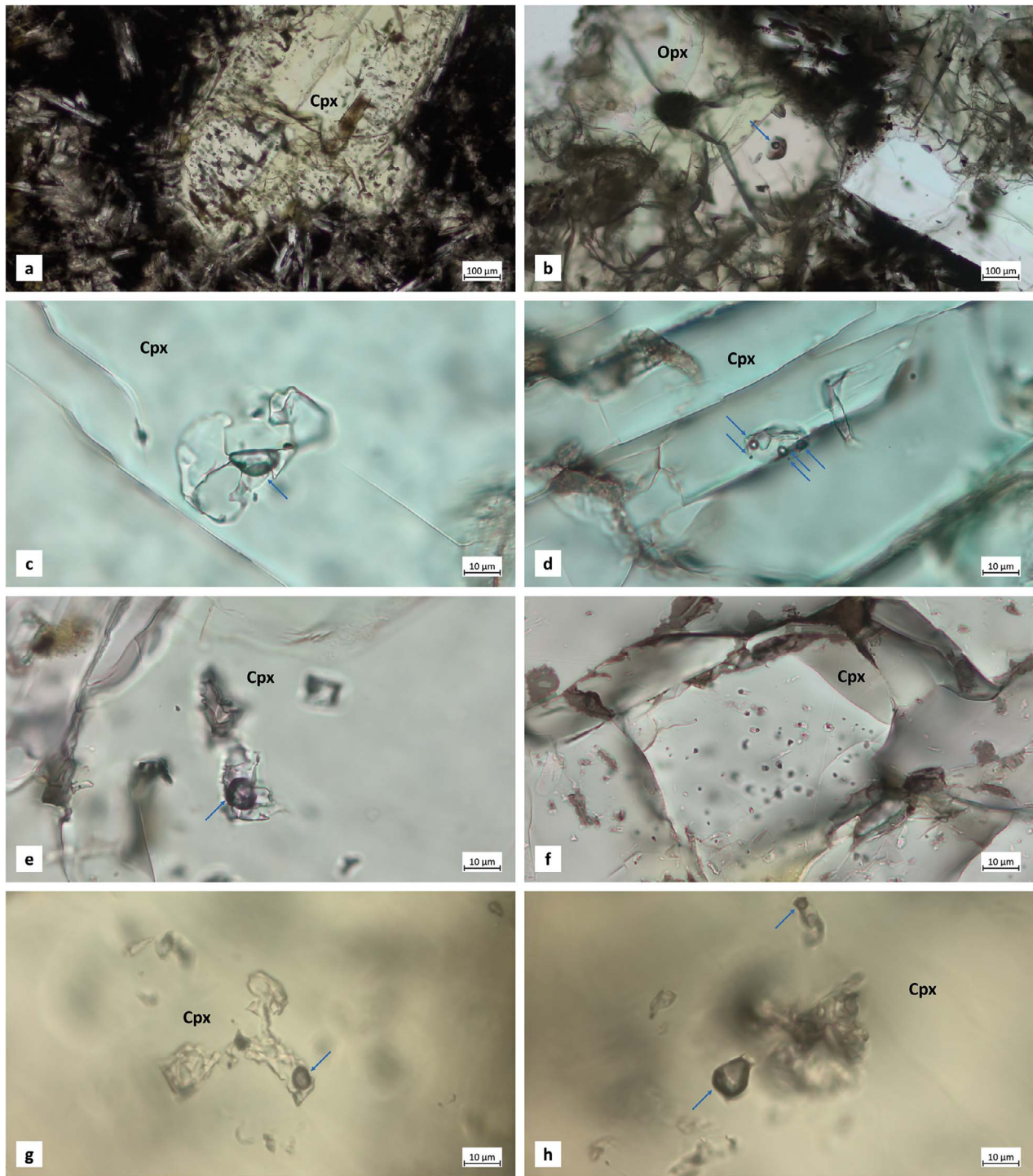


Fig. 5. Photomicrographs of bubble-bearing MIs within glomerocrysts, from both CAMP and Deccan. Representative photomicrographs of bubble-bearing MIs within glomerocrysts in transmitted, plane polarized light. Light blue arrows indicate bubbles within MIs. a) Augitic Cpx crystal containing abundant bubble-bearing MIs within a glomerocryst (sample NEW31, CAMP, USA). Bubble-bearing MIs are clearly clustered from rim to mantle of this Cpx crystal, suggesting a change in crystal growth. b) Enstatitic Opx crystal containing a big single-bubble MI within a glomerocryst (sample NS21, CAMP, Canada). This single-bubble MI was reconstructed in 3D by Synchrotron radiation X-ray microtomography (Fig. 12). c) Single-bubble MI with interstitial bubble (sample AL14, CAMP, Portugal). d) Multi-bubble MI with 5 bubbles displaying different sizes (sample NS12, CAMP, Canada). e) Single-bubble MI displaying an irregular shape, made up of two disconnected portions: one of glass and bubble, and the other one of glass only (sample AN18, CAMP, Morocco). f) Cluster of extremely tiny ($\leq 1 \mu\text{m}$ -sized), single-bubble MIs (sample AN137A, CAMP, Morocco). g) Partially crystallized, single-bubble MI displaying an extremely irregular shape (sample BOR14-2, Deccan, India). h) Partially crystallized, single-bubble MI displaying an extremely irregular shape, made up of two disconnected portions and thus resulting in a bubble-dominated inclusion (sample BOR14-2, Deccan, India).

EMP on MIs glass). Compared to the mafic composition of the whole rocks from both CAMP and Deccan, ranging from basalt to basaltic andesite, their MIs glass has an intermediate to felsic

composition and shows a wide variability, ranging from (trachy-) andesite to rhyolite (Fig. 9). The glass of exposed MIs within CAMP rock samples mostly has an intermediate composition

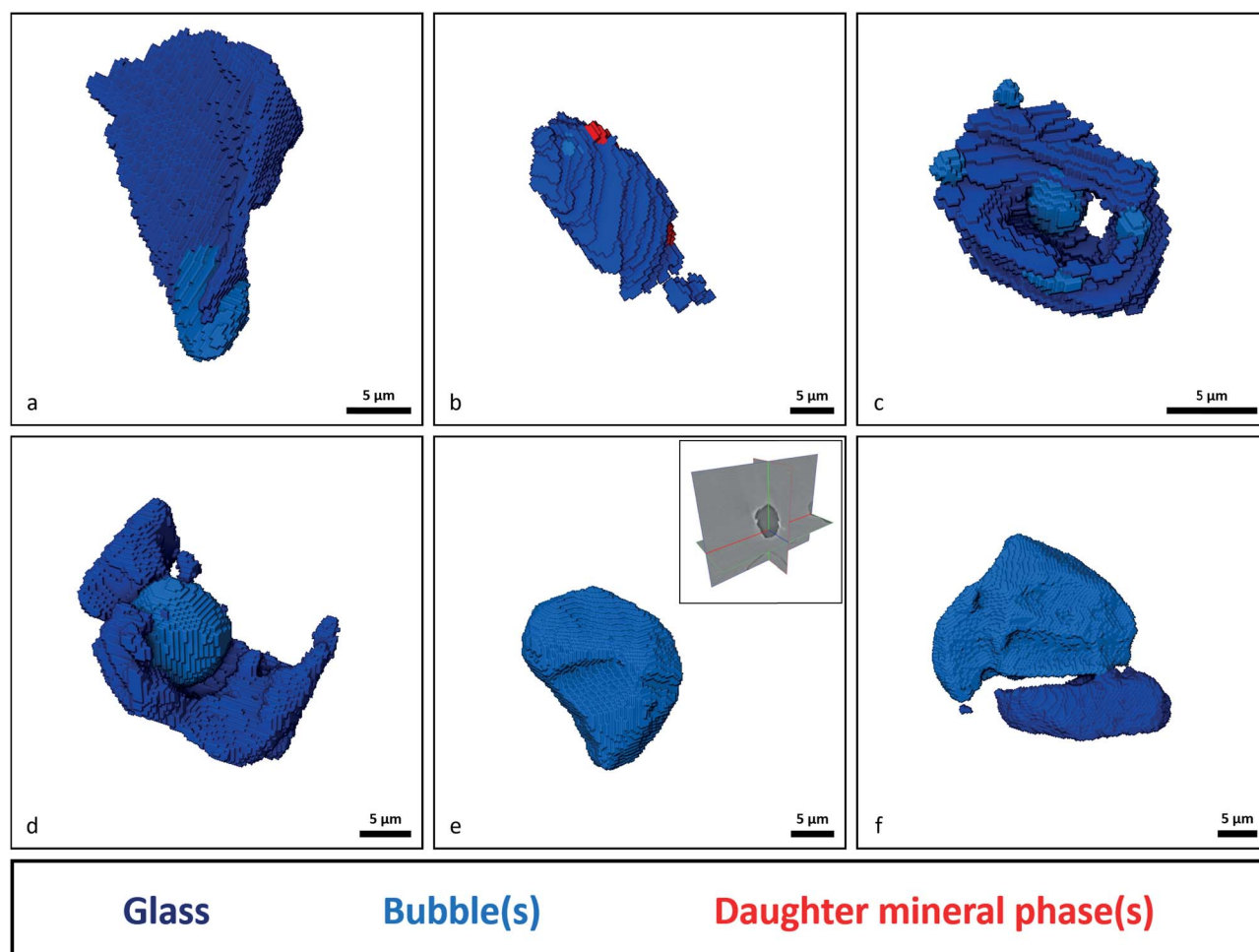


Fig. 6. 3D reconstructions of bubble-bearing MIs, from both CAMP and Deccan. Representative 3D reconstructions of bubble-bearing MIs hosted in Cpx by Synchrotron radiation X-ray microtomography. Bubble-bearing (both single- and multi-bubble) MIs consist of glass (dark blue phase), (gas-bearing) bubble(s) (light blue phase) and daughter mineral phase(s) (likely Mag; red phase). The inset of panel e shows the orthogonal sections of the reconstructed inclusion, consisting of gas only. a) Sample AN137A, CAMP, Morocco. b) Sample NEW73, CAMP, USA. c) Sample NS12, CAMP, Canada. d) Sample MAT14-3, Deccan, India. e-f) Sample PAS14-1, Deccan, India. See [Supplementary Data 1](#) for all the bubble-bearing MIs reconstructed by Synchrotron radiation X-ray microtomography.

(57–63 wt.% SiO₂), whereas the glass of exposed MIs within Deccan rock samples mostly has a felsic composition (>63 wt.% SiO₂). In the analysed MIs glass, SiO₂ displays a positive correlation with Na₂O and K₂O, and a negative correlation with TiO₂ and FeO (as total FeO). In general, the analysed MIs glass shows an evident variability in major element composition for both CAMP and Deccan, even within the same rock samples.

Tiny (μm-sized) crystals that likely formed from the entrapped melt within MIs (i.e., daughter mineral phases) were also analysed in exposed MIs. Kaersutitic amphibole (Amp), enstatitic orthopyroxene (Opx) and hercynitic spinel (Spl) were detected within MIs from sample MAT14-3. Potential thin (<3 μm) rims of Cpx that likely crystallized from the entrapped melt on MIs boundary (i.e., daughter mineral phases) were not analysed because of their small size (similar to the employed EMP beam diameter).

Oxygen isotope composition of host Cpx and MIs glass

The host Cpx of glomerocrysts and the glass of exposed MIs were analysed by SIMS for oxygen isotope composition (see [Supplementary Data 2](#) for all the analytical data; 133 SIMS spots on host Cpx crystals, 93 for the CAMP and 40 for the Deccan; 28 SIMS spots on MIs glass, 21 for the CAMP and 7 for

the Deccan). Oxygen isotope data for host Cpx crystals with an augitic composition were acquired on all rock samples from both CAMP and Deccan, except for sample NS21 that contains host Opx crystals (see [Supplementary Data 3](#) for the photomicrographs of all the sites analysed by SIMS on host Cpx crystals). Measured $\delta^{18}\text{O}_{\text{Cpx}}$ values in glomerocrysts from both CAMP and Deccan range from +3.9 (± 0.3) to +5.8 (± 0.3) ‰ and their sample-averaged $\delta^{18}\text{O}_{\text{Cpx}}$ values span from +4.4 (N=10) to +5.6 (N=10) ‰ ([Tab. 1](#) and [Fig. 10](#)). The analysed glomerocrysts have $\delta^{18}\text{O}_{\text{Cpx}}$ values similar to or slightly lower than typical $\delta^{18}\text{O}$ values of Cpx crystals from mantle peridotites, generally ranging between +5.3 and +5.9 ‰ ([Mattey et al., 1994](#)). Some rock samples (e.g., NEW31, BOR14-2 and KJA14-2) display a high internal variability in measured $\delta^{18}\text{O}_{\text{Cpx}}$ values (up to 1.0 ‰), whereas other rock samples (e.g., AL14, NS12 and MAT14-3) display a low internal variability in measured $\delta^{18}\text{O}_{\text{Cpx}}$ values (down to 0.4 ‰).

Oxygen isotope data for MIs glass were acquired on the only 6 rock samples with MIs large enough to be suitable for SIMS analysis (see [Supplementary Data 3](#) for the photomicrographs of all the sites analysed by SIMS on MIs glass): 5 from the CAMP (samples AL14, AN137A, NEW31, NEW73 and NS21) and 1 from the Deccan (sample BOR14-2). Measured $\delta^{18}\text{O}_{\text{glass}}$ values in exposed MIs from both CAMP and Deccan range from +5.5 (± 0.4) to +22.1 (± 0.4) ‰

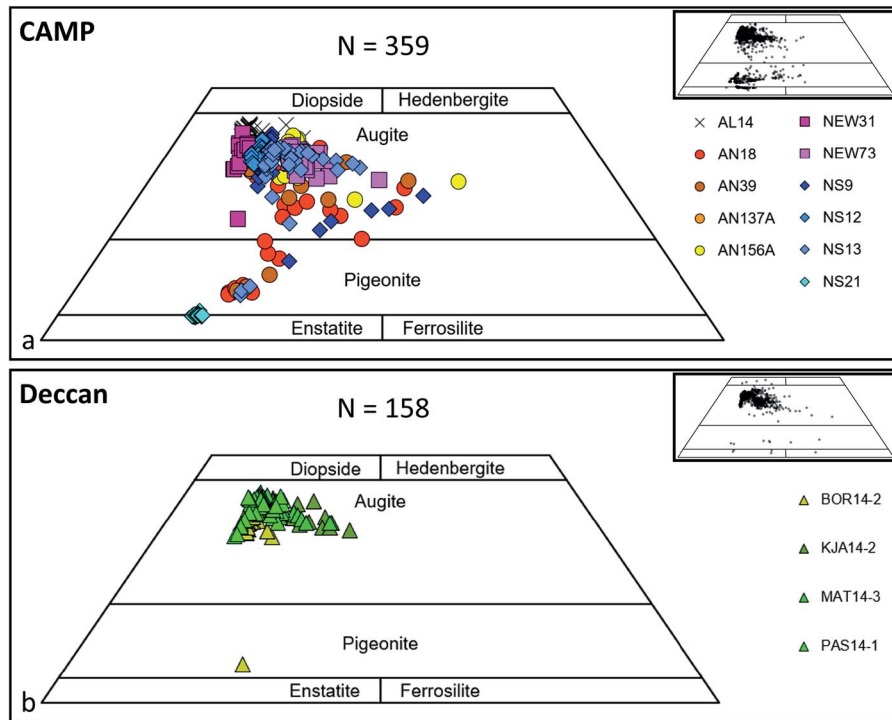


Fig. 7. Classification of host Cpx crystals. a) Host Cpx crystals from CAMP rock samples. b) Host Cpx crystals from Deccan rock samples. The symbols indicate the composition of host Cpx crystals on the ternary wollastonite–enstatite–ferrosilite classification diagram (Morimoto, 1988). In the top right inset of each panel, the grey semi-transparent circles indicate the composition of pyroxenes as glomerocrysts, phenocrysts and microcrysts in effusive rocks and as crystals in intrusive rocks from the literature for the CAMP (De Min *et al.*, 2003; Callegaro *et al.*, 2013, 2014b; Marzoli *et al.*, 2019) and the Deccan (Melluso & Sethna, 2010; Callegaro *et al.*, 2023), respectively. The analysed host Cpx crystals have a mainly augitic and subordinately pigeonitic composition for both CAMP and Deccan, as typical of tholeiitic basalts worldwide. Hence, glomerocryst and non-glomerocryst crystal populations do not display any significant difference in major element composition. See Supplementary Data 2 for all the analytical data.

(Tab. 2 and Fig. 10). The analysed MIs have extremely variable $\delta^{18}\text{O}_{\text{glass}}$ values, even within the same rock samples (e.g., NEW31, NS21 and BOR14-2). Although some measured $\delta^{18}\text{O}_{\text{glass}}$ values overlap typical $\delta^{18}\text{O}$ values of mantle-derived basaltic melts, generally ranging between +5.3 and +5.9 ‰ (Eiler *et al.*, 2000; Bindeman, 2008), most of them are substantially higher, approaching typical $\delta^{18}\text{O}$ values of sedimentary and some metamorphic rocks, even > +20.0 ‰ (Bindeman, 2008). In general, $\delta^{18}\text{O}_{\text{glass}}$ is significantly higher than $\delta^{18}\text{O}_{\text{Cpx}}$ in all the analysed rock samples from both CAMP and Deccan. The lowest $\delta^{18}\text{O}_{\text{glass}}$ values (i.e., those overlapping typical $\delta^{18}\text{O}$ values of mantle-derived basaltic melts) are from samples AN137A, NEW31 and BOR14-2, and the highest ones (i.e., those approaching typical $\delta^{18}\text{O}$ values of crustal rocks) are from samples AL14 and NEW73. Interestingly, the 2 analysed rock samples of the Newark Basin (sample NEW31 from the Orange Mountain Basalt and sample NEW73 from the Hook Mountain Basalt), display contrasting $\delta^{18}\text{O}_{\text{glass}}$ values.

Combining data from the present and previous studies on oxygen isotopes from both CAMP and Deccan (see Supplementary Materials for oxygen isotope composition), the $\delta^{18}\text{O}_{\text{glass}}$ values of MIs from this study are among the highest oxygen isotope compositions reported for both these LIPs. Excluding hydrothermal materials of pipes and veins from the North Mountain Basalt in North America (Kontak & Dostal, 2010), the highest oxygen isotope composition reported in the literature for the CAMP is +12.0 ‰ $\delta^{18}\text{O}$ on zircon and baddeleyite crystals from the Tarabuco sill in South America (Davies *et al.*, 2021), whereas the highest measured $\delta^{18}\text{O}_{\text{glass}}$ value of MIs from this study is +22.1 (± 0.4) ‰ for the CAMP. Interestingly, the highest oxygen isotope composition reported in the literature for the Deccan is +17.0 ‰ $\delta^{18}\text{O}$ on

the red boles (Ghosh *et al.*, 2006), whereas the highest measured $\delta^{18}\text{O}_{\text{glass}}$ value of MIs from this study is +16.2 (± 0.5) ‰ for the Deccan.

Volatile content of bubbles within MIs

Confocal Raman microspectroscopy data on the volatile content of bubbles within MIs are presented for Deccan rock samples only (see Supplementary Data 2 for all the analytical data; 18 Raman spots on bubbles from 16 MIs for the Deccan). The volatile content of bubbles within MIs for all CAMP rock samples was previously analysed (Capriolo *et al.*, 2020). Most of the analysed bubbles resulted to be empty, albeit potentially containing volatile species below the detection limit, and were thus not reported in the present study. Only CO_2 was detected within the bubbles of 16 single-bubble MIs from all Deccan rock samples (Fig. 11). No other volatile species (i.e., elemental C, CH_4 , SO_2 , H_2S and H_2O) were detected within the same CO_2 -bearing bubbles. In the Raman spectrum of CO_2 , the distance between the two main bands (known as Fermi diad or doublet) is directly proportional to its density (Rosso & Bodnar, 1995), allowing to determine the CO_2 density within the analysed bubbles. Applying the densimeter calibration of Kawakami *et al.* (2003), which is optimal for mafic systems and low-density fluids (Hartley *et al.*, 2014; Lamadrid *et al.*, 2017), the CO_2 within the analysed bubbles displays a density of about 0.1 g/cm³, ranging from a minimum of 0.086 g/cm³ to a maximum of 0.138 g/cm³.

Synchrotron radiation X-ray microtomography provides quantitative data of higher precision compared to optical observations (see Supplementary Data 2 for all the analytical data; 16 reconstructed glomerocrysts, 13 for the CAMP and 3 for the Deccan;

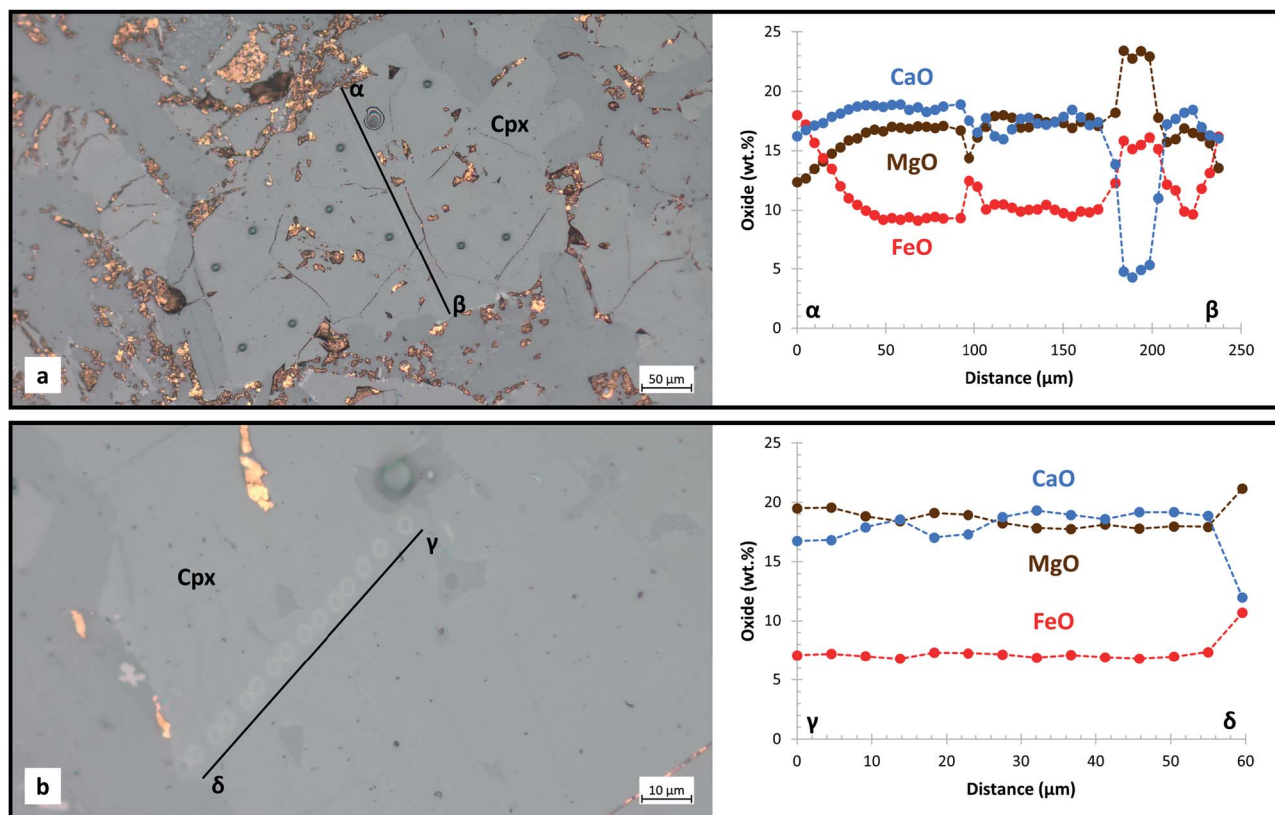


Fig. 8. Transects for CaO, FeO (as total FeO) and MgO of host Cpx crystals within glomerocrysts. a) Rim (α) to rim (β) transect of a Cpx crystal aggregate forming a glomerocryst (sample NS13, CAMP, Canada). The analysed host Cpx has a mostly augitic composition, and the broken line profile of this transect reveals the polycrystalline nature of the crystal aggregate. b) Inclusion (γ) to rim (δ) transect of a Cpx crystal within a glomerocryst (sample NEW31, CAMP, USA). The analysed host Cpx has a homogeneous augitic composition from the exposed MI to the crystal rim. In both photomicrographs (at different magnification in reflected, plane polarized light), analytical spots (larger for SIMS and smaller for EMP) and interstitial residues of gold coating are visible on the surface of the rock samples. See [Supplementary Data 3](#) for the photomicrographs in reflected, plane polarized light of all the sites analysed by SIMS and EMP on host Cpx crystals and MIs glass.

12 reconstructed MIs, 9 for the CAMP and 3 for the Deccan). X-ray microtomography data show a clear density contrast between bubbles, glass, host and daughter mineral phases of MIs, and display a broad range in terms of volume proportions between these phases (Figs. 6 and 12). The bubble/inclusion fraction of a MI is the ratio between the volume occupied by (gas-bearing) bubble(s) and the volume occupied by the whole MI (i.e., melt + bubble(s) + daughter mineral phase(s) within the inclusion). X-ray microtomography data indicate that 0.1–0.2 is the prevalent bubble/inclusion fraction for primary MIs within rock samples from both CAMP and Deccan, in agreement with volume estimates based on optical microscopy. However, X-ray microtomography data display a wide spectrum of bubble/inclusion fractions for primary MIs, from 0.07 to 0.68, and exceptionally up to 1, reflecting a variability from inclusions consisting of glass with a minimum amount of (gas-bearing) bubble(s), to those entirely consisting of gas.

Combining data from the present and previous studies on MIs from both CAMP and Deccan (see Supplementary Materials for volatile budget), the average density of glass is 2.6 g/cm^3 for an intermediate composition (Emerson, 1990), the average CO_2 density of bubbles is 0.1 g/cm^3 , and the minimum volume fraction of bubbles within MIs is 0.07. The minimum bubble/inclusion fraction, obtained by Synchrotron radiation X-ray microtomography, corresponds to the amount of volatiles directly exsolved from the entrapped melt within MIs, assuming negligible post-entrapment processes. Hence, the concentration of CO_2 in CAMP and Deccan

melts represented by the analysed MIs is conservatively about 0.3 wt.%, that is:

$$\text{CO}_2 = (0.1 \text{ g/cm}^3 \times 0.07) / \{ [0.1 \text{ g/cm}^3 \times 0.07] + [2.6 \text{ g/cm}^3 \times (1-0.07)] \} \times 100 \text{ wt.} \% = 0.29 \text{ wt.} \%$$

DISCUSSION

The investigated glomerocrysts containing abundant bubble-bearing MIs are found in several lava flows from both CAMP and Deccan (Supplementary Fig. 2). Textural, chemical and isotopic evidence indicates that glomerocrysts and their MIs formed in a dynamic mush-dominated plumbing system. The analysed glomerocrysts (Figs. 3 and 4) are interpreted as preserved fragments of a crystal mush formed by sintering in a transcrustal plumbing system. The analysed MIs (Figs. 5 and 6) are interpreted as μm - to tens of μm -sized pockets of interstitial multiphase magma (i.e., silicate melt \pm exsolved fluids \pm precipitated crystals) entrapped in or between growing crystals within the crystal mush during magma crystallization.

Textural evidence of a mush-dominated plumbing system

All the analysed rock samples are lava flows containing Cpx-dominated glomerocrysts, characterized by MI-rich and MI-free

Table 1: Dataset of $\delta^{18}\text{O}$ values of host Cpx crystals. In CAMP rock samples, the analysed host Cpx crystals display $\delta^{18}\text{O}$ values between +4.80 and +5.17 ‰ for Portugal (sample AL14), between +4.27 and +5.24 ‰ for Morocco (samples AN18, AN39, AN137A and AN156A), between +4.02 and +5.63 ‰ for USA (samples NEW31 and NEW73), and between +4.65 and +5.79 ‰ for Canada (samples NS9, NS12 and NS13). In Deccan rock samples, the analysed host Cpx crystals display similar $\delta^{18}\text{O}$ values, between +4.52 and +5.54 ‰ (sample BOR14-2), or lower $\delta^{18}\text{O}$ values, between +3.89 and +4.90 ‰ (samples KJA14-2, MAT14-3 and PAS14-1). See [Supplementary Data 2](#) for all the analytical data.

	$\delta^{18}\text{O}$	2σ		$\delta^{18}\text{O}$	2σ		$\delta^{18}\text{O}$	2σ
	(‰)	(\pm ‰)		(‰)	(\pm ‰)		(‰)	(\pm ‰)
AL14_1_Cpx_01	4.95	0.31	NEW31_1_Cpx_01	5.26	0.36	BOR14-2_Cpx_01	5.16	0.38
AL14_1_Cpx_02	4.80	0.34	NEW31_1_Cpx_02	4.88	0.32	BOR14-2_Cpx_02	5.11	0.33
AL14_1_Cpx_03	4.88	0.31	NEW31_1_Cpx_03	5.22	0.35	BOR14-2_Cpx_03	4.95	0.35
AL14_1_Cpx_04	4.83	0.31	NEW31_1_Cpx_04	5.12	0.33	BOR14-2_Cpx_04	5.32	0.32
AL14_1_Cpx_05	4.82	0.31	NEW31_1_Cpx_05	5.63	0.32	BOR14-2_Cpx_05	5.11	0.36
AL14_1_Cpx_06	4.95	0.33	NEW31_1_Cpx_06	5.26	0.32	BOR14-2_Cpx_06	4.91	0.35
AL14_1_Cpx_07	5.04	0.31	NEW31_1_Cpx_07	4.96	0.35	BOR14-2_Cpx_07	5.54	0.38
AL14_1_Cpx_08	4.90	0.31	NEW31_1_Cpx_08	5.34	0.34	BOR14-2_Cpx_08	5.35	0.32
AL14_1_Cpx_09	5.17	0.31	NEW31_1_Cpx_09	5.24	0.35	BOR14-2_Cpx_09	4.93	0.33
AL14_1_Cpx_10	5.09	0.35	NEW31_1_Cpx_10	5.12	0.38	BOR14-2_Cpx_10	4.52	0.33
			NEW73_2_Cpx_01	4.51	0.33	KJA14-2_Cpx_01	3.89	0.34
			NEW73_2_Cpx_02	4.56	0.34	KJA14-2_Cpx_02	4.25	0.35
			NEW73_2_Cpx_03	4.68	0.37	KJA14-2_Cpx_03	4.31	0.36
AN18_2_Cpx_04	4.42	0.36	NEW73_2_Cpx_04	4.12	0.33	KJA14-2_Cpx_04	4.18	0.34
AN18_2_Cpx_05	4.69	0.33	NEW73_2_Cpx_05	4.40	0.37	KJA14-2_Cpx_05	4.58	0.34
AN18_2_Cpx_06	4.46	0.34	NEW73_2_Cpx_06	4.65	0.36	KJA14-2_Cpx_06	4.29	0.33
			NEW73_2_Cpx_07	4.17	0.36	KJA14-2_Cpx_07	4.49	0.34
AN18_2_Cpx_08	4.98	0.32	NEW73_2_Cpx_08	4.49	0.33	KJA14-2_Cpx_08	4.51	0.41
			NEW73_2_Cpx_09	4.02	0.36	KJA14-2_Cpx_09	4.19	0.40
						KJA14-2_Cpx_10	4.90	0.40
AN39_1_Cpx_01	5.00	0.34	NS9_1_Cpx_01	5.34	0.33	MAT14-3_4_Cpx_01	4.42	0.34
AN39_1_Cpx_02	5.15	0.33	NS9_1_Cpx_02	5.46	0.33	MAT14-3_4_Cpx_02	4.58	0.32
AN39_1_Cpx_03	5.06	0.38	NS9_1_Cpx_03	5.18	0.32	MAT14-3_4_Cpx_03	4.54	0.33
AN39_1_Cpx_04	4.56	0.31	NS9_1_Cpx_04	5.13	0.31	MAT14-3_4_Cpx_04	4.69	0.35
AN39_1_Cpx_05	4.85	0.33	NS9_1_Cpx_05	5.35	0.41	MAT14-3_4_Cpx_05	4.81	0.33
AN39_1_Cpx_06	5.24	0.31	NS9_1_Cpx_06	5.02	0.34	MAT14-3_4_Cpx_06	4.65	0.45
AN39_1_Cpx_07	5.06	0.37	NS9_1_Cpx_07	5.62	0.34	MAT14-3_4_Cpx_07	4.83	0.32
AN39_1_Cpx_08	4.79	0.33	NS9_1_Cpx_08	5.49	0.33	MAT14-3_4_Cpx_08	4.51	0.32
AN39_1_Cpx_09	4.68	0.32	NS9_1_Cpx_09	5.58	0.33	MAT14-3_4_Cpx_09	4.42	0.32
AN39_1_Cpx_10	4.97	0.34	NS9_1_Cpx_10	5.58	0.32	MAT14-3_4_Cpx_10	4.55	0.39
AN137A_2_Cpx_01	4.84	0.35	NS12_3_Cpx_01	4.83	0.40	PAS14-1_3_Cpx_01	4.23	0.34
AN137A_2_Cpx_02	4.78	0.33	NS12_3_Cpx_02	4.80	0.32	PAS14-1_3_Cpx_02	4.40	0.33
AN137A_2_Cpx_03	4.77	0.31	NS12_3_Cpx_03	4.65	0.32	PAS14-1_3_Cpx_03	4.33	0.32
AN137A_2_Cpx_04	4.95	0.36	NS12_3_Cpx_04	4.76	0.33	PAS14-1_3_Cpx_04	4.42	0.37
AN137A_2_Cpx_05	4.79	0.39	NS12_3_Cpx_05	4.82	0.32	PAS14-1_3_Cpx_05	4.52	0.35
AN137A_2_Cpx_06	5.01	0.33	NS12_3_Cpx_06	4.88	0.38	PAS14-1_3_Cpx_06	4.44	0.38
AN137A_2_Cpx_07	5.24	0.39	NS12_3_Cpx_07	4.71	0.36	PAS14-1_3_Cpx_07	4.70	0.36
AN137A_2_Cpx_08	4.69	0.35	NS12_3_Cpx_08	4.88	0.32	PAS14-1_3_Cpx_08	4.22	0.33
AN137A_2_Cpx_09	4.98	0.36	NS12_3_Cpx_09	4.88	0.40	PAS14-1_3_Cpx_09	4.42	0.41
AN137A_2_Cpx_10	5.17	0.34	NS12_3_Cpx_10	5.05	0.34	PAS14-1_3_Cpx_10	4.38	0.35
AN156A_2_Cpx_01	4.57	0.35	NS13_2_Cpx_01	5.28	0.34			
AN156A_2_Cpx_02	4.36	0.31	NS13_2_Cpx_02	5.56	0.34			
AN156A_2_Cpx_03	4.55	0.32	NS13_2_Cpx_03	5.79	0.32			
AN156A_2_Cpx_04	4.52	0.31	NS13_2_Cpx_04	5.76	0.34			
AN156A_2_Cpx_05	4.54	0.32	NS13_2_Cpx_05	5.61	0.37			
AN156A_2_Cpx_06	4.32	0.31	NS13_2_Cpx_06	5.34	0.38			
AN156A_2_Cpx_07	4.27	0.33	NS13_2_Cpx_07	5.79	0.34			
AN156A_2_Cpx_08	4.49	0.31	NS13_2_Cpx_08	5.50	0.32			
AN156A_2_Cpx_09	4.28	0.33	NS13_2_Cpx_09	5.73	0.35			
AN156A_2_Cpx_10	4.77	0.31	NS13_2_Cpx_10	5.31	0.32			

Table 2: Dataset of $\delta^{18}\text{O}$ values of MIs glass. The measured $\delta^{18}\text{O}_{\text{glass}}$ values are significantly higher than the measured $\delta^{18}\text{O}_{\text{Cpx}}$ values in all the investigated rock samples from both CAMP and Deccan. Sample AL14 yielded 1 rhyolitic MI with +21.05 ‰ $\delta^{18}\text{O}$. Sample AN137A yielded 2 andesitic MIs with respectively +5.47 and +6.81 ‰ $\delta^{18}\text{O}$. Sample NEW31 yielded 10 (trachy-) andesitic MIs with $\delta^{18}\text{O}$ values ranging from +12.05 to +16.05 ‰, exceptionally down to +6.67 ‰ in the case of the most evolved MI. Sample NEW73 yielded 4 dacitic to trachytic MIs with $\delta^{18}\text{O}$ values ranging from +17.47 to +22.14 ‰. Sample NS21 yielded 1 andesitic MI with +7.64 ‰ $\delta^{18}\text{O}$ and 1 dacitic MI with +15.06 ‰ $\delta^{18}\text{O}$. Sample BOR14-2 yielded 7 dacitic to trachytic and rhyolitic MIs with $\delta^{18}\text{O}$ values ranging from +5.70 to +16.15 ‰. See [Supplementary Data 2](#) for all the analytical data.

	$\delta^{18}\text{O}$	2σ		$\delta^{18}\text{O}$	2σ
	(‰)	(± ‰)		(‰)	(± ‰)
AL14_1_MIb	21.05	0.34	NEW73_2_MIa	20.50	0.37
			NEW73_2_MIg_A	19.73	0.35
AN137A_2_MIa	5.47	0.38	NEW73_2_MIg_B	19.45	0.40
AN137A_4_MIa	6.81	0.37	NEW73_3_MIa	22.14	0.40
			NEW73_3_MIe	17.47	0.37
NEW31_1_MIb	14.34	0.39			
NEW31_1_MIa	7.95	0.33	NS21_1_MIa	15.06	0.42
NEW31_1_MIf	6.67	0.41	NS21_1_MIf	7.64	0.34
NEW31_1_MIe	7.89	0.33			
NEW31_1_MId	14.63	0.32	BOR14-2_bis_MIe	7.81	0.35
NEW31_1bis_MIa	13.48	0.57	BOR14-2_bis_MIg	15.96	0.36
NEW31_1bis_MIb	12.89	0.46	BOR14-2_bis_MIf	6.82	0.33
NEW31_1bis_MIi	14.13	0.40	BOR14-2_bis_MIh	5.70	0.31
NEW31_1bis_MIk	12.05	0.36	BOR14-2_bis_MIa	9.38	0.35
NEW31_1bis_MIo	15.73	0.34	BOR14-2_bis_MIb	6.14	0.31
NEW31_1bis_MIl	14.99	0.38	BOR14-2_bis_MId	16.15	0.45

portions (Supplementary Fig. 5). The lack of any interstitial (microcrystalline or glassy) groundmass between glomerocryst-forming crystals rules out the hypothesis of accidental crystal clustering prior to eruption, whereas the random orientation of glomerocryst-forming crystals and the irregular shape of their grain boundaries exclude the hypothesis of compaction after synneusis in a magma chamber (Holness *et al.*, 2019). The irregular shape of primary MIs and their net-like distribution in specific sectors of Cpx crystal domains hint at an original interconnection between interstitial melt pockets (Gleeson *et al.*, 2023). These domains likely correspond to rapid growth zones, where MIs are the relics of an effective (i.e., open) porosity, turned into an ineffective (i.e., closed) porosity due to the crystal growth along melt-saturated boundaries. Input of new magma batches and volatile fluxing or exsolution in magma reservoirs are potential trigger mechanisms for a rapid crystal growth (Hort, 1998), which may clog the interconnected pores of the crystal framework occupied by melt and bubbles, leading to their entrapment as MIs (Supplementary Fig. 5). The presence of MIs throughout growth shells of single crystals within the glomerocrysts (Supplementary Fig. 3) points to intra-crystal melt entrapment, whereas the presence of MIs between individual crystals within the same glomerocrysts (Supplementary Fig. 3) points to inter-crystal melt entrapment during rapid growth of the crystal framework (McCarthy *et al.*, 2020). The occurrence of daughter mineral phases as μm -sized crystals within partially crystallized MIs or as a μm -thick rim of Cpx along their boundary (Supplementary Fig. 3) implies post-entrapment crystallization, that is the precipitation of a mineral phase from the melt after its entrapment into MIs (Kress & Ghiorso, 2004; Steele-MacInnis *et al.*, 2011). In addition, the occasional evidence of ductile to brittle deformation within glomerocryst-forming crystals and phenocrysts (Supplementary Fig. 4), as well as the presence of pseudosecondary MIs, indicate multiple fragmentation and remobilization events of the crystal framework in the magma

plumbing system (Bindeman, 2005; Cooper & Kent, 2014; Jackson *et al.*, 2018; Marzoli *et al.*, 2022).

Synchrotron radiation X-ray microtomography reveals a wide spectrum of bubble/inclusion fractions in primary MIs, from those with dominant glass (0.93 vol.%) to those without any glass and with pure fluid only (Fig. 6). The great variability of bubble/inclusion fractions indicates that in most cases the melt was entrapped along with an already exsolved fluid phase after migrating along crystal-melt interfaces, determining a heterogeneous entrapment (Steele-MacInnis *et al.*, 2017). In a scenario of heterogeneous entrapment, most of the empty bubbles analysed by confocal Raman microspectroscopy are likely to be gas exsolution bubbles that lost their original volatile content (likely because of a fluid phase loss via microcracks), rather than shrinkage bubbles that nucleated after the entrapment of a volatile-free melt. Furthermore, multi-bubble MIs prove that volatile-bearing bubbles did not all coalesce after melt entrapment, and the oblate or prolate spheroidal shape of bubbles within MIs without any morphological constraints reveals a post-entrapment oriented stress (Caricchi *et al.*, 2011). Since a vitrifying melt always shrinks after entrapment, the minimum bubble/inclusion fraction is exclusively determined by post-entrapment shrinkage. Hence, the minimum bubble/inclusion fraction of 0.07, reconstructed by Synchrotron radiation X-ray microtomography in the analysed MIs, corresponds to the amount of volatiles directly exsolved from the entrapped melt (Moore *et al.*, 2015). However, uncertainties derived from post-entrapment processes may slightly affect the bubble/inclusion fraction (Kress & Ghiorso, 2004; Steele-MacInnis *et al.*, 2011). For instance, post-entrapment crystallization at the interface between the entrapped melt and the host mineral phase (e.g., Cpx on MIs boundary) modifies the volume proportions within MIs. Fractional and equilibrium crystallization may thus have occurred within MIs and throughout the magma plumbing system of both CAMP and Deccan, as further supported by chemical evidence of a mush-dominated plumbing system.

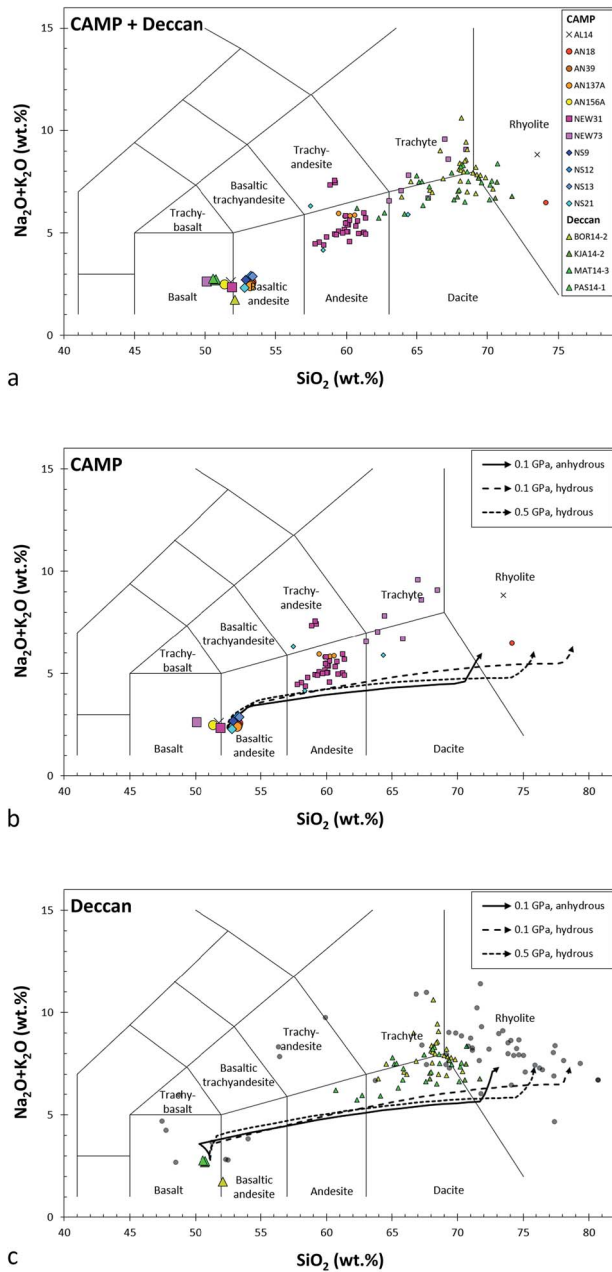


Fig. 9. Classification of MIs glass and whole rocks along with fractional crystallization (FC) models. a) Classification diagram for CAMP and Deccan rock samples. b) FC models for CAMP rock samples. c) FC models for Deccan rock samples, along with mafic to felsic whole rock compositions from the literature (Halder et al., 2023). The small symbols indicate the composition of MIs glass, and the large symbols indicate the composition of whole rocks (hosting the glomerocrysts containing the MIs) on the SiO₂ vs. Na₂O+K₂O (TAS) classification diagram (Le Maitre, 2002). The grey semi-transparent circles indicate the composition of mafic to felsic rocks in the Deccan from the literature. The lines indicate potential FC paths up to ca. 10 wt.% residual melt at different conditions (0.1 GPa for anhydrous compositions, and 0.1 and 0.5 GPa for hydrous compositions). All data are plotted after recalculation at 100 wt.% (volatile-free). The analysed MIs glass has an intermediate to felsic composition, ranging from (trachy-) andesite to rhyolite, whereas the corresponding whole rocks have a mafic composition, ranging from basalt to basaltic andesite, for both CAMP and Deccan. The whole rock compositions of all the investigated rock samples are from the literature (sample AL14 from Callegaro et al., 2014b; samples AN18, AN39, AN137A and AN156A from Marzoli et al., 2019; samples NEW31, NEW73, NS9, NS12, NS13 and NS21 from Merle et al., 2014; samples BOR14-2, KJA14-2, MAT14-3 and PAS14-1 from Callegaro et al., 2023). See Supplementary Data 2 for all the analytical data.

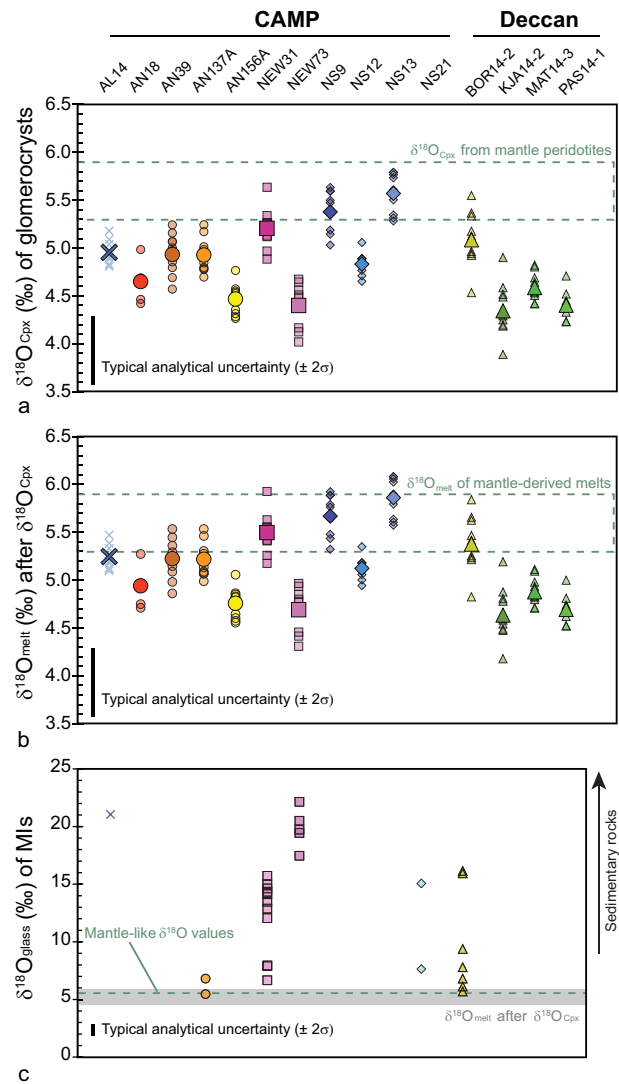


Fig. 10. Plots of δ¹⁸O values of host Cpx crystals and MIs glass. a) Plot of δ¹⁸O_{Cpx} values of glomerocrysts, compared to the typical δ¹⁸O values of Cpx crystals from mantle peridotites, ranging from +5.3 to +5.9‰ (Mattey et al., 1994). b) Plot of δ¹⁸O_{melt} values calculated after δ¹⁸O_{Cpx} values, using a fractionation factor Δ_{melt-Cpx} of +0.3‰ (Taylor et al., 1984; Harris et al., 2005), compared to the typical δ¹⁸O values of mantle-derived basaltic melts, ranging from +5.3 to +5.9‰ (Eiler et al., 2000; Bindeman, 2008). c) Plot of δ¹⁸O_{glass} values of MIs, compared to the typical mantle-like δ¹⁸O values and the calculated δ¹⁸O_{melt} values. The small symbols indicate the single δ¹⁸O values per rock sample, and the large symbols indicate the sample-averaged δ¹⁸O values per rock sample. Compared to the measured δ¹⁸O_{Cpx} values and the calculated δ¹⁸O_{melt} values, the measured δ¹⁸O_{glass} values of MIs are significantly higher in all the investigated rock samples from both CAMP and Deccan. See Supplementary Data 2 for all the analytical data.

Chemical evidence of a mush-dominated plumbing system

The analysed pyroxene crystals from glomerocrysts are MgO-rich and, apart from rare enstatitic Opx, these are mostly augitic Cpx and subordinately pigeonitic Cpx in both CAMP and Deccan rock samples (Fig. 7). The major element composition of the analysed glomerocrysts is typical of pyroxene crystals in tholeiitic basalts, including these two LIPs (De Min et al., 2003; Melluso & Sethna, 2010; Callegaro et al., 2013, 2014b, 2023; Marzoli et al., 2019). In addition, the reconstructed crystallization sequence of pyroxene

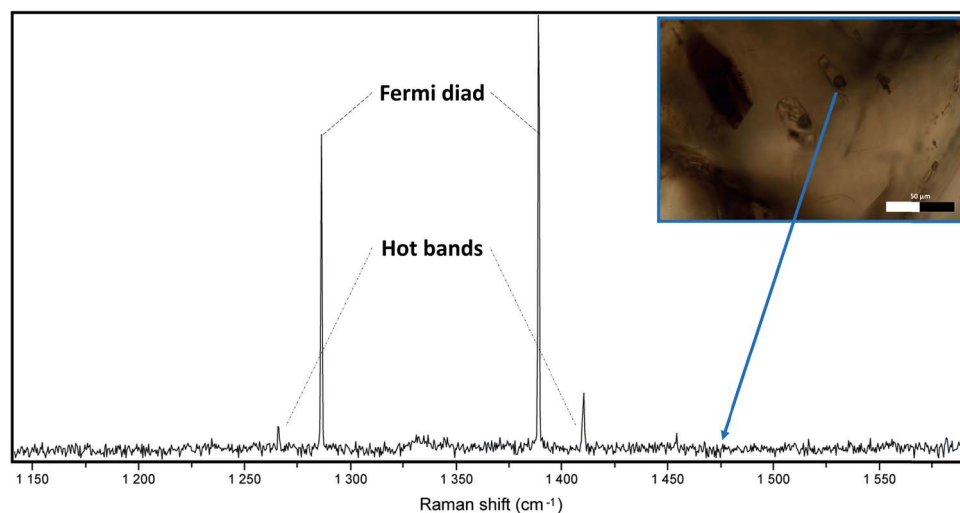


Fig. 11. Raman spectrum of CO₂ from the bubble within a single-bubble MI. Representative Raman spectrum of CO₂ from the bubble within a single-bubble MI (sample PAS14-1, Deccan, India). The Raman spectrum of CO₂ is characterized by two main bands (at about 1285 and 1388 cm⁻¹, known as Fermi diad or doublet) and two symmetrical minor bands (respectively below 1285 cm⁻¹ and above 1388 cm⁻¹, known as hot bands) due to the resonance effect (Frezzotti *et al.*, 2012).

and plagioclase, followed by oxides, is typical of tholeiitic continental flood basalts (Chin *et al.*, 2018; Bédard *et al.*, 2021). The analysed MIs glass is SiO₂-rich and MgO-poor, displaying an intermediate to felsic composition (from (trachy-) andesite to rhyolite) in both CAMP and Deccan rock samples (Fig. 9). Conversely, the investigated rock samples have a mafic whole rock composition (from basalt to basaltic andesite) for both CAMP and Deccan (Merle *et al.*, 2014; Callegaro *et al.*, 2014b, 2023; Marzoli *et al.*, 2019).

The investigated MIs from both CAMP and Deccan indicate a CO₂ concentration of at least 0.3 wt.% for the entrapped melts. Although H₂O was never detected within bubbles of the investigated MIs, the local occurrence of kaersutitic Amp as daughter mineral phase within MIs from the Deccan indicates a H₂O concentration of up to 4 wt.% for the same entrapped melts (Merzbacher & Egger, 1984). The calculated CO₂ concentration in mafic to felsic melts is consistent with a maximum entrapment pressure of about 0.5 GPa at CO₂-H₂O fluid-saturated conditions (Tamic *et al.*, 2001; Shishkina *et al.*, 2010). This pressure constraint suggests a maximum entrapment depth of about 15 km for a pressure/depth gradient of 0.03 GPa/km. Apart from CO₂, the absence of SO₂, H₂S and H₂O within all the analysed bubbles of MIs is consistent with a deep volatile exsolution since SO₂, H₂S and H₂O exsolve at lower pressure than CO₂ (Wallace & Edmonds, 2011; Baker & Alletti, 2012; Boulliung & Wood, 2022; Ding *et al.*, 2023). Up to >90 % of the total CO₂ budget of MIs is in the bubbles, as they generally contain about one order of magnitude more CO₂ than the coexisting glass (Steele-MacInnis *et al.*, 2011; Hartley *et al.*, 2014; Moore *et al.*, 2015; Capriolo *et al.*, 2020).

Likely due to the different rheology of the entrapped melts, the two investigated LIPs differ in the presence of multi- versus single-bubble MIs (Figs. 2 and 6). In CAMP rock samples, where MIs glass is less evolved (i.e., intermediate SiO₂ content, thus relatively less viscous), MIs often contain several bubbles, thus many nuclei formed for bubbles in the source melt. On the contrary, in Deccan rock samples, where MIs glass is more evolved (i.e., high SiO₂ content, thus relatively more viscous), MIs mostly contain a single bubble, thus only few nuclei formed for bubbles in the source melt. In both cases, the melt and nucleated bubbles were randomly entrapped and then quenched in different volume proportions within MIs because of melt-fluid decoupling

(Caricchi *et al.*, 2018). Notably, a single bubble is energetically favoured rather than several bubbles within a specific volume of viscous melt (Shea, 2017). The dominant presence of single-bubble MIs in the Deccan may also imply either a lower degree of CO₂ saturation (Mourtada-Bonnefoi & Laporte, 2002), or a heating episode that induced coalescence without decrepitation (Faure & Schiano, 2004), after an evolution analogous to that forming the multi-bubble MIs in the CAMP. The rhyolitic composition of MIs glass and the basaltic composition of whole rocks were modelled to quantify the viscosity of the investigated felsic and mafic melts, using sample AL14 (Callegaro *et al.*, 2014b). Oxygen fugacity was set to the QFM buffer, pressure was set to 0.1 GPa, and temperature was set to 1100 °C in all models. Applying a viscosity model for silicate melts (Giordano *et al.*, 2008), the viscosity of the rhyolitic melt is 41.1 kPa × s, and the viscosity of the basaltic melt is 0.1 kPa × s, suggesting a great variability in the rheology of melts during the evolution of the magma plumbing system.

Differentiation by fractional and equilibrium crystallization possibly combined with crustal assimilation may explain the evolved composition of MIs glass in comparison with whole rocks and their Cpx crystals. Post-entrapment crystallization may also have occurred within some MIs, as supported by the presence of daughter mineral phases, such as oxides as well as anhydrous and hydrous silicates (Supplementary Fig. 3). In the case of the CAMP, the major element composition of intermediate MIs glass (sample NEW31) may correspond to a residual melt after crystallization of about 39 wt.% augitic Cpx, 11 wt.% Pl and 5 wt.% Mag from a typical CAMP basalt, carrying out a simple mass balance calculation (Capriolo *et al.*, 2020). Similarly, in the case of the Deccan, the major element composition of felsic MIs glass (sample MAT14-3) may correspond to a residual melt after crystallization of about 34 wt.% kaersutitic Amp, 23 wt.% augitic Cpx and 10 wt.% enstatitic Opx from a typical Deccan basalt, carrying out a simple mass balance calculation combining the analysed MIs glass, host and daughter mineral phases from this study and their whole rock composition from the literature (Callegaro *et al.*, 2023). Part of this differentiation may have occurred after MIs formation as post-entrapment crystallization (Kress & Ghiorso, 2004; Steele-MacInnis *et al.*, 2011). However, the limited volumes of daughter mineral phases within the investigated MIs point to

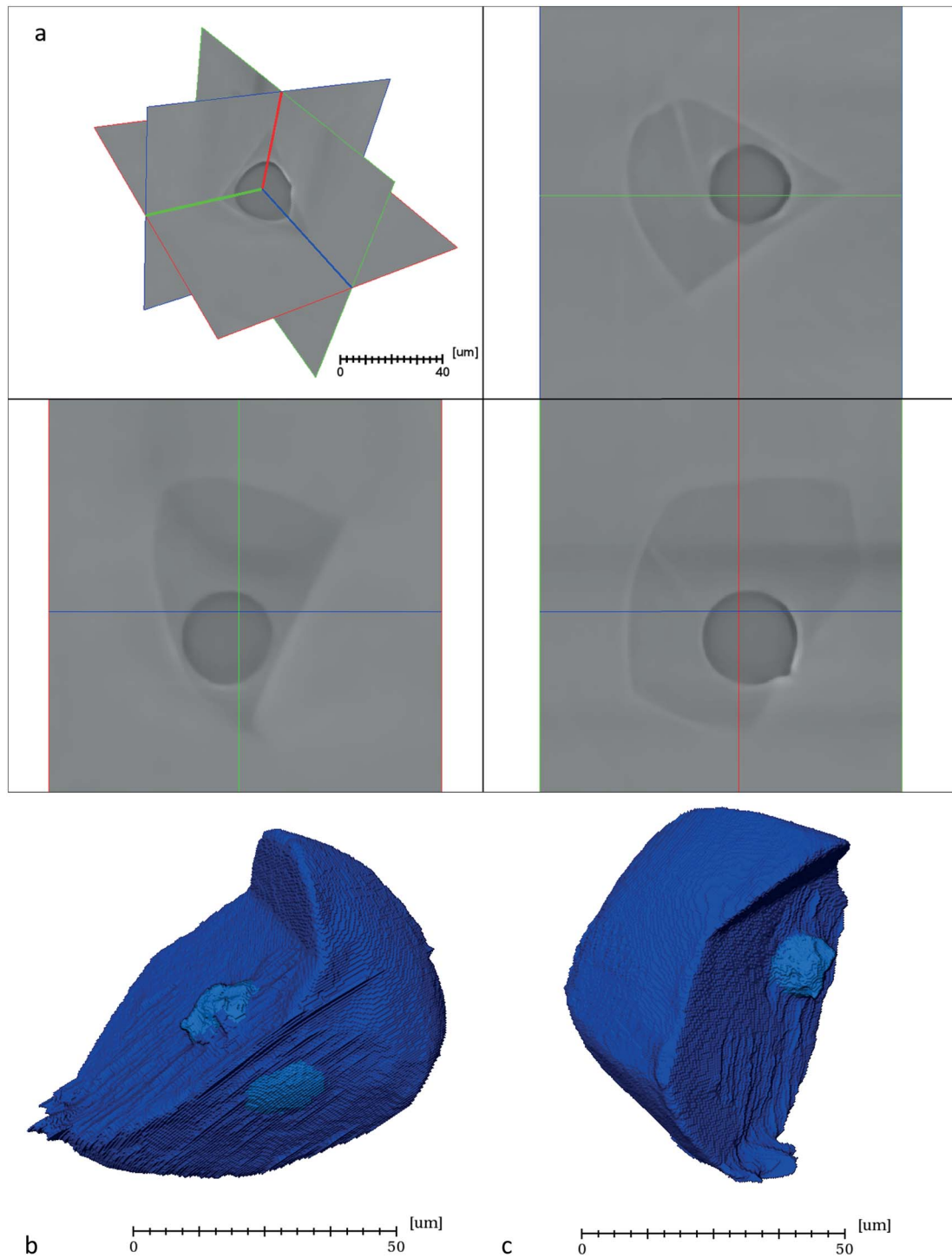


Fig. 12. 3D reconstruction of a bubble-bearing MI. Representative 3D reconstruction of a large bubble-bearing MI hosted in Opx by Synchrotron radiation X-ray microtomography. a) Orthogonal sections of a large bubble-bearing MI (sample NS21, CAMP, Canada). The darker region corresponds to the CO₂-bearing bubble of MI, the intermediate region corresponds to the glass of MI and the brighter region corresponds to the host mineral phase (Opx). b-c) 3D reconstruction of the same large bubble-bearing MI from two different perspectives. The dark blue phase corresponds to the glass and the light blue phase corresponds to the CO₂-bearing bubble.

post-entrapment crystallization as a marginal process in driving MIs differentiation. Fractional and equilibrium crystallization may have occurred at different times and depths throughout the transcrustal plumbing system, as supported by geochemical and petrological evidence in both CAMP and Deccan. Most of the lava flows from both these LIPs have a basaltic composition, which represents ca. 30–50 wt.% residual melt after crystallization

of a primary mantle melt (Marzoli *et al.*, 2018, 2019, 2022; Krishnamurthy, 2020b). Strongly evolved (SiO₂ > 57 wt.%) rocks are absent throughout all the CAMP, but are locally present in the Deccan (Cucciniello *et al.*, 2019, 2020; Basu *et al.*, 2020; Krishnamurthy, 2020a, 2020b; O'Connor *et al.*, 2022; Halder *et al.*, 2023). Interestingly, the major element composition of evolved Deccan rocks is similar to that of the analysed MIs glass (Supplementary Figs. 6

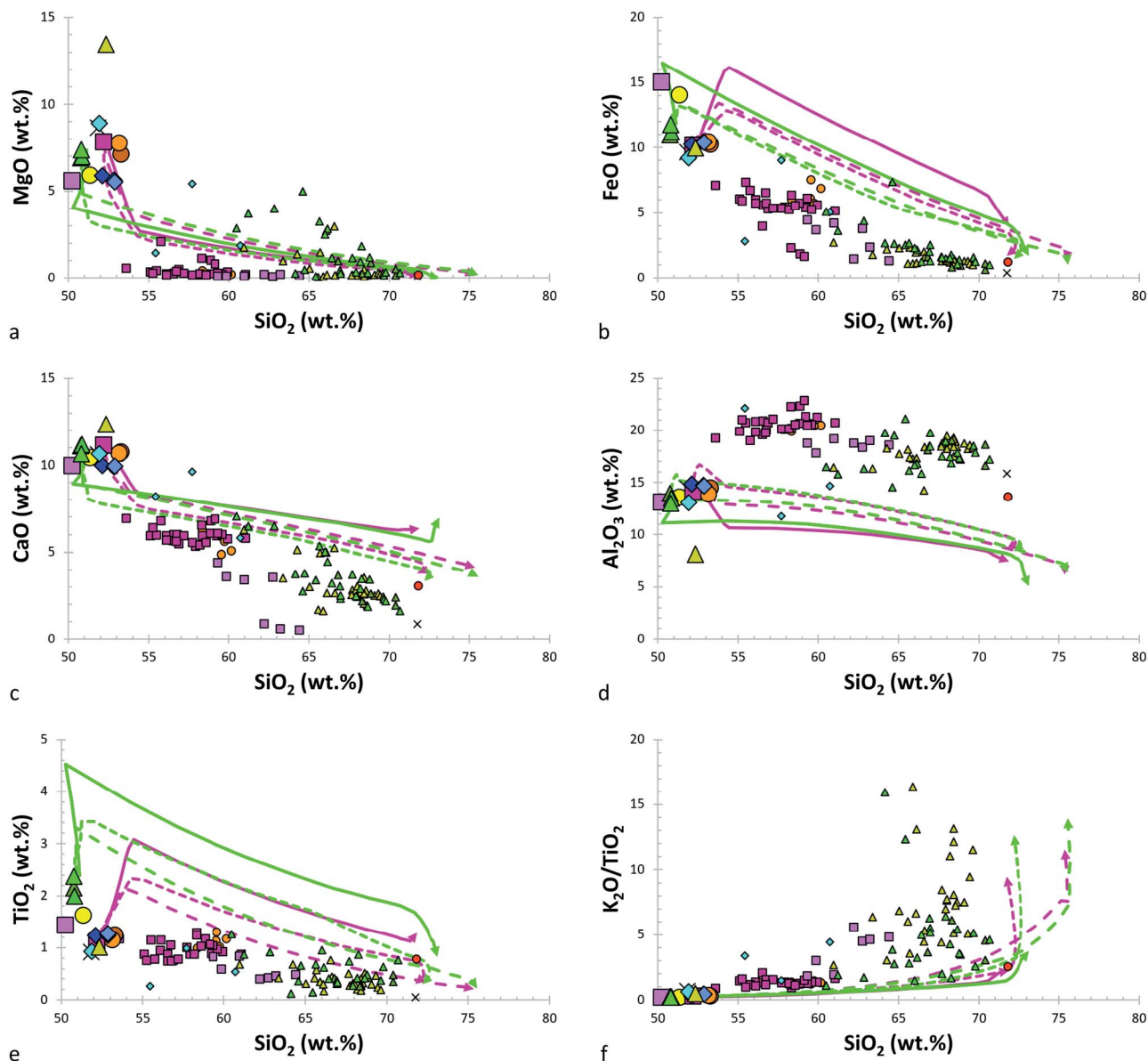


Fig. 13. Fractional crystallization (FC) models in comparison with the composition of MIs glass and whole rocks, in terms of SiO₂ versus other major element oxides and K₂O/TiO₂ ratio. a) SiO₂ vs. MgO. b) SiO₂ vs. FeO. c) SiO₂ vs. CaO. d) SiO₂ vs. Al₂O₃. e) SiO₂ vs. TiO₂. f) SiO₂ vs. K₂O/TiO₂. The lines indicate potential FC paths up to ca. 10 wt.% residual melt at different conditions (purple lines for the CAMP and green lines for the Deccan; same line legend of Fig. 9). The small symbols indicate the composition of MIs glass, and the large symbols indicate the composition of whole rocks (hosting the glomerocrysts containing the MIs; same symbol legend of Fig. 9). All data are plotted without any recalculation (EMP data for MIs glass have totals between 92.00 and 101.00 wt.%), and Fe is reported as total FeO. In the plot of SiO₂ vs. K₂O/TiO₂, the only MI glass from sample AL14 plots off the scale (K₂O/TiO₂ ~ 81). The whole rock compositions of all the investigated rock samples are from the literature (same references of Fig. 9).

and 7). The chemical contrast between the mafic composition of whole rocks and the intermediate to felsic composition of their MIs glass hints at the bimodal magmatism that fits the paradigm of crystal mush reservoirs (Jackson *et al.*, 2018).

In order to test the closed-system differentiation process (Figs. 9 and 13), fractional crystallization was simulated using Rhyolite-MELTS (code version 1.2.0; Gualda *et al.*, 2012), starting from the parental melt composition of a typical basalt from both CAMP and Deccan. Sample NEW31 (Merle *et al.*, 2014) was employed as the starting composition for CAMP models, whereas sample PAS14-1 (Callegaro *et al.*, 2023) was employed as the starting composition for Deccan models. Oxygen fugacity was set to the QFM buffer in all models, pressure was set to 0.1 GPa for anhydrous compositions, and to 0.1 and 0.5 GPa for hydrous (0.5 wt.% H₂O in the starting melt) compositions, in order to

test different depths throughout the magma plumbing system. According to the modelled paths, fractional crystallization alone cannot explain the evolved composition of MIs glass. In particular, the measured Al₂O₃ and Na₂O+K₂O contents in MIs glass are higher than the modelled ones, whereas the measured FeO, CaO and TiO₂ contents in MIs glass are lower than the modelled ones in both CAMP and Deccan. Crustal assimilation may thus have accompanied fractional crystallization of CAMP and Deccan magmas, as further supported by isotopic evidence of a mush-dominated plumbing system.

Isotopic evidence of a mush-dominated plumbing system

The measured $\delta^{18}\text{O}_{\text{Cpx}}$ values of the investigated glomerocrysts display a moderate variability, ranging from +3.9 (\pm 0.3) to

+5.8 (± 0.3) ‰ (Fig. 10). The corresponding sample-averaged $\delta^{18}\text{O}_{\text{Cpx}}$ values display a narrower variability, ranging from +4.4 ($N=10$) to +5.6 ($N=10$) ‰ (Fig. 10). Some of the measured $\delta^{18}\text{O}_{\text{Cpx}}$ values overlap the typical $\delta^{18}\text{O}_{\text{Cpx}}$ values from mantle peridotites (Fig. 10), which range between +5.3 and +5.9 ‰ (Mattey et al., 1994). All the other analysed host crystals yielded relatively low $\delta^{18}\text{O}_{\text{Cpx}}$ values (Fig. 10), which may result either from high-temperature hydrothermal alteration, from assimilation of crustal material that was hydrothermally altered, or from a mantle source that involved recycled lithosphere (Bindeman et al., 2006; Genske et al., 2013; Hartley et al., 2013; Troch et al., 2020; Xu et al., 2021). Although some local, minor alteration may have occurred, the hypothesis of diffuse high-temperature hydrothermal alteration may be discarded since petrographic observations and major element compositions of Cpx crystals do not show any evidence of alteration (see Supplementary Data 3 for the photomicrographs of all the sites analysed by SIMS on host Cpx crystals). The hypothesis of assimilation of crustal material that was hydrothermally altered may be discarded as well since this process would have partially affected MIs too, but their $\delta^{18}\text{O}_{\text{glass}}$ values are inconsistent with this hypothesis in all the investigated rock samples. Lastly, the hypothesis of a mantle source that involved recycled lithosphere is supported by extensive geochemical evidence especially in the CAMP. For CAMP basaltic rocks, their geochemical composition suggests a mantle source enriched by subduction events, with minor evidence of mantle plume components (Chalokwu et al., 1999; Deckart et al., 2005; Kontak & Dostal, 2010; Merle et al., 2011, 2014; Callegaro et al., 2013, 2014b; Bertrand et al., 2014; Whalen et al., 2015; Marzoli et al., 2019; Boscaini et al., 2022). For Deccan basaltic rocks, their geochemical composition suggests significant time-related compositional changes, from an early continental lithosphere signature to a late mantle plume source (Mahoney et al., 1982; Matsuhisa et al., 1986; Peng et al., 1994, 1998; Peng & Mahoney, 1995; Melluso et al., 2006; Sheth & Melluso, 2008; Bhattacharya et al., 2013; Peters et al., 2017).

In order to estimate the $\delta^{18}\text{O}$ values of the melt from which Cpx crystals grew (Figs. 10 and 14), a fractionation factor between melt and Cpx crystals ($\Delta_{\text{melt-Cpx}} = +0.3$ ‰; Taylor et al., 1984; Harris et al., 2005) was applied to the measured $\delta^{18}\text{O}_{\text{Cpx}}$ values. The sample-averaged $\delta^{18}\text{O}$ values of the melt ($\delta^{18}\text{O}_{\text{melt}}$ values) calculated from the measured $\delta^{18}\text{O}_{\text{Cpx}}$ values range from +4.7 ($N=10$) to +5.9 ($N=10$) ‰ (Fig. 10). Apart from few rock samples displaying slightly lower values, the calculated $\delta^{18}\text{O}_{\text{melt}}$ values generally overlap the typical $\delta^{18}\text{O}$ values of mantle-derived basaltic melts, which span from +5.3 to +5.9 ‰ (Eiler et al., 2000; Bindeman, 2008). In summary, although few rock samples likely recorded a heterogeneous mantle source with slightly low $\delta^{18}\text{O}$ values, the analysed glomerocrysts crystallized from mantle-derived mafic melts.

The measured $\delta^{18}\text{O}_{\text{glass}}$ values of the investigated MIs display a high variability, ranging from +5.5 (± 0.4) to +22.1 (± 0.4) ‰ (Fig. 10), clearly indicating isotopic disequilibrium between MIs glass and their host Cpx crystals in most of the analysed rock samples from both CAMP and Deccan. Only a few of the measured $\delta^{18}\text{O}_{\text{glass}}$ values overlap the calculated $\delta^{18}\text{O}_{\text{melt}}$ values and the typical $\delta^{18}\text{O}$ values of mantle-derived basaltic melts (Fig. 10), which range between +5.3 and +5.9 ‰ (Eiler et al., 2000; Bindeman, 2008). All the other analysed MIs yielded high $\delta^{18}\text{O}_{\text{glass}}$ values (Fig. 10), which approach the typical $\delta^{18}\text{O}$ values of sedimentary and some metamorphic rocks (Bindeman, 2008). These extreme $\delta^{18}\text{O}_{\text{glass}}$ values are too high to result from closed-system differentiation processes alone (e.g., fractional

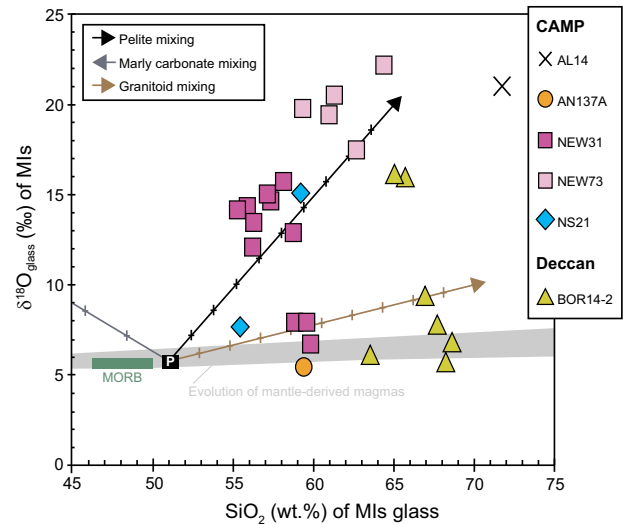


Fig. 14. Crustal assimilation models in comparison with the composition of MIs glass, in terms of SiO_2 versus $\delta^{18}\text{O}$. The lines indicate crustal assimilation paths for potential different assimilants (black, grey and brown lines), starting from a mantle-derived parental melt (P), and the symbols indicate the composition of MIs glass for both CAMP and Deccan. The green area indicates the composition of mid-ocean ridge basalts (MORB), and the grey area indicates the evolution of mantle-derived magmas, reflecting a closed-system differentiation process for a basaltic parental melt (Troch et al., 2020). Most of the analysed MIs fall outside the array of mantle-derived magmas, pointing to an open-system differentiation process. All data are plotted without any recalculation (EMP data for MIs glass have totals between 92.00 and 101.00 wt.%).

crystallization of a mantle-derived parental melt), and may result either from low-temperature hydrothermal alteration, from post-entrapment crystallization, or from open-system differentiation processes (Bindeman, 2008). Although some local, minor alteration may have occurred, the hypothesis of diffuse low-temperature hydrothermal alteration may be discarded since petrographic observations and major element compositions of MIs glass do not show any evidence of alteration (see Supplementary Data 3 for the photomicrographs of all the sites analysed by SIMS on MIs glass). Moreover, the analysed MIs yielding the highest $\delta^{18}\text{O}_{\text{glass}}$ values display a correlation between their SiO_2 content and their $\delta^{18}\text{O}$ value (e.g., sample NEW73), whereas low-temperature hydrothermal alteration would have resulted in less systematic data trends (i.e., more scattered data). The hypothesis of post-entrapment crystallization may be discarded as well since the analysed MIs display $\delta^{18}\text{O}_{\text{glass}}$ values up to +22.1 ‰, whereas crystallization of mineral phases such as Cpx and Pl at magmatic temperatures would have resulted in a very minor fractionation of oxygen isotopes (<0.5 ‰; Taylor & Sheppard, 1986). Furthermore, the sites potentially affected by evident post-entrapment crystallization were carefully avoided for SIMS analysis, the presence of daughter mineral phases at sub- μm scale would have not affected the measurement as the SIMS analytical spot is about 10 μm , and no noticeable changes of oxygen count rates and oxygen isotope ratios (pointing to the analysis of different materials such as crystals) were observed during SIMS analysis. Similarly, the occurrence of boundary layer effects (Kent, 2008) related to post-entrapment crystallization may be excluded as well since no correlation between MIs size and their $\delta^{18}\text{O}_{\text{glass}}$ values was observed. Lastly, the hypothesis of open-system differentiation processes (e.g., assimilation of crustal material) is supported by extensive geochemical evidence

Table 3: Conditions employed in the four oxygen diffusion models. For each model, different conditions were employed in terms of temperature, number of time steps, duration of each time step, total duration, oxygen diffusivity in the melt and oxygen diffusivity in the crystal. See [Supplementary Data 4](#) for oxygen diffusion models as multimedia files.

Model	Temperature	Number of time steps	Duration of each time step (yr)	Total duration (yr)	Oxygen diffusivity in the melt		Oxygen diffusivity in the crystal	
	(°C)				(m ² /s)	Bibliographic reference	(m ² /s)	Bibliographic reference
1	900	10	10	100	7.2×10^{-14}	Zhang & Ni, 2010	1.3×10^{-20}	Farver, 1989
2	900	10	1000	10 000	7.2×10^{-14}	Zhang & Ni, 2010	1.9×10^{-28}	Ryerson & McKeegan, 1994
3	1100	10	10	100	5.4×10^{-13}	Zhang & Ni, 2010	3.8×10^{-19}	Farver, 1989
4	1100	10	1000	10 000	5.4×10^{-13}	Zhang & Ni, 2010	1.8×10^{-25}	Ryerson & McKeegan, 1994

in both CAMP and Deccan. For CAMP lava flows, their geochemical composition indicates up to 10 wt.% crustal assimilation (Merle *et al.*, 2011, 2014; Callegaro *et al.*, 2013, 2014b; Marzoli *et al.*, 2019). For Deccan lava flows from the Kalsubai Subgroup (e.g., sample BOR14-2), their geochemical composition indicates significant crustal contamination by the continental lithosphere (Mahoney *et al.*, 1982; Peng *et al.*, 1994, 1998; Peng & Mahoney, 1995; Melluso *et al.*, 2006; Sheth & Melluso, 2008). The wide range in $\delta^{18}\text{O}_{\text{glass}}$ values of the investigated MIs, along with their variability in major element compositions (Supplementary Fig. 8), points to variable amounts of crustal assimilation and/or to the involvement of chemically and isotopically heterogeneous assimilants, such as sedimentary rocks from shallow basins and crystalline rocks from potentially different depths throughout the transcrustal section (Bindeman, 2008; Bindeman *et al.*, 2016).

In order to test the open-system differentiation process (Fig. 14), crustal assimilation was simulated using simple binary mixing models with different potential assimilants. For the mantle-derived parental melt, the SiO₂ content (51.0 wt.%) and the $\delta^{18}\text{O}$ value (+5.7 ‰) are from the literature (Eiler *et al.*, 2000; Bindeman, 2008; Merle *et al.*, 2014; Callegaro *et al.*, 2014b, 2023; Marzoli *et al.*, 2019). For the potential assimilants, including pelite (65.0 wt.% SiO₂ and +20.0 ‰ $\delta^{18}\text{O}$), marly carbonate (25.0 wt.% SiO₂ and +20.0 ‰ $\delta^{18}\text{O}$) and granitoid (70.0 wt.% SiO₂ and +10.0 ‰ $\delta^{18}\text{O}$), both the SiO₂ content and the $\delta^{18}\text{O}$ value are from the literature (Bindeman, 2008; Rudnick & Gao, 2014). Samples AL14 and NEW73 from the CAMP yielded measured $\delta^{18}\text{O}_{\text{glass}}$ values > +20 ‰ (Figs. 10 and 14), indicating that the entrapped melt is dominated by crustal components, likely with a (meta-) sedimentary origin (e.g., pelite). The other investigated rock samples from the CAMP yielded measured $\delta^{18}\text{O}_{\text{glass}}$ values < +20 ‰ (Figs. 10 and 14), suggesting a lesser degree of contamination from a similar assimilant (e.g., pelite) or the involvement of a different assimilant (e.g., granitoid). Sample BOR14-2 from the Deccan yielded measured $\delta^{18}\text{O}_{\text{glass}}$ values between +6 and +16 ‰ (Figs. 10 and 14), indicating the involvement of crystalline and/or metasedimentary components (e.g., granitoid, metapelite), as sedimentary basins are absent in the Western Ghats. In summary, the analysed MIs entrapped intermediate to felsic melts with normal (i.e., mantle-like) to extremely high $\delta^{18}\text{O}$ values, typical of (meta-) sedimentary rocks.

The variability of the measured $\delta^{18}\text{O}$ values of Cpx crystals and their MIs suggests a dynamic evolution of the crystal mush reservoirs for both CAMP and Deccan. The bimodal distribution of $\delta^{18}\text{O}_{\text{glass}}$ values in some rock samples (NEW31, NS21 and BOR14-2) may result either from variable amounts of crustal contamination by similar or different assimilants, from the combination of open- and closed-system differentiation processes involving different assimilants, or from the local oxygen isotope re-equilibration

between MIs and host Cpx crystals. As a mineral phase, Cpx preserves magmatic signatures as it is refractory to oxygen isotope diffusional exchange (Taylor *et al.*, 1984; Dallai *et al.*, 2004; Deegan *et al.*, 2021). Nonetheless, post-entrapment oxygen isotope exchange between the silicate melt/glass of MIs and their host mineral phase and the subsequent oxygen isotope diffusion in the host mineral phase may have partially re-equilibrated the measured $\delta^{18}\text{O}$ values (Farver, 1989, 2010; Cole & Chakraborty, 2001; Cherniak & Dimanov, 2010; Zhang & Ni, 2010).

In order to test the oxygen isotope re-equilibration (see Supplementary Data 4 for oxygen diffusion models), exchange of oxygen isotopes between melt and crystals and diffusion of oxygen isotopes in the same crystals were simulated using a 1D diffusion model between two media with different oxygen diffusivity (Hickson *et al.*, 2011). Finite difference equations were solved via Crank-Nicholson method. The 1D diffusion model was run without any fractionation of oxygen isotopes between a 50 µm-wide MI, with an initial $\delta^{18}\text{O}$ value of +22.0 ‰, and the host Cpx crystal (simplified to diopsidic composition), with an initial $\delta^{18}\text{O}$ value of +5.5 ‰. Fractionation of oxygen isotopes is negligible as the isotopic fractionation factor at the modelled temperatures is small (<1; Bindeman *et al.*, 2004). Four different models were run (Tab. 3), using oxygen diffusivities in the melt and in the crystal from the literature (Farver, 1989; Ryerson & McKeegan, 1994; Zhang & Ni, 2010). According to the modelled re-equilibration, oxygen isotope diffusion may potentially re-equilibrate the $\delta^{18}\text{O}_{\text{glass}}$ values of MIs down to +9.0 ‰ in 100 years. Since most of the analysed rock samples display a broad variability in terms of $\delta^{18}\text{O}_{\text{glass}}$, oxygen isotope diffusion can explain the $\delta^{18}\text{O}_{\text{glass}}$ values of few MIs only, indicating that in general the cooling was too fast (in the order of years or decades) to allow MIs and their host Cpx crystals to re-equilibrate isotopically.

Architecture of a mush-dominated plumbing system

The investigated microstructures preserved in lava flows, from the glomerocrysts at the mm-scale to their bubble-bearing MIs at the µm-scale, offer a snapshot of a transient disequilibrium condition driven by volatile exsolution and crustal assimilation in mush-dominated magmatic reservoirs of these two LIPs. The snapshot of this spatial and temporal evolution would otherwise be undetectable at the scale of whole rock samples. Glomerocrysts and their bubble-bearing, evolved MIs are relics of the crystal mush ripped from the magma plumbing system and preserved in lava flows from both CAMP and Deccan. These fragments likely formed during or after volatile exsolution and crustal assimilation, when interstitial CO₂ bubbles and intermediate to felsic melts made crystal-dominated magmas buoyant in the magma plumbing system, enhanced by crystal mush compaction and gas

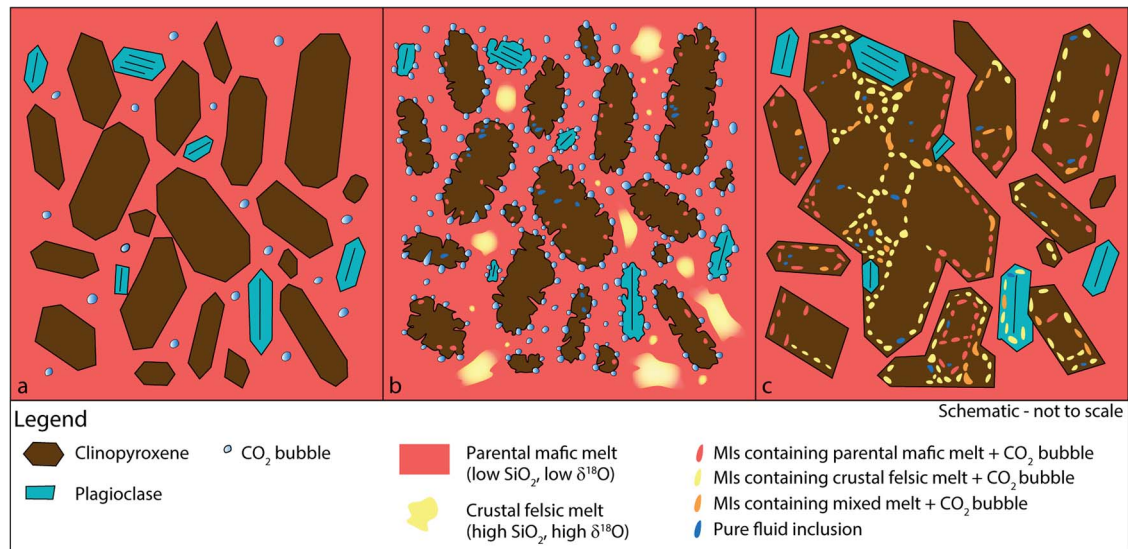


Fig. 15. Sequence of magmatic processes forming glomerocrysts and their bubble-bearing MIs, reconstructed on the basis of textural, chemical and isotopic evidence of a mush-dominated plumbing system. a) Development of a crystal mush in the magma plumbing system, where a primary basaltic melt, Cpx and Pl crystals and exsolved CO₂ coexist. b) Episode of crustal assimilation with a crustal felsic melt entering the system. The increase of volatile content via the assimilated crustal material (CO₂ + H₂O) causes a drop of the solidus with a partial dissolution of the already formed crystals. However, the subsequent volatile exsolution via the system saturation (CO₂ exsolves into bubbles and H₂O remains in the melt because of the depth) causes a rise of the solidus with a rapid crystal growth. Since none of the analysed host Cpx crystals yielded crust-like δ¹⁸O values, the interstitial channels feeding the intra- and inter-crystal pores likely have a very thin (<10 μm) cross section (smaller than the employed SIMS beam diameter). c) New development of a crystal mush in the magma plumbing system, where the rapid crystal growth entraps droplets of different melts (i.e., parental mafic melt, crustal felsic melt or mixed melt) along with CO₂ bubbles. A further CO₂ flux, potentially from assimilated crustal material or from new basaltic magma batches, may speed up the crystal growth. The presence of bubble-bearing evolved melt pockets within the crystal mush may promote the buoyancy of Cpx-dominated glomerocrysts. Hence, potential remobilization events may rip fragments of these solidified portions of the magma plumbing system to Earth's surface, thus found as relics in lava flows.

filter pressing (Anderson *et al.*, 1984; Philpotts *et al.*, 1996). Crustal assimilation includes a broad spectrum of chemical and physical exchange processes between magma and host rocks, mainly driven by partial melts and supercritical fluids entering the multiphase (i.e., solid + liquid + gas phases) magmatic system. Major element and oxygen isotope compositions of host Cpx crystals and their MIs glass indicate the occurrence of two distinct silicate melts (i.e., a parental mafic melt and a crustal felsic melt) within the crystal mush reservoir (Fig. 15). Intermediate to felsic melts, resulting from variable amounts of crustal contamination, were entrapped in MIs during the formation of augitic Cpx crystals, which formed from a mafic melt throughout the magma plumbing system. However, none of the analysed glomerocrysts yielded δ¹⁸O_{Cpx} values and corresponding δ¹⁸O_{melt} values representative of a melt potentially affected by assimilation, indicating that the crustal felsic melt may have been volumetrically minor, and that the entrapment process was too rapid to allow this melt to mix with the parental mafic melt. Potential cycles of dissolution and recrystallization of Cpx crystals, forming MIs, may be triggered and driven by the arrival of new magma batches (of either mantle or crustal origin) and by volatile fluxing or exsolution in the crystal mush reservoirs (Bouvier *et al.*, 2022; Caracciolo *et al.*, 2022).

The development of a transcrustal plumbing system is necessary for the eruptibility of continental LIP magmas, implying that the intrusive activity along with related degassing generally precede the effusive activity, as inferred for several LIPs (Karlstrom & Richards, 2011; Davies *et al.*, 2017; Bédard *et al.*, 2021; Tian & Buck, 2022). The eruptibility of magmas forming extensive continental flood basalts mostly depends on their density, aside from many other parameters, such as temperature, pressure, chemical composition, viscosity and tectonic context. Silicate magmas are typically less dense than their crystallized products

and, if the overburden density is equal to or lower than that of magma, the lithostatic pressure generally prevents magma ascent and eruption, unless crustal discontinuities (e.g., fractures, fault planes and any other anisotropy) are present. Hence, the presence of sedimentary basins and the average felsic composition of the upper crust represent a density barrier for basaltic magmas. Throughout the transcrustal section, the development of a complex magma plumbing system via multiple intrusions and their progressive crystallization increases the overburden density up to and exceeding the eruptibility threshold, triggering the eruption of LIP magmas (Tian & Buck, 2022). Moreover, magmatic intrusions often exploit pre-existing conduits, leading to widespread crustal contamination and ubiquitous magma mixing associated with replenishment (Bédard *et al.*, 2021). During magma ascent to Earth's surface, volatile fluxing or exsolution and crustal assimilation with different degrees of magma mixing increase the pressure and decrease the density of the multiphase system (crystals + melts + fluids) up to and exceeding the eruptibility threshold, triggering the eruption of LIP magmas (Caricchi *et al.*, 2018). The geochemical and microstructural constraints on crystal mush reservoirs in LIPs from this study point to the key role of volatile exsolution and crustal assimilation in driving their open-system evolution. Despite the several differences between CAMP and Deccan, the textural, chemical and isotopic evidence from the analysed glomerocrysts and bubble-bearing MIs indicates a similar architecture of their mush-dominated plumbing system, shaped by transient disequilibrium conditions triggered by multiple episodes of volatile exsolution and crustal assimilation.

The analysed Cpx crystals from glomerocrysts derived from mafic melts, as revealed by δ¹⁸O_{Cpx} values measured on them, and their whole rocks were affected by variable degrees of crustal

assimilation and partial mixing, as revealed by $\delta^{18}\text{O}_{\text{glass}}$ values measured on MIs within them. However, Fe–Mg partition coefficients and predicted versus observed Cpx components indicate a local and limited equilibrium in terms of major element compositions between Cpx crystals from glomerocrysts and their whole rocks. The occurrence of occasional equilibrium conditions allowed the application of Cpx–liquid geothermobarometry, using the major element composition of whole rocks as a liquid. The Cpx crystals from glomerocrysts and their whole rocks were thus employed to estimate the crystallization temperatures and pressures of glomerocrysts, using the major element composition of Cpx crystals from this study and the major element composition of their whole rocks from the literature (Merle *et al.*, 2014; Callegaro *et al.*, 2014b, 2023; Marzoli *et al.*, 2019). Except for sample AN18, sample NS21 that contains Opx crystals and sample BOR14-2 that is a cumulitic rock, all the analysed rock samples from both CAMP and Deccan yielded at least a few geothermobarometry data at equilibrium conditions. Applying different Cpx–liquid geothermobarometry models for silicate melts (Putirka *et al.*, 1996; Putirka *et al.*, 2003; Putirka, 2008; Neave & Putirka, 2017), the estimated crystallization pressures span from the middle to the upper crust (see Supplementary Data 5 for geothermobarometry data), in agreement with previous studies on both CAMP and Deccan (Callegaro *et al.*, 2014b, 2023; Marzoli *et al.*, 2019, 2022; Capriolo *et al.*, 2020). These crystallization pressures are also consistent with the maximum entrapment pressure of about 0.5 GPa, assessed from the calculated CO_2 concentration in mafic to felsic melts at CO_2 – H_2O fluid-saturated conditions. For both these LIPs, the development of a complex magma plumbing system through most of the transcrustal section, up to sedimentary basins in the CAMP, implies several potential sources for carbon, preserved as CO_2 within MIs. Discarding any potential melt–fluid decoupling (Caricchi *et al.*, 2018), the occurrence of both mantle-like and crust-dominated $\delta^{18}\text{O}_{\text{glass}}$ values in the investigated MIs indicate that the CO_2 within their bubbles likely derived from both primary melts and assimilated crustal melts. Hence, the assimilation of carbon-bearing crystalline and sedimentary rocks, such as graphite-bearing schists or gneisses and organic matter-rich shales or sandstones (Svensen *et al.*, 2004; Deegan *et al.*, 2022), may have enriched magmas in CO_2 through the entire transcrustal section.

CONCLUSIONS

Glomerocrysts with abundant bubble-bearing MIs were investigated from several basaltic lava flows of both CAMP and Deccan, via a multi-technique approach combining in situ geochemical and microstructural analysis. In contrast with the traditional model of melt-dominated magma chambers, the analysed microstructures fit very well the more complex paradigm of a mush-dominated plumbing system through most of the transcrustal section (Marsh, 2015; Cashman *et al.*, 2017; Sparks *et al.*, 2019). In this context, the investigated glomerocrysts are fragments of the crystal mush, and their MIs cargo are relics of interstitial melts and fluids (i.e., CO_2) within the porous crystal framework, constituting the magma plumbing system of these mass extinction-related LIPs. Confocal Raman microspectroscopy analysis revealed the presence of CO_2 within bubbles of MIs and allowed the quantification of its density. Synchrotron radiation X-ray microtomography data, in support of optical microscopy observations, allowed the 3D reconstruction of the investigated microstructures and provided a precise estimate of the minimum bubble/inclusion fraction within MIs, which is

fundamental to assess the original volatile budget. These new X-ray microtomography data led to a high-precision refinement of the CO_2 concentration (at least 0.3 wt.%) in CAMP and Deccan melts. Chemical and isotopic constraints from EMP and SIMS data revealed that glomerocrysts formed from a mafic melt with normal (i.e., mantle-like) to slightly low $\delta^{18}\text{O}$ values, derived from mantle melting and fractional crystallization, whereas MIs entrapped distinct, intermediate to felsic melts with normal (i.e., mantle-like) to extremely high $\delta^{18}\text{O}$ values, derived at least partially from crustal assimilation of (meta-) pelites or granitoids. Moreover, isotopic evidence unveils that the CO_2 preserved by MIs likely derived partly from the mantle and partly from assimilated crustal materials. All textural, chemical and isotopic evidence indicates a dynamic evolution for the magma plumbing system of these two LIPs, where crystals, silicate melts and exsolved fluids were continuously coexisting and interacting throughout their transit and temporary storage in the transcrustal section.

FUNDING AND ACKNOWLEDGEMENTS

This work was carried out with the support of Diamond Light Source (UK), instruments I13-2 and I13-Data (experiment MG24552), and of NordSIMS (Sweden), which operates under the grant 2021-00276 of the Swedish Research Council (this is NordSIMS publication 776). M.C. and S.C. acknowledge the support of the Norwegian Research Council for the grant 301096 (MAPLES, Young Research Talents funding scheme) and the grant 22327 (CEED, Centres of Excellence funding scheme). F.M.D. acknowledges the support of the Swedish Research Council for the grant 2022-04569. L.E.A. acknowledges the support of the Programma Nazionale di Ricerche in Antartide (Italy) for the grant PNRA18_00103 (HOT ANTARCTICA). P.R.R. acknowledges the support of the U.S. National Science Foundation for the grants EAR-1736737 and EAR-1615021. B.B.C. acknowledges the support of the University of Padova (Italy) for the grant ‘WelcomeKit’. N.Y. acknowledges the support of the OCP Group (Office Chérifien des Phosphates, Morocco), the UM6P (Mohammed VI Polytechnic University, Morocco), the CNRST (National Center for Scientific and Technical Research, Morocco) and the MESRSI (Ministry of Higher Education, Scientific Research and Innovation, Morocco) for the grant APRD ‘AlkaCarboLipsWac’. A.M. acknowledges the support of the Ministero dell’Università e della Ricerca, Progetti di Ricerca di Interesse Nazionale (Italy), for the grant 20178LPCP. All authors thank L. Tauro (University of Padova) and K. Lindén (Swedish Museum of Natural History) for sample preparation, M. Erambert (University of Oslo) and A. Risplendente (University of Milano) for assistance during EMP analytical sessions, C. Harris (University of Cape Town) for helpful discussions about oxygen isotope geochemistry, the editor M. Humphreys and the anonymous reviewers for useful comments improving this work.

SUPPLEMENTARY DATA

Supplementary data are available at *Journal of Petrology* online.

DATA AVAILABILITY

All data generated in this study are provided in the Supplementary Materials (Supplementary Text, Supplementary Figs. 1–8 and Supplementary Tab. 1) and in the Supplementary Data 1–5. The bibliographic references cited in the Supplementary Materials are the same reported in this paper.

REFERENCES

- Alvarez, L. W., Alvarez, W., Asaro, F. & Michel, H. V. (1980). Extraterrestrial cause for the cretaceous–tertiary extinction. *Science* **208**, 1095–1108. <https://doi.org/10.1126/science.208.4448.1095>.
- Anderson, Jr., A. T., Swihart, G. H., Artioli, G. & Geiger, C. A. (1984). Segregation vesicles, gas filter-pressing, and igneous differentiation. *The Journal of Geology* **92**, 55–72. <https://doi.org/10.1086/628834>.
- Andreasen, R., Peate, D. W. & Brooks, C. K. (2004). Magma plumbing systems in large igneous provinces: inferences from cyclical variations in Palaeogene East Greenland basalts. *Contributions to Mineralogy and Petrology* **147**, 438–452. <https://doi.org/10.1007/s00410-004-0566-2>.
- Baker, D. R. (2008). The fidelity of melt inclusions as records of melt composition. *Contributions to Mineralogy and Petrology* **156**, 377–395. <https://doi.org/10.1007/s00410-008-0291-3>.
- Baker, D. R. & Alletti, M. (2012). Fluid saturation and volatile partitioning between melts and hydrous fluids in crustal magmatic systems: the contribution of experimental measurements and solubility models. *Earth-Science Reviews* **114**, 298–324. <https://doi.org/10.1016/j.earscirev.2012.06.005>.
- Basu, A. R., Chakrabarty, P., Szymanowski, D., Ibañez-Mejía, M., Schoene, B., Ghosh, N. & Georg, R. B. (2020). Widespread silicic and alkaline magmatism synchronous with the Deccan Traps flood basalts. *Earth and Planetary Science Letters* **552**, 116616. <https://doi.org/10.1016/j.epsl.2020.116616>.
- Beane, J. E., Turner, C. A., Hooper, P. R., Subbarao, K. V. & Walsh, J. N. (1986). Stratigraphy, composition and form of the Deccan Basalts, Western Ghats, India. *Bulletin of Volcanology* **48**, 61–83. <https://doi.org/10.1007/BF01073513>.
- Bédard, J. H., Saumur, B. M., Tegner, C., Troll, V. R., Deegan, F. M., Evenchick, C. A., Grasby, S. E. & Dewing, K. (2021). Geochemical systematics of High Arctic Large Igneous Province continental tholeiites from Canada: evidence for progressive crustal contamination in the plumbing system. *Journal of Petrology* **62**, 1–39. <https://doi.org/10.1093/petrology/egab041>.
- Bertrand, H., Fornari, M., Marzoli, A., García-Duarte, R. & Sempere, T. (2014). The Central Atlantic Magmatic Province extends into Bolivia. *Lithos* **188**, 33–43. <https://doi.org/10.1016/j.lithos.2013.10.019>.
- Bhattacharya, S. K., Ma, G. S.-K. & Matsuhisa, Y. (2013). Oxygen isotope evidence for crustal contamination in Deccan Basalts. *Chemie der Erde* **73**, 105–112. <https://doi.org/10.1016/j.chemer.2012.11.007>.
- Bindeman, I. N., Ponomareva, V. V., Bailey, J. C. & Valley, J. W. (2004). Volcanic arc of Kamchatka: a province with high- $\delta^{18}\text{O}$ magma sources and large-scale $^{18}\text{O}/^{16}\text{O}$ depletion of the upper crust. *Geochimica et Cosmochimica Acta* **68**, 841–865. <https://doi.org/10.1016/j.gca.2003.07.009>.
- Bindeman, I. N. (2005). Fragmentation phenomena in populations of magmatic crystals. *American Mineralogist* **90**, 1801–1815. <https://doi.org/10.2138/am.2005.1645>.
- Bindeman, I. N., Sigmarrsson, O. & Eiler, J. (2006). Time constraints on the origin of large volume basalts derived from O-isotope and trace element mineral zoning and U-series disequilibria in the Laki and Grímsvötn volcanic system. *Earth and Planetary Science Letters* **245**, 245–259. <https://doi.org/10.1016/j.epsl.2006.02.029>.
- Bindeman, I. (2008). Oxygen isotopes in mantle and crustal magmas as revealed by single crystal analysis. *Reviews in Mineralogy and Geochemistry* **69**, 445–478. <https://doi.org/10.2138/rmg.2008.69.12>.
- Bindeman, I. N., Bekker, A. & Zakharov, D. O. (2016). Oxygen isotope perspective on crustal evolution on early earth: a record of Precambrian shales with emphasis on Paleoproterozoic glaciations and Great Oxygenation Event. *Earth and Planetary Science Letters* **437**, 101–113. <https://doi.org/10.1016/j.epsl.2015.12.029>.
- Black, B. A. & Manga, M. (2017). Volatiles and the tempo of flood basalt magmatism. *Earth and Planetary Science Letters* **458**, 130–140. <https://doi.org/10.1016/j.epsl.2016.09.035>.
- Black, B. A. & Gibson, S. A. (2019). Deep carbon and the life cycle of large igneous provinces. *Elements* **15**, 319–324. <https://doi.org/10.2138/gselements.15.5.319>.
- Black, B. A., Karlstrom, L. & Mather, T. A. (2021). The life cycle of large igneous provinces. *Nature Reviews Earth & Environment* **2**, 840–857. <https://doi.org/10.1038/s43017-021-00221-4>.
- Blackburn, T. J., Olsen, P. E., Bowering, S. A., McLean, N. M., Kent, D. V., Puffer, J., McHone, G., Troy Rasbury, E. & Et-Touhami, M. (2013). Zircon U–Pb geochronology links the end-Triassic extinction with the Central Atlantic magmatic province. *Science* **340**, 941–945. <https://doi.org/10.1126/science.1234204>.
- Bond, D. P. G. & Grasby, S. E. (2017). On the causes of mass extinctions. *Palaeogeography, Palaeoclimatology, Palaeoecology* **478**, 3–29. <https://doi.org/10.1016/j.palaeo.2016.11.005>.
- Boscaini, A., Marzoli, A., Bertrand, H., Chiaradia, M., Jourdan, F., Faccenda, M., Meyzen, C. M., Callegaro, S. & Serrano Durán, L. (2022). Cratonic keels controlled the emplacement of the Central Atlantic Magmatic Province (CAMP). *Earth and Planetary Science Letters* **584**, 117480. <https://doi.org/10.1016/j.epsl.2022.117480>.
- Boulliang, J. & Wood, B. J. (2022). SO_2 solubility and degassing behavior in silicate melts. *Geochimica et Cosmochimica Acta* **336**, 150–164. <https://doi.org/10.1016/j.gca.2022.08.032>.
- Bouvier, A.-S., Rose-Koga, E. F., Nichols, A. R. L. & Le Lay, C. (2022). Melt inclusion formation during olivine recrystallization: evidence from stable isotopes. *Earth and Planetary Science Letters* **592**, 117638. <https://doi.org/10.1016/j.epsl.2022.117638>.
- Callegaro, S., Marzoli, A., Bertrand, H., Chiaradia, M., Reisberg, L., Meyzen, C., Bellieni, G., Weems, R. E. & Merle, R. (2013). Upper and lower crust recycling in the source of CAMP basaltic dykes from southeastern North America. *Earth and Planetary Science Letters* **376**, 186–199. <https://doi.org/10.1016/j.epsl.2013.06.023>.
- Callegaro, S., Baker, D. R., De Min, A., Marzoli, A., Geraki, K., Bertrand, H., Viti, C. & Nestola, F. (2014a). Microanalyses link sulphur from large igneous provinces and Mesozoic mass extinctions. *Geology* **42**(10), 895–898. <https://doi.org/10.1130/G35983.1>.
- Callegaro, S., Rapaille, C., Marzoli, A., Bertrand, H., Chiaradia, M., Reisberg, L., Bellieni, G., Martins, L., Madeira, J., Mata, J., Youbi, N., De Min, A., Rosário Azevedo, M. & Khalil Bensalah, M. (2014b). Enriched mantle source for the Central Atlantic magmatic province: new supporting evidence from southwestern Europe. *Lithos* **188**, 15–32. <https://doi.org/10.1016/j.lithos.2013.10.021>.
- Callegaro, S., Baker, D. R., Renne, P. R., Melluso, L., Geraki, K., Whitehouse, M. J., De Min, A. & Marzoli, A. (2023). Recurring volcanic winters during the latest cretaceous: sulfur and fluorine budgets of Deccan Traps lavas. *Science Advances* **9**, eadg8284. <https://doi.org/10.1126/sciadv.adg8284>.
- Capriolo, M., Marzoli, A., Aradi, L. E., Callegaro, S., Dal Corso, J., Newton, R. J., Mills, B. J. W., Wignall, P. B., Bartoli, O., Baker, D. R., Youbi, N., Remusat, L., Spiess, R. & Szabó, C. (2020). Deep CO_2 in the end-Triassic Central Atlantic Magmatic Province. *Nature Communications* **11**, 1670. <https://doi.org/10.1038/s41467-020-15325-6>.
- Capriolo, M., Marzoli, A., Aradi, L. E., Ackerson, M. R., Bartoli, O., Callegaro, S., Dal Corso, J., Ernesto, M., Gouvêa Vasconcellos, E. M., De Min, A., Newton, R. J. & Szabó, C. (2021). Massive methane fluxing from magma–sediment interaction in the end-Triassic Central Atlantic Magmatic Province. *Nature Communications* **12**, 5534. <https://doi.org/10.1038/s41467-021-25510-w>.
- Capriolo, M., Mills, B. J. W., Newton, R. J., Dal Corso, J., Dunhill, A. M., Wignall, P. B. & Marzoli, A. (2022). Anthropogenic-scale

- CO₂ degassing from the Central Atlantic Magmatic Province as a driver of the end-Triassic mass extinction. *Global and Planetary Change* **209**, 103731. <https://doi.org/10.1016/j.gloplacha.2021.103731>.
- Caracciolo, A., Halldórsson, S. A., Bali, E., Marshall, E. W., Jeon, H., Whitehouse, M. J., Barnes, J. D., Guðfinnsson, G. H., Kahl, M. & Hartley, M. E. (2022). Oxygen isotope evidence for progressively assimilating trans-crustal magma plumbing systems in Iceland. *Geology* **50**, 796–800. <https://doi.org/10.1130/G49874.1>.
- Caricchi, L., Pommier, A., Pistone, M., Castro, J., Burgisser, A. & Perugini, D. (2011). Strain-induced magma degassing: insights from simple-shear experiments on bubble bearing melts. *Bulletin of Volcanology* **73**, 1245–1257. <https://doi.org/10.1007/s00445-011-0471-2>.
- Caricchi, L., Sheldrake, T. E. & Blundy, J. (2018). Modulation of magmatic processes by CO₂ flushing. *Earth and Planetary Science Letters* **491**, 160–171. <https://doi.org/10.1016/j.epsl.2018.03.042>.
- Carvas, K. Z., Marques, L. S., Vasconcelos, P. M. & Ubide, T. (2023). Tracking the transition from a Gondwana LIP to the South Atlantic Ocean with geochronological and geochemical indicators. *Journal of Geophysical Research* **128**(5), 1–21. <https://doi.org/10.1029/2022JB025816>.
- Cashman, K. V., Sparks, R. S. J. & Blundy, J. D. (2017). Vertically extensive and unstable magmatic systems: a unified view of igneous processes. *Science* **355**, 6331. <https://doi.org/10.1126/science.aag3055>.
- Chalokwu, C. I., Ripley, E. M. & Park, Y.-R. (1999). Oxygen isotopic systematics of an open-system magma chamber: an example from the Freetown Layered Complex of Sierra Leone. *Geochimica et Cosmochimica Acta* **63**, 675–685. [https://doi.org/10.1016/S0016-7037\(99\)00098-8](https://doi.org/10.1016/S0016-7037(99)00098-8).
- Chenet, A.-L., Fluteau, F., Courtillot, V., Gérard, M. & Subbarao, K. V. (2008). Determination of rapid Deccan eruptions across the Cretaceous–Tertiary boundary using paleomagnetic secular variation: Results from a 1200-m-thick section in the Mahabaleshwar escarpment. *Journal of Geophysical Research* **113**(B04101), 1–27. <https://doi.org/10.1029/2006JB004635>.
- Cherniak, D. J. & Dimanov, A. (2010). Diffusion in pyroxene, mica and amphibole. *Reviews in Mineralogy and Geochemistry* **72**, 641–690. <https://doi.org/10.2138/rmg.2010.72.14>.
- Chin, E. J., Shimizu, K., Bybee, G. M. & Erdman, M. E. (2018). On the development of the calc-alkaline and tholeiitic magma series: a deep crustal cumulate perspective. *Earth and Planetary Science Letters* **482**, 277–287. <https://doi.org/10.1016/j.epsl.2017.11.016>.
- Choudhary, B. R., Santosh, M., De Vivo, B., Jadhav, G. & Babu, E. V. S. S. K. (2019). Melt inclusion evidence for mantle heterogeneity and magma degassing in the Deccan large Igneous Province, India. *Lithos* **346–347**, 105135. <https://doi.org/10.1016/j.lithos.2019.07.002>.
- Clapham, M. E. & Renne, P. R. (2019). Flood basalts and mass extinctions. *Annual Review of Earth and Planetary Sciences* **47**, 275–303. <https://doi.org/10.1146/annurev-earth-053018-060136>.
- Cole, D. R. & Chakraborty, S. (2001). Rates and mechanisms of isotopic exchange. *Reviews in Mineralogy and Geochemistry* **43**, 83–223. <https://doi.org/10.2138/gsrng.43.1.83>.
- Cooper, K. M. & Kent, A. J. R. (2014). Rapid remobilization of magmatic crystals kept in cold storage. *Nature* **506**, 480–483. <https://doi.org/10.1038/nature12991>.
- Coplen, T. B. (1988). Normalization of oxygen and hydrogen isotope data. *Chemical Geology* **72**, 293–297.
- Courtillot, V., Besse, J., Vandamme, D., Montigny, R., Jaeger, J.-J. & Cappetta, H. (1986). Deccan flood basalts at the Cretaceous/Tertiary boundary? *Earth and Planetary Science Letters* **80**, 361–374. [https://doi.org/10.1016/0012-821X\(86\)90118-4](https://doi.org/10.1016/0012-821X(86)90118-4).
- Cucciniello, C., Choudhary, A. K., Pande, K. & Sheth, H. (2019). Mineralogy, geochemistry and ⁴⁰Ar–³⁹Ar geochronology of the Barda and Alech complexes, Saurashtra, northwestern Deccan Traps: early silicic magmas derived by flood basalt fractionation. *Geological Magazine* **156**, 1668–1690. <https://doi.org/10.1017/S0016756818000924>.
- Cucciniello, C., Sheth, H., Duraiswami, R. A., Wegner, W., Koerber, C., Das, T. & Ghule, V. (2020). The Southeastern Saurashtra dyke swarm, Deccan Traps: magmatic evolution of a tholeiitic basalt–basaltic andesite–andesite–rhyolite suite. *Lithos* **376–377**, 105759. <https://doi.org/10.1016/j.lithos.2020.105759>.
- Dallai, L., Freda, C. & Gaeta, M. (2004). Oxygen isotope geochemistry of pyroclastic clinopyroxene monitors carbonate contributions to Roman-type ultrapotassic magmas. *Contributions to Mineralogy and Petrology* **148**, 247–263. <https://doi.org/10.1007/s00410-004-0602-2>.
- Davies, J. H. F. L., Marzoli, A., Bertrand, H., Youbi, N., Ernesto, M. & Schaltegger, U. (2017). End-Triassic mass extinction started by intrusive CAMP activity. *Nature Communications* **8**, 15596. <https://doi.org/10.1038/ncomms15596>.
- Davies, J. H. F. L., Marzoli, A., Bertrand, H., Youbi, N., Ernesto, M., Greber, N. D., Ackerson, M., Simpson, G., Bouvier, A.-S., Baumgartner, L., Pettke, T., Farina, F., Ahrenstedt, H. V. & Schaltegger, U. (2021). Zircon petrochronology in large igneous provinces reveals upper crustal contamination processes: new U–Pb ages, Hf and O isotopes, and trace elements from the Central Atlantic magmatic province (CAMP). *Contributions to Mineralogy and Petrology* **176**, 9. <https://doi.org/10.1007/s00410-020-01765-2>.
- Deckart, K., Bertrand, H. & Liégeois, J.-P. (2005). Geochemistry and Sr, Nd, Pb isotopic composition of the Central Atlantic Magmatic Province (CAMP) in Guyana and Guinea. *Lithos* **82**, 289–314. <https://doi.org/10.1016/j.lithos.2004.09.023>.
- Deegan, F. M., Whitehouse, M. J., Troll, V. R., Budd, D. A., Harris, C., Geiger, H. & Hålenius, U. (2016). Pyroxene standards for SIMS oxygen isotope analysis and their application to Merapi volcano, Sunda arc, Indonesia. *Chemical Geology* **447**, 1–10. <https://doi.org/10.1016/j.chemgeo.2016.10.018>.
- Deegan, F. M., Whitehouse, M. J., Troll, V. R., Geiger, H., Jeon, H., le Roux, P., Harris, C., van Helden, M. & González-Maurel, O. (2021). Sunda arc mantle source ⁸¹⁸O value revealed by intracrystal isotope analysis. *Nature Communications* **12**, 3930. <https://doi.org/10.1038/s41467-021-24143-3>.
- Deegan, F. M., Bédard, J. H., Grasby, S. E., Dewing, K., Geiger, H., Misiti, V., Capriolo, M., Callegaro, S., Svensen, H. H., Yakymchuk, C., Aradi, L. E., Freda, C. & Troll, V. R. (2022). Magma–shale interaction in large igneous provinces: implications for climate warming and sulphide genesis. *Journal of Petrology* **63**, 1–10. <https://doi.org/10.1093/petrology/egac094>.
- De Min, A., Piccirillo, E. M., Marzoli, A., Bellieni, G., Renne, P. R., Ernesto, M. & Marques, L. S. (2003). The Central Atlantic Magmatic Province (CAMP) in Brazil: Petrology, geochemistry, ⁴⁰Ar/³⁹Ar ages, paleomagnetism and geodynamic implications. In: Hames, W. E., McHone, J. G., Renne, P. R. & Ruppel, C. (eds.) *The Central Atlantic Magmatic Province: Insights from fragments of Pangea*. AGU Geophysical Monograph **136**. American Geophysical Union, USA (Washington, DC), pp. 91–128. <https://doi.org/10.1029/136GM06>.
- Ding, S., Plank, T., Wallace, P. J. & Rasmussen, D. J. (2023). Sulfur_X: a model of sulfur degassing during magma ascent. *Geochemistry, Geophysics, Geosystems* **24**, e2022GC010552. <https://doi.org/10.1029/2022GC010552>.

- Eiler, J. M., Schiano, P., Kitchen, N. & Stolper, E. M. (2000). Oxygen-isotope evidence for recycled crust in the sources of mid-ocean-ridge basalts. *Nature* **403**, 530–534. <https://doi.org/10.1038/35000553>.
- Emerson, D. W. (1990). Notes on mass properties of rocks: density, porosity, permeability. *Exploration Geophysics* **21**, 209–216. <https://doi.org/10.1071/EG990209>.
- Ernst, R. E. (2014) *Large Igneous Provinces*. UK (Cambridge): Cambridge University Press.
- Ernst, R. E. & Youbi, N. (2017). How large igneous provinces affect global climate, sometimes cause mass extinctions, and represent natural markers in the geological record. *Palaeogeography, Palaeoclimatology, Palaeoecology* **478**, 30–52. <https://doi.org/10.1016/j.palaeo.2017.03.014>.
- Farver, J. R. (1989). Oxygen self-diffusion in diopside with application to cooling rate determinations. *Earth and Planetary Science Letters* **92**, 386–396. [https://doi.org/10.1016/0012-821X\(89\)90062-9](https://doi.org/10.1016/0012-821X(89)90062-9).
- Farver, J. R. (2010). Oxygen and hydrogen diffusion in minerals. *Reviews in Mineralogy and Geochemistry* **72**, 447–507. <https://doi.org/10.2138/rmg.2010.72.10>.
- Faure, F. & Schiano, P. (2004). Crystal morphologies in pillow basalts: implications for mid-ocean ridge processes. *Earth and Planetary Science Letters* **220**, 331–344. [https://doi.org/10.1016/S0012-821X\(04\)00057-3](https://doi.org/10.1016/S0012-821X(04)00057-3).
- Fendley, I. M., Mittal, T., Sprain, C. J., Marvin-DiPasquale, M., Tobin, T. S. & Renne, P. R. (2019). Constraints on the volume and rate of Deccan Traps flood basalt eruptions using a combination of high-resolution terrestrial mercury records and geochemical box models. *Earth and Planetary Science Letters* **524**, 115721. <https://doi.org/10.1016/j.epsl.2019.115721>.
- Ferguson, M. R. M., Ehrig, K., Meffre, S. & Feig, S. (2019). From magma to mush to lava: crystal history of voluminous felsic lavas in the Gawler Range Volcanics, South Australia. *Lithos* **346–347**, 105148. <https://doi.org/10.1016/j.lithos.2019.105148>.
- Frezzotti, M. L., Tecce, F. & Casagli, A. (2012). Raman spectroscopy for fluid inclusion analysis. *Journal of Geochemical Exploration* **112**, 1–20.
- Genske, F. S., Beier, C., Haase, K. M., Turner, S. P., Krumm, S. & Brandl, P. A. (2013). Oxygen isotopes in the Azores islands: crustal assimilation recorded in olivine. *Geology* **41**, 491–494. <https://doi.org/10.1130/G33911.1>.
- Ghosh, P., Sayeed, M. R. G., Islam, R. & Hundekari, S. M. (2006). Inter-basaltic clay (bole bed) horizons from Deccan traps of India: implications for palaeo-weathering and palaeo-climate during Deccan volcanism. *Palaeogeography, Palaeoclimatology, Palaeoecology* **242**, 90–109. <https://doi.org/10.1016/j.palaeo.2006.05.018>.
- Gilbert, V., Batenburg, S. J., Arenillas, I. & Arz, J. A. (2021). Contribution of orbital forcing and Deccan volcanism to global climatic and biotic changes across the Cretaceous–Paleogene boundary at Zumaia, Spain. *Geology* **50**, 21–25. <https://doi.org/10.1130/G49214.1>.
- Giordano, D., Russell, J. K. & Dingwell, D. B. (2008). Viscosity of magmatic liquids: a model. *Earth and Planetary Science Letters* **271**, 123–134. <https://doi.org/10.1016/j.epsl.2008.03.038>.
- Gleeson, M. L. M., Lissenberg, C. J. & Antoshechkina, P. M. (2023). Porosity evolution of mafic crystal mush during reactive flow. *Nature Communications* **14**, 3088. <https://doi.org/10.1038/s41467-023-38136-x>.
- Gonfiantini, R. (1978). Standards for stable isotope measurements in natural compounds. *Nature* **271**, 534–536. <https://doi.org/10.1038/271534a0>.
- Grant, T. B., Larsen, R. B., Anker-Rasch, L., Grannes, K. R., Iljina, M., McEnroe, S., Nikolaisen, E., Schanche, M. & Øen, E. (2016). Anatomy of a deep crustal volcanic conduit system; the Rein-fjord Ultramafic Complex, Seiland Igneous Province, Northern Norway. *Lithos* **252–253**, 200–215. <https://doi.org/10.1016/j.lithos.2016.02.020>.
- Green, T., Renne, P. R. & Keller, C. B. (2022). Continental flood basalts drive Phanerozoic extinctions. *Proceedings of the National Academy of Sciences* **119**, 38, e2120441119. <https://doi.org/10.1073/pnas.2120441119>.
- Gualda, G. A. R., Ghiorso, M. S., Lemons, R. V. & Carley, T. L. (2012). Rhyolite-MELTS: a modified calibration of MELTS optimized for silica-rich, fluid-bearing magmatic systems. *Journal of Petrology* **53**, 875–890. <https://doi.org/10.1093/petrology/egr080>.
- Gürsoy, D., De Carlo, F., Xiao, X. & Jacobsen, C. (2014). TomoPy: a framework for the analysis of synchrotron tomographic data. *Journal of Synchrotron Radiation* **21**, 1188–1193. <https://doi.org/10.1107/S1600577514013939>.
- Halder, M., Paul, D. & Yang, S. (2023). Origin of silicic rocks of the Deccan traps continental flood basalt province: inferences from field observations, petrography, and geochemistry. *Geochemistry* **83**, 125958. <https://doi.org/10.1016/j.chemer.2023.125958>.
- Harris, C., Pronost, J. J. M., Ashwal, L. D. & Cawthorn, R. G. (2005). Oxygen and hydrogen isotope stratigraphy of the Rustenburg Layered Suite, Bushveld Complex: constraints on crustal contamination. *Journal of Petrology* **46**, 579–601. <https://doi.org/10.1093/petrology/egh089>.
- Hartley, M. E., Thordarson, T., Taylor, C., Fitton, J. G. & EIMF (2012). Evaluation of the effects of composition on instrumental mass fractionation during SIMS oxygen isotope analyses of glasses. *Chemical Geology* **334**, 312–323. <https://doi.org/10.1016/j.chemgeo.2012.10.027>.
- Hartley, M. E., Thordarson, T., Fitton, J. G. & EIMF (2013). Oxygen isotopes in melt inclusions and glasses from the Askja volcanic system, North Iceland. *Geochimica et Cosmochimica Acta* **123**, 55–73. <https://doi.org/10.1016/j.gca.2013.09.008>.
- Hartley, M. E., Maclennan, J., Edmonds, M. & Thordarson, T. (2014). Reconstructing the deep CO₂ degassing behaviour of large basaltic fissure eruptions. *Earth and Planetary Science Letters* **393**, 120–131. <https://doi.org/10.1016/j.epsl.2014.02.031>.
- Heimdal, T. H., Svensen, H. H., Ramezani, J., Iyer, K., Pereira, E., Rodrigues, R., Jones, M. T. & Callegaro, S. (2018). Large-scale sill emplacement in Brazil as a trigger for the end-Triassic crisis. *Scientific Reports* **8**, 141. <https://doi.org/10.1038/s41598-017-18629-8>.
- Heimdal, T. H., Callegaro, S., Svensen, H. H., Jones, M. T., Pereira, E. & Planke, S. (2019). Evidence for magma–evaporite interactions during the emplacement of the Central Atlantic Magmatic Province (CAMP) in Brazil. *Earth and Planetary Science Letters* **506**, 476–492. <https://doi.org/10.1016/j.epsl.2018.11.018>.
- Heimdal, T. H., Jones, M. T. & Svensen, H. H. (2020). Thermogenic carbon release from the Central Atlantic magmatic province caused major end-Triassic carbon cycle perturbations. *Proceedings of the National Academy of Sciences* **117**(22), 11968–11974. <https://doi.org/10.1073/pnas.2000095117>.
- Hernandez Nava, A., Black, B. A., Gibson, S. A., Bodnar, R. J., Renne, P. R. & Vanderkluisen, L. (2021). Reconciling early Deccan Traps CO₂ outgassing and pre-KPB global climate. *Proceedings of the National Academy of Sciences* **118**(14), e2007797118. <https://doi.org/10.1073/pnas.2007797118>.
- Hickson, R. I., Barry, S. I., Mercer, G. N. & Sidhu, H. S. (2011). Finite difference schemes for multilayer diffusion. *Mathematical and Computer Modelling* **54**, 210–220. <https://doi.org/10.1016/j.mcm.2011.02.003>.

- Holness, M. B., Anderson, A. T., Martin, V. M., MacLennan, J., Passmore, E. & Schwindinger, K. (2007). Textures in partially solidified crystalline nodules: a window into the pore structure of slowly cooled mafic intrusions. *Journal of Petrology* **48**, 1243–1264. <https://doi.org/10.1093/ptrology/egm016>.
- Holness, M. B., Nielsen, T. F. D. & Tegner, C. (2017). The Skaergaard Intrusion of East Greenland: paradigms, problems and new perspectives. *Elements* **13**, 391–396. <https://doi.org/10.2138/gselements.13.6.391>.
- Holness, M. B., Stock, M. J. & Geist, D. (2019). Magma chambers versus mush zones: constraining the architecture of sub-volcanic plumbing systems from microstructural analysis of crystalline enclaves. *Philosophical Transactions of the Royal Society A* **377**, 20180006. <https://doi.org/10.1098/rsta.2018.0006>.
- Hort, M. (1998). Abrupt change in magma liquidus temperature because of volatile loss or magma mixing: effects on nucleation, crystal growth and thermal history of the magma. *Journal of Petrology* **39**, 1063–1076. <https://doi.org/10.1093/ptrology/39.5.1063>.
- Hull, P. M., Bornemann, A., Penman, D. E., Henehan, M. J., Norris, R. D., Wilson, P. A., Blum, P., Alegret, L., Batenburg, S. J., Bown, P. R., Bralower, T. J., Courmede, C., Deutsch, A., Donner, B., Friedrich, O., Jehle, S., Kim, H., Kroon, D., Lippert, P. C., Loroch, D., Moebius, I., Moriya, K., Peppe, D. J., Ravizza, G. E., Röhl, U., Schueth, J. D., Sepúlveda, J., Sexton, P. F., Sibert, E. C., Śliwińska, K. K., Summons, R. E., Thomas, E., Westerhold, T., Whiteside, J. H., Yamaguchi, T. & Zachos, J. C. (2020). On impact and volcanism across the Cretaceous–Paleogene boundary. *Science* **367**, 266–272. <https://doi.org/10.1126/science.aay5055>.
- Jackson, M. D., Blundy, J. & Sparks, R. S. J. (2018). Chemical differentiation, cold storage and remobilization of magma in the Earth's crust. *Nature* **564**, 405–409. <https://doi.org/10.1038/s41586-018-0746-2>.
- Jochum, K. P., Stoll, B., Herwig, K., Willbold, M., Hofmann, A. W., Amiri, M., Aarburg, S., Abouchami, W., Hellebrand, E., Mocek, B., Raczek, I., Stracke, A., Alard, O., Bouman, C., Becker, S., Dücking, M., Brätz, H., Klemd, R., de Bruin, D., Canil, D., Cornell, D., de Hoog, C.-J., Dalpé, C., Danyushevsky, L., Eisenhauer, A., Gao, Y., Snow, J. E., Groschopf, N., Günther, D., Latkoczy, C., Guillong, M., Hauri, E. H., Höfer, H. E., Lahaye, Y., Horz, K., Jacob, D. E., Kasemann, S. A., Kent, A. J. R., Ludwig, T., Zack, T., Mason, P. R. D., Meixner, A., Rosner, M., Misawa, K., Nash, B. P., Pfänder, J., Premo, W. R., Sun, W. D., Tiepolo, M., Vannucci, R., Vennemann, T., Wayne, D. & Woodhead, J. D. (2006). MPI-DING reference glasses for in situ microanalysis: new reference values for element concentrations and isotope ratios. *Geochemistry, Geophysics, Geosystems* **7**, Q02008. <https://doi.org/10.1029/2005GC001060>.
- Karlstrom, L. & Richards, M. (2011). On the evolution of large ultramafic magma chambers and timescales for flood basalt eruptions. *Journal of Geophysical Research* **116**(B08216), 1–13. <https://doi.org/10.1029/2010JB008159>.
- Kawakami, Y., Yamamoto, J. & Kagi, H. (2003). Micro-Raman densimeter for CO₂ inclusions in mantle-derived minerals. *Applied Spectroscopy* **57**, 1333–1339. <https://doi.org/10.1366/000370203322554473>.
- Kent, A. J. R. (2008). Melt inclusions in basaltic and related volcanic rocks. *Reviews in Mineralogy and Geochemistry* **69**, 273–331. <https://doi.org/10.2138/rmg.2008.69.8>.
- Knight, K. B., Nomade, S., Renne, P. R., Marzoli, A., Bertrand, H. & Youbi, N. (2004). The Central Atlantic Magmatic Province at the Triassic–Jurassic boundary: paleomagnetic and ⁴⁰Ar/³⁹Ar evidence from Morocco for brief, episodic volcanism. *Earth and Planetary Science Letters* **228**, 143–160. <https://doi.org/10.1016/j.epsl.2004.09.022>.
- Kontak, D. J. (2008). On the edge of CAMP: geology and volcanology of the Jurassic North Mountain Basalt, Nova Scotia. *Lithos* **101**, 74–101. <https://doi.org/10.1016/j.lithos.2007.07.013>.
- Kontak, D. J. & Dostal, J. (2010). The late-stage crystallization history of the Jurassic North Mountain Basalt, Nova Scotia, Canada: II. Nature and origin of segregation pipes. *The Canadian Mineralogist* **48**, 1533–1568. <https://doi.org/10.3749/canmin.48.5.1533>.
- Krans, S. R., Rooney, T. O., Kappelman, J., Yirgu, G. & Ayalew, D. (2018). From initiation to termination: a petrostratigraphic tour of the Ethiopian low-Ti flood basalt province. *Contributions to Mineralogy and Petrology* **173**, 37. <https://doi.org/10.1007/s00410-018-1460-7>.
- Kress, V. C. & Ghiorso, M. S. (2004). Thermodynamic modeling of post-entrapment crystallization in igneous phases. *Journal of Volcanology and Geothermal Research* **137**, 247–260. <https://doi.org/10.1016/j.jvolgeores.2004.05.012>.
- Krishnamurthy, P. (2020a). The Deccan Volcanic Province (DVP), India: a review. Part 1: areal extent and distribution, compositional diversity, flow types and sequences, stratigraphic correlations, dyke swarms and sills, petrography and mineralogy. *Journal Geological Society of India* **96**, 9–35. <https://doi.org/10.1007/s12594-020-1501-5>.
- Krishnamurthy, P. (2020b). The Deccan Volcanic Province (DVP), India: a review. Part 2: geochemistry, petrological evolution, petrogenesis, mantle sources, age and erupted volume relations, upper cretaceous–Palaeogene (K–Pg) mass extinctions, economic aspects, summary and future studies in DVP. *Journal Geological Society of India* **96**, 111–147. <https://doi.org/10.1007/s12594-020-1521-1>.
- Lamadrid, H. M., Moore, L. R., Moncada, D., Rimstidt, J. D., Burruss, R. C. & Bodnar, R. J. (2017). Reassessment of the Raman CO₂ densimeter. *Chemical Geology* **450**, 210–222. <https://doi.org/10.1016/j.chemgeo.2016.12.034>.
- Le Maitre, R. W. (2002). *Igneous Rocks: A Classification and Glossary of Terms*. In: Le Maitre, R. W., Streckeisen, A., Zanettin, B., Le Bas, M. J., Bonin, B. & Bateman, P. (eds.) *Recommendations of the International Union of Geological Sciences Subcommission on the Systematics of Igneous Rocks*. UK (Cambridge): Cambridge University Press.
- Mahoney, J., Macdougall, J. D., Lugmair, G. W., Murali, A. V., Sankar Das, M. & Gopalan, K. (1982). Origin of the Deccan Trap flows at Mahabaleshwar inferred from Nd and Sr isotopic and chemical evidence. *Earth and Planetary Science Letters* **60**, 47–60. [https://doi.org/10.1016/0012-821X\(82\)90019-X](https://doi.org/10.1016/0012-821X(82)90019-X).
- Marsh, B. D. (2015). Magma chambers. In: Sigurdsson H. (ed.) *The Encyclopedia of Volcanoes*. USA (Cambridge, Massachusetts): Academic Press, pp.185–201.
- Marzoli, A., Renne, P. R., Piccirillo, E. M., Ernesto, M., Bellieni, G. & De Min, A. (1999). Extensive 200-million-year-old continental flood basalts of the Central Atlantic Magmatic Province. *Science* **284**, 616–618. <https://doi.org/10.1126/science.284.5414.616>.
- Marzoli, A., Bertrand, H., Knight, K. B., Cirilli, S., Buratti, N., Vérati, C., Nomade, S., Renne, P. R., Youbi, N., Martini, R., Allenbach, K., Neuwerth, R., Rapaille, C., Zaninetti, L. & Bellieni, G. (2004). Synchrony of the Central Atlantic magmatic province and the Triassic–Jurassic boundary climatic and biotic crisis. *Geology* **32**, 973–976. <https://doi.org/10.1130/G20652.1>.
- Marzoli, A., Callegaro, S., Dal Corso, J., Davies, J. H. F. L., Chiaradia, M., Youbi, N., Bertrand, H., Reisberg, L., Merle, R. & Jourdan, F. (2018). The Central Atlantic Magmatic Province (CAMP): a review. In: Tanner, L. H. (ed.) *The Late Triassic World: Earth in a Time of Transition*. Topics in Geobiology **46**. Germany (Heidelberg): Springer, pp. 91–125. https://doi.org/10.1007/978-3-319-68009-5_4.
- Marzoli, A., Bertrand, H., Youbi, N., Callegaro, S., Merle, R., Reisberg, L., Chiaradia, M., Brownlee, S. I., Jourdan, F., Zanetti, A.,

- Davies, J. H. F. L., Cuppone, T., Mahmoudi, A., Medina, F., Renne, P. R., Bellieni, G., Crivellari, S., El Hachimi, H., Khalil Bensalah, M., Meyzen, C. M. & Tegner, C. (2019). The Central Atlantic Magmatic Province (CAMP) in Morocco. *Journal of Petrology* **60**, 945–996. <https://doi.org/10.1093/petrology/egz021>.
- Marzoli, A., Renne, P. R., Andreasen, R., Spiess, R., Chiaradia, M., Ruth, D. C. S., Tholt, A. J., Pande, K. & Costa, F. (2022). The shallow magmatic plumbing system of the Deccan Traps, evidence from plagioclase megacrysts and their host lavas. *Journal of Petrology* **63**, 1–32. <https://doi.org/10.1093/petrology/egac075>.
- Matsuhisa, Y., Bhattacharya, S. K., Gopalan, K., Mahoney, J. & Macdougall, J. D. (1986). Oxygen isotope evidence for crustal contamination in Deccan basalts. *Terra Cognita* **6**, 181.
- Mattey, D., Lowry, D. & Macpherson, C. (1994). Oxygen isotope composition of mantle peridotite. *Earth and Planetary Science Letters* **128**, 231–241. [https://doi.org/10.1016/0012-821X\(94\)90147-3](https://doi.org/10.1016/0012-821X(94)90147-3).
- McCarthy, A., Chelle-Michou, C., Blundy, J. D., Vonlanthen, P., Meibom, A. & Escrig, S. (2020). Taking the pulse of volcanic eruptions using plagioclase glomerocrysts. *Earth and Planetary Science Letters* **552**, 116596. <https://doi.org/10.1016/j.epsl.2020.116596>.
- Melluso, L., Mahoney, J. J. & Dallai, L. (2006). Mantle sources and crustal input as recorded in high-Mg Deccan Traps basalts of Gujarat (India). *Lithos* **89**, 259–274. <https://doi.org/10.1016/j.lithos.2005.12.007>.
- Melluso, L. & Sethna, S. F. (2010) Mineral compositions in the Deccan igneous rocks of India: An overview. In: Ray J., Sen G. & Ghosh B. (eds.) *Topics in Igneous Petrology*. Germany (Heidelberg): Springer, pp.135–159.
- Merle, R., Marzoli, A., Bertrand, H., Reisberg, L., Verati, C., Zimmermann, C., Chiaradia, M., Bellieni, G. & Ernesto, M. (2011). $^{40}\text{Ar}/^{39}\text{Ar}$ ages and Sr–Nd–Pb–Os geochemistry of CAMP tholeiites from Western Maranhão basin (NE Brazil). *Lithos* **122**, 137–151. <https://doi.org/10.1016/j.lithos.2010.12.010>.
- Merle, R., Marzoli, A., Reisberg, L., Bertrand, H., Nemchin, A., Chiaradia, M., Callegaro, S., Jourdan, F., Bellieni, G., Kontak, D., Puffer, J. & Mchone, J. G. (2014). Sr, Nd, Pb and Os isotope systematics of CAMP tholeiites from Eastern North America (ENA): evidence of a subduction-enriched mantle source. *Journal of Petrology* **55**, 133–180. <https://doi.org/10.1093/petrology/egt063>.
- Merzbacher, C. & Eggler, D. H. (1984). A magmatic geohygrometer: application to Mount St. Helens and other dacitic magmas. *Geology* **12**, 587–590. [https://doi.org/10.1130/0091-7613\(1984\)12<587:AMGATM>2.0.CO;2](https://doi.org/10.1130/0091-7613(1984)12<587:AMGATM>2.0.CO;2).
- Mittal, T. & Richards, M. A. (2021). The magmatic architecture of continental flood basalts: 2. A new conceptual model. *Journal of Geophysical Research* **126** B021807, 1–54.
- Mittal, T., Richards, M. A. & Fendley, I. M. (2021). The magmatic architecture of continental flood basalts I: observations from the Deccan Traps. *Journal of Geophysical Research* **126**(12), 1–54. <https://doi.org/10.1029/2021JB021808>.
- Mittal, T., Sprain, C. J., Renne, P. R. & Richards, M. A. (2022). Deccan volcanism at K-Pg time. *Special Paper of the Geological Society of America* **557**, 1–26. [https://doi.org/10.1130/2022.2557\(22\)](https://doi.org/10.1130/2022.2557(22)).
- Moore, L. R., Gazel, E., Tuohy, R., Lloyd, A. S., Esposito, R., Steele-Macinnis, M., Hauri, E. H., Wallace, P. J., Plank, T. & Bodnar, R. J. (2015). Bubbles matter: an assessment of the contribution of vapor bubbles to melt inclusion volatile budgets. *American Mineralogist* **100**, 806–823. <https://doi.org/10.2138/am-2015-5036>.
- Morimoto, N. (1988). Nomenclature of pyroxenes. *American Mineralogist* **73**, 1123–1133.
- Mourtada-Bonnefoi, C. C. & Laporte, D. (2002). Homogeneous bubble nucleation in rhyolitic magmas: an experimental study of the effect of H₂O and CO₂. *Journal of Geophysical Research* **107**(B42066), 1–19. <https://doi.org/10.1029/2001JB000290>.
- Neave, D. A. & Putirka, K. D. (2017). A new clinopyroxene-liquid barometer, and implications for magma storage pressures under Icelandic rift zones. *American Mineralogist* **102**, 777–794. <https://doi.org/10.2138/am-2017-5968>.
- O'Connor, L., Szymanowski, D., Eddy, M. P., Samperton, K. M. & Schoene, B. (2022). A red bole zircon record of cryptic silicic volcanism in the Deccan Traps, India. *Geology* **50**, 460–464. <https://doi.org/10.1130/G49613.1>.
- Peng, Z. X., Mahoney, J., Hooper, P., Harris, C. & Beane, J. (1994). A role for lower continental crust in flood basalt genesis? Isotopic and incompatible element study of the lower six formations of the western Deccan Traps. *Geochimica et Cosmochimica Acta* **58**, 267–288. [https://doi.org/10.1016/0016-7037\(94\)90464-2](https://doi.org/10.1016/0016-7037(94)90464-2).
- Peng, Z. X. & Mahoney, J. J. (1995). Drillhole lavas from the northwestern Deccan Traps, and the evolution of Réunion hotspot mantle. *Earth and Planetary Science Letters* **134**, 169–185. [https://doi.org/10.1016/0012-821X\(95\)00110-X](https://doi.org/10.1016/0012-821X(95)00110-X).
- Peng, Z. X., Mahoney, J. J., Hooper, P. R., Macdougall, J. D. & Krishnamurthy, P. (1998). Basalts of the northeastern Deccan Traps, India: isotopic and elemental geochemistry and relation to southwestern Deccan stratigraphy. *Journal of Geophysical Research* **103**(B12), 29843–29865. <https://doi.org/10.1029/98JB01514>.
- Peters, B. J., Day, J. M. D., Greenwood, R. C., Hilton, D. R., Gibson, J. & Franchi, I. A. (2017). Helium–oxygen–osmium isotopic and elemental constraints on the mantle sources of the Deccan Traps. *Earth and Planetary Science Letters* **478**, 245–257. <https://doi.org/10.1016/j.epsl.2017.08.042>.
- Philpotts, A. R., Carroll, M. & Hill, J. M. (1996). Crystal-mush compaction and the origin of pegmatitic segregation sheets in a thick flood-basalt flow in the Mesozoic Hartford Basin, Connecticut. *Journal of Petrology* **37**, 811–836. <https://doi.org/10.1093/petrology/37.4.811>.
- Pichavant, M., Di Carlo, I., Rotolo, S. G., Scaillet, B., Burgisser, A., Le Gall, N. & Martel, C. (2013). Generation of CO₂-rich melts during basalt magma ascent and degassing. *Contributions to Mineralogy and Petrology* **166**, 545–561. <https://doi.org/10.1029/98JB01514>.
- Pistone, M., Caricchi, L., Ulmer, P., Reusser, E. & Ardia, P. (2013). Rheology of volatile-bearing crystal mushes: mobilization vs. viscous death. *Chemical Geology* **345**, 16–39. <https://doi.org/10.1016/j.chemgeo.2013.02.007>.
- Putirka, K., Johnson, M., Kinzler, R., Longhi, J. & Walker, D. (1996). Thermobarometry of mafic igneous rocks based on clinopyroxene-liquid equilibria, 0–30 kbar. *Contributions to Mineralogy and Petrology* **123**, 92–108. <https://doi.org/10.1007/s004100050145>.
- Putirka, K. D., Mikaelian, H., Ryerson, F. & Shaw, H. (2003). New clinopyroxene-liquid thermobarometers for mafic, evolved, and volatile-bearing lava compositions, with applications to lavas from Tibet and the Snake River Plain, Idaho. *American Mineralogist* **88**, 1542–1554. <https://doi.org/10.2138/am-2003-1017>.
- Putirka, K. D. (2008). Thermometers and barometers for volcanic systems. *Reviews in Mineralogy and Geochemistry* **69**, 61–120. <https://doi.org/10.2138/rmg.2008.69.3>.
- Raup, D. M. & Sepkoski, Jr., J. J. (1982). Mass extinctions in the marine fossil record. *Science* **215**, 1501–1503. <https://doi.org/10.1126/science.215.4539.1501>.
- Renne, P. R., Sprain, C. J., Richards, M. A., Self, S., Vanderkluyzen, L. & Pande, K. (2015). State shift in Deccan volcanism at the Cretaceous–Paleogene boundary, possibly induced by impact. *Science* **350**, 76–78. <https://doi.org/10.1126/science.aac7549>.

- Roedder, E. (1979). Origin and significance of magmatic inclusions. *Bulletin de Minéralogie* **102**, 487–510. <https://doi.org/10.3406/bulmi.1979.7299>.
- Roedder, E. (1984). *Fluid inclusions*. Reviews in Mineralogy **12**. Germany (Berlin): De Gruyter. <https://doi.org/10.1515/9781501508271>.
- Rosso, K. M. & Bodnar, R. J. (1995). Microthermometric and Raman spectroscopic detection limits of CO₂ in fluid inclusions and the Raman spectroscopic characterization of CO₂. *Geochimica et Cosmochimica Acta* **59**, 3961–3975. [https://doi.org/10.1016/0016-7037\(95\)94441-H](https://doi.org/10.1016/0016-7037(95)94441-H).
- Rudnick, R. L. & Gao, S. (2014). Composition of the continental crust. In: Holland, H. D. & Turekian, K. K. (eds.) *Treatise on Geochemistry* **3** (2003). UK (Oxford): Elsevier, pp. 1–64.
- Ryerson, F. J. & McKeegan, K. D. (1994). Determination of oxygen self-diffusion in åkermanite, anorthite, diopside, and spinel: implications for oxygen isotopic anomalies and the thermal histories of Ca–Al-rich inclusions. *Geochimica et Cosmochimica Acta* **58**, 3713–3734. [https://doi.org/10.1016/0016-7037\(94\)90161-9](https://doi.org/10.1016/0016-7037(94)90161-9).
- Schoene, B., Eddy, M. P., Samperton, K. M., Keller, C. B., Keller, G., Adatte, T. & Khadri, S. F. R. (2019). U–Pb constraints on pulsed eruption of the Deccan Traps across the end-Cretaceous mass extinction. *Science* **363**, 862–866. <https://doi.org/10.1126/science.aau2422>.
- Self, S., Thordarson, T. & Widdowson, M. (2005). Gas fluxes from flood basalt eruptions. *Elements* **1**, 283–287. <https://doi.org/10.2113/gselements.1.5.283>.
- Self, S., Blake, S., Sharma, K., Widdowson, M. & Sephton, S. (2008). Sulfur and chlorine in late Cretaceous Deccan magmas and eruptive gas release. *Science* **319**, 1654–1657. <https://doi.org/10.1126/science.1152830>.
- Self, S., Mittal, T., Dole, G. & Vanderkluysen, L. (2022). Toward understanding Deccan volcanism. *Annual Review of Earth and Planetary Sciences* **50**, 477–506. <https://doi.org/10.1146/annurev-earth-012721-051416>.
- Shea, T. (2017). Bubble nucleation in magmas: a dominantly heterogeneous process? *Journal of Volcanology and Geothermal Research* **343**, 155–170. <https://doi.org/10.1016/j.jvolgeores.2017.06.025>.
- Sheth, H. C. & Melluso, L. (2008). The Mount Pavagadh volcanic suite, Deccan Traps: geochemical stratigraphy and magmatic evolution. *Journal of Asian Earth Sciences* **32**, 5–21. <https://doi.org/10.1016/j.jseaes.2007.10.001>.
- Shishkina, T. A., Botcharnikov, R. E., Holtz, F., Almeev, R. R. & Portnyagin, M. V. (2010). Solubility of H₂O- and CO₂-bearing fluids in tholeiitic basalts at pressures up to 500 MPa. *Chemical Geology* **277**, 115–125. <https://doi.org/10.1016/j.chemgeo.2010.07.014>.
- Sparks, R. S. J., Annen, C., Blundy, J. D., Cashman, K. V., Rust, A. C. & Jackson, M. D. (2019). Formation and dynamics of magma reservoirs. *Philosophical Transactions of the Royal Society A* **377**, 20180019. <https://doi.org/10.1098/rsta.2018.0019>.
- Sprain, C. J., Renne, P. R., Vanderkluysen, L., Pande, K., Self, S. & Mittal, T. (2019). The eruptive tempo of Deccan volcanism in relation to the Cretaceous–Paleogene boundary. *Science* **363**, 866–870. <https://doi.org/10.1126/science.aav1446>.
- Steele-MacInnis, M., Esposito, R. & Bodnar, R. J. (2011). Thermodynamic model for the effect of post-entrapment crystallization on the H₂O–CO₂ systematics of vapor-saturated, silicate melt inclusions. *Journal of Petrology* **52**, 2461–2482. <https://doi.org/10.1093/petrology/egr052>.
- Steele-MacInnis, M., Esposito, R., Moore, L. R. & Hartley, M. E. (2017). Heterogeneously entrapped, vapor-rich melt inclusions record pre-eruptive magmatic volatile contents. *Contributions to Mineralogy and Petrology* **172**, 18. <https://doi.org/10.1007/s00410-017-1343-3>.
- Svensen, H., Planke, S., Malthes-Sørensen, A., Jamtveit, B., Myklebust, R., Rasmussen Eidem, T. & Rey, S. S. (2004). Release of methane from a volcanic basin as a mechanism for initial Eocene global warming. *Nature* **429**, 542–545. <https://doi.org/10.1038/nature02566>.
- Tamic, N., Behrens, H. & Holtz, F. (2001). The solubility of H₂O and CO₂ in rhyolitic melts in equilibrium with a mixed CO₂–H₂O fluid phase. *Chemical Geology* **174**, 333–347. [https://doi.org/10.1016/S0009-2541\(00\)00324-7](https://doi.org/10.1016/S0009-2541(00)00324-7).
- Taylor, Jr., H. P., Turi, B. & Cundari, A. (1984). ¹⁸O/¹⁶O and chemical relationships in K-rich volcanic rocks from Australia, East Africa, Antarctica, and San Venanzo–Cupaello, Italy. *Earth and Planetary Science Letters* **69**, 263–276. [https://doi.org/10.1016/0012-821X\(84\)90186-9](https://doi.org/10.1016/0012-821X(84)90186-9).
- Taylor, Jr., H. P. & Sheppard, S. M. F. (1986). Igneous rocks: I. Processes of isotopic fractionation and isotope systematics. In: Valley, J. W., Taylor, Jr., H. P. & O’Neil, J. R. (eds.) *Stable isotopes in high temperature geological processes*. Reviews in Mineralogy **16**. Germany (Berlin): De Gruyter, pp. 227–272. <https://doi.org/10.1515/9781501508936-013>.
- Tian, X. & Buck, W. R. (2022). Intrusions induce global warming before continental flood basalt volcanism. *Nature Geoscience* **15**, 417–422. <https://www.nature.com/articles/s41561-022-00939-w>.
- Troch, J., Ellis, B. S., Harris, C., Bachmann, O. & Bindeman, I. N. (2020). Low-^δ¹⁸O silicic magmas on Earth: a review. *Earth-Science Reviews* **208**, 103299. <https://doi.org/10.1016/j.earscirev.2020.103299>.
- Ubide, T., Galé, C., Arranz, E., Lago, M. & Larrea, P. (2014). Clinopyroxene and amphibole crystal populations in a lamprophyre sill from the Catalonia Coastal Ranges (NE Spain): a record of magma history and a window to mineral-melt partitioning. *Lithos* **184–187**, 225–242. <https://doi.org/10.1016/j.lithos.2013.10.029>.
- Ubide, T., Mollo, S., Zhao, J.-X., Nazzari, M. & Scarlato, P. (2019). Sector-zoned clinopyroxene as a recorder of magma history, eruption triggers, and ascent rates. *Geochimica et Cosmochimica Acta* **251**, 265–283. <https://doi.org/10.1016/j.gca.2019.02.021>.
- Ubide, T., Larrea, P., Becerril, L. & Galé, C. (2022). Volcanic plumbing filters on ocean-island basalt geochemistry. *Geology* **50**, 26–31. <https://doi.org/10.1130/G49224.1>.
- Wadeson, N. & Basham, M. (2016). Savu: a python-based, MPI framework for simultaneous processing of multiple, N-dimensional, large tomography datasets. <https://doi.org/10.48550/arXiv.1610.08015>.
- Wallace, P. J. & Edmonds, M. (2011). The sulfur budget in magmas: evidence from melt inclusions, submarine glasses, and volcanic gas emissions. *Reviews in Mineralogy and Geochemistry* **73**, 215–246. <https://doi.org/10.2138/rmg.2011.73.8>.
- Whalen, L., Gazel, E., Vidito, C., Puffer, J., Bizimis, M., Henika, W. & Caddick, M. J. (2015). Supercontinental inheritance and its influence on supercontinental breakup: the Central Atlantic Magmatic Province and the breakup of Pangea. *Geochemistry, Geophysics, Geosystems* **16**, 3532–3554. <https://doi.org/10.1002/2015GC005885>.
- Wignall, P. B. (2015) *The Worst of Times: How Life on Earth Survived Eighty Million Years of Extinctions*. USA (Princeton, New Jersey): Princeton University Press.
- Xu, J.-Y., Giuliani, A., Li, Q.-L., Lu, K., Melgarejo, J. C. & Griffin, W. L. (2021). Light oxygen isotopes in mantle-derived magmas reflect assimilation of sub-continental lithospheric mantle material. *Nature Communications* **12**, 6295. <https://doi.org/10.1038/s41467-021-26668-z>.
- Zhang, Y. & Ni, H. (2010). Diffusion of H, C, and O components in silicate melts. *Reviews in Mineralogy and Geochemistry* **72**, 171–225. <https://doi.org/10.2138/rmg.2010.72.5>.